Measurement of the Valence Quark Spin Distributions of the Nucleon Using Deep Inelastic Scattering at HERMES

Diplomarbeit

vorgelegt von

Felix M. Menden

TRIUMF, Vancouver B.C., Canada
II. Institut für Experimentalphysik Universität Hamburg

Hamburg
Oktober 1997

Measurement of the Valence Quark Spin Distributions of the Nucleon Using Deep Inelastic Scattering at HERMES

Author:	Felix M. Menden
Date:	October 28, 1997
Supervisors:	Dr.M.C.Vetterli (TRIUMF, Simon Fraser University)
	Prof.Dr.A.Wagner (DESY, Universität Hamburg)

Contents

0 Zusammenfassung in deutscher Sprache

In tief-inelastischer Lepton-Nukleon-Streuung ist der Impulsübertrag (Q^2) so groß, und die daher auflösbare Distanz so klein, daß die Substruktur des Nukleons untersucht werden kann. Innerhalb der letzten fünfzig Jahre führten zahlreiche Hochenergiephysik-Experimente zu einer Vorstellung, in der das Lepton, durch Austausch eines virtuellen Photons, inkohärent an einem Parton (Quark) des Nukleons streut. Im Streuprozeß bricht das Nukleon auseinander und das getroffene Quark sowie der Rest des Targets fragmentieren zu Hadronen. Aus der Kinematik des gestreuten Leptons läßt sich der Bruchteil des Viererimpulses den das getroffene Quark im Nukleon getragen hat, vollständig berechnen. In Koinzidenz detektierte Hadronen, die von der Fragmentation des getroffenen Quarks (*current region*) stammen, erlauben eine Messung der einzelnen Quark-Komponenten des Nukleons.

Die Aufklärung der (unpolarisierten) Struktur des Protons ergab, daß die eigentlichen Quarks nur etwa die Hälfte des Nukleonimpulses tragen. Der Rest wird von den Gluonen im Nukleon getragen. Die Spinstruktur - des als selbstverständlich als Fermion verstandenen - Protons ist aber noch ungeklärt. Experimente in den siebziger Jahren führten zu Ergebnissen, die einen mit Null verträglichen Spinanteil der Quarks ergaben (*nucleon spin crisis*). Dies war der Auslöser für den Aufbau einer zweiten Generation von Spin-Experimenten am SLAC, CERN und bei HERA. HERMES ist ein HERA-Experiment, indem polarisierte Leptonen (Positronen) an einen polarisierten Target gestreut werden. Einfache Rechnungen im Quark-Parton Modell (Kap.2) zeigen, daß aus semi-inklusiven (gestreutes Positron wird in Koinzidenz mit einem Hadron detektiert) Pion-Spin-Asymmetrien, gemessen mit verschiedenen Targets (^{1}H,^{2}H,^{3}He), die Valenzquark-Beiträge des Nukleonspins bestimmt werden können. Dabei werden die Ausdrücke für die Teilchenausbeuten mit Hilfe von Fragmentationsfunktionen, die die (unbekannte) Struktur des Fragmentationsprozesses enthalten, geschrieben.

Der HERMES Detektor ist optimiert, tief-inelastische Streuereignisse aufzuzeichnen. Der durch den Sokolov-Ternov Effekt polarisierte Positronenstrahl des HERA Speicherrings wird an den Nukleonen eines Ring-internen polarisierten Gastargets gestreut. Der Spinzustand der Atomkerne des Gases wird dabei in kleinen Zeitintervallen umgekehrt (1-10 min). Die Polarisation des Positronenstrahls wird mit einem longitudinalen und einem transversalen Polarimeter gemessen. Spurrekonstruktion und Impulsmessung werden durch den HERMES Magneten in Verbindung mit einer Reihe von Driftkammern in der Detektoranordnung (Abb.3.5) ermöglicht. Ein Čerenkov Schwellenzähler, ein Übergangsstrahlungs-Detektor (TRD), ein Preshower Detektor und ein Kalorimeter erlauben eine effiziente Teilchenidentifikation, die semi-inklusive Messungen ermöglicht. Der HERA Positronenstrahl, die benutzten Targets und das HERMES Vorwärtsspektrometer sind in Kap.3 ausführlich beschrieben.

Diese Arbeit hat zwei Schwerpunkte: Eine Wahrscheinlichkeitsanalyse der Detektorantwort des HERMES TRD (Übergangsstrahlungs-Detektor), die zu einer verbesserten Teilchenidentifikation führt, und eine Extraktion der Spin-Verteilungen der Valenzquarks unter der Benutzung der ersten HERMES 1995/1996 Daten.

Der HERMES TRD ist ein gutes Beispiel für die Ausnutzung des Übergansstrahlungseffekts im Detektorbau. Die Möglichkeit ein Signal zu erhalten, das vom Lorentz-Faktor des Teilchens und nicht von seiner Geschwindigkeit abhängig ist, ermöglicht eine hervorragende Hadron/Positron Diskriminierung relativistischer Teilchen. Die Wahrscheinlichkeitsanalyse der Detektorantwort des sechsmoduligen TRD basiert auf Bayes Theorem. Dazu werden Mutterverteilungen (*parent distributions*) für jedes Modul und jede Teilchenart definiert. Die Wahrscheinlichkeit, daß ein Teilchen eine Detektorantwort verursacht hat, ergibt sich aus der Evaluation der Detektorantwort mit den entsprechenden *parent distributions*. Da diese Wahrscheinlichkeiten implizit gekoppelt sind, werden sie als *conditional probabilities* bezeichnet. Der sogenannte Flußfaktor, das Verhältnis der Teilchensorten in einem definierten kinematischen Bereich, läßt sich iterativ berechnen und zur Teilchenidentifikation heranziehen. Flußfaktoren erlauben die *conditional probabilities* in 'echte' Wahrscheinlichkeiten umzurechnen. Diese *real probabilities* repräsentieren die Wahrscheinlichkeit, daß ein Detektorsignal von einem bestimmten Teilchen verursacht wurde. Beide Größen, die *conditional probability* und die *real probability* bieten eine bessere Teilchenidentifikation als der bisher angewandte spezielle Mittelwert (*truncated mean*) aus den sechs Modulantworten (Kap.4).

Die Analyse der polarisierten Daten ist in Kap.5 beschrieben. Die dort definierte Datenqualität selektiert die Untermenge der gemessenen Daten mit einwandfrei arbeitendem Beschleunigerring, Target und Spektrometer. Nach der Korrektur für ladungssymmetrischen Untergrund, können die semi-inklusiven Spin-Asymmetrien aus den 1995 (^{3}He) und 1996 (^{1}H) Daten berechnet werden. Entsprechend des naiven Quark-Parton Modells werden aus den Ladung-Differenz-Pion-Asymmetrien die polarisierten Valenzquarkverteilungen $\delta u_v(x)$ und $\delta d_v(x)$ extrahiert. Das Ergebnis ist statistisch limitiert, vor allem durch die Helium-Daten aus dem (Inbetriebnahme-) Jahr 1995. Verschiedene systematische Studien, sowie Zeitserien und Monte Carlo Simulationen geben Aufschluß über systematische Effekte. Die angenommene Isospin- und Ladungskonjugations-Symmetrien der Fragmentationsfunktionen sind hierbei noch zu beweisen.

Das HERMES Experiment wird eine präzise Bestimmung der Quark-Spinverteilungen des Nukleons durchführen. Die vorliegende Datenanalyse stellt eine Möglichkeit der Extraktion der polarisierten Valenzquarkverteilungen unter der Benutzung erster HERMES Daten vor. Nicht nur die in Zukunft erwartet Statistik, sondern auch alternative Extraktionsmethoden werden eine präzisere Bestimmung der Spin-Strukturfunktionen erlauben, als in dieser Arbeit vorgestellt. Die bevorstehende Aufklärung der Spinstruktur des Nukleons in dieser und der nächsten Dekade (COMPASS) machen polarisierte tief-inelastischen Streuung zu einem aufregenden aktuellen Gebiet der Hochenergiephysik.

1 Introduction

The understanding of the sub-structure of the proton (neutron) is one of most fundamental questions of high-energy physics. Scattering experiments probe the sub-structure of the nucleon by scattering (point-like) leptons incoherently off the constituents (partons). During this process, the proton breaks up and the fragments appear as outgoing hadrons (*deep-inelastic scattering*).

A series of deep inelastic lepton-nucleon scattering experiments measured the unpolarized structure of the nucleon during the last fifty years establishing the Quark Parton Model (QPM). The surprise was that only half of the proton momentum is carried by the quarks. The field quanta of the strong interaction, the gluons, are responsible for the remaining half. After the division of the nucleon momentum between the constituents was clarified, the following question arose: Where does the spin of the nucleon come from?

Results from first experiments (1970 and later) using polarized leptons and nucleon targets indicated a quark spin-contribution consistent with zero (*nucleon spin-crisis*). The spin structure of the nucleon was (is) not entirely understood. So a next generation of spin experiments was proposed and built at SLAC, CERN, and HERA to solve this problem. The next decade will be an exiting time for understanding sub-nucleon degrees of freedom.

The HERMES experiment (HERa spin MESurement) is optimized for the detection of deep inelastic scattering events. The polarized positrons of the HERA storage ring are scattered off nucleons in a ring-internal (dilution free) polarized gas target into the HERMES spectrometer. The large acceptance of the forward spectrometer covers a broad kinematic range for the scattered positron. The HERMES particle identification is able to identify the deep inelastic positron and hadrons coming in coincidence. This is the basis for the measurement of *inclusive* (scattered positron only) and *semi-inclusive* (hadron in coincidence required) spin asymmetries. By identifying pions and using different targets, the single quark spin distributions can be measured.

This thesis focuses on two aspects of the HERMES data analysis: an improved particle identification of the HERMES Transition Radiation Detector (TRD) using a probability-based method, and the measurement of the semi-inclusive charged pion spin asymmetries on a ^{3}He (1995) and a proton (1996) target with subsequent extraction of $\delta u_v(x)$ and $\delta d_v(x)$ within the simple QPM. The 1996 dataset is presented giving a first impression of the statistical accuracy of the HERMES data (fig.5.9).

HERMES will provide precise measurements of the quark contributions to the spin of the nucleon. Upgrades focusing on the measurements of open charm production promise to give a first look at the gluon polarization (ΔG). Future spin experiments such as COMPASS (CERN) are designed to measure ΔG and will continue to unveil the spin structure of the nucleon.

2 Theoretical Motivation for Deep Inelastic Scattering

Deep inelastic lepton nucleon scattering (DIS) is a process for which the momentum transfer is so large and therefore the resolved distance so small that the nucleon's substructure can be probed. The following inevitable break-up of the target nucleon manifests the inelasticity of this process.

2.1 DIS Formalism

2.1.1 Kinematics

Deep inelastic scattering of a charged lepton e off a nucleon N,

$$e + N \rightarrow e' + X \quad ,$$

to an outgoing lepton e' and a hadronic final state X is an electro-weak process. In lowest order, it can be described as neutral boson exchange (Z^0, γ) between the two particles. Because at HERMES the center of mass energies are well below the Z^0-mass, the one-photon exchange is the dominant process (fig.2.1).

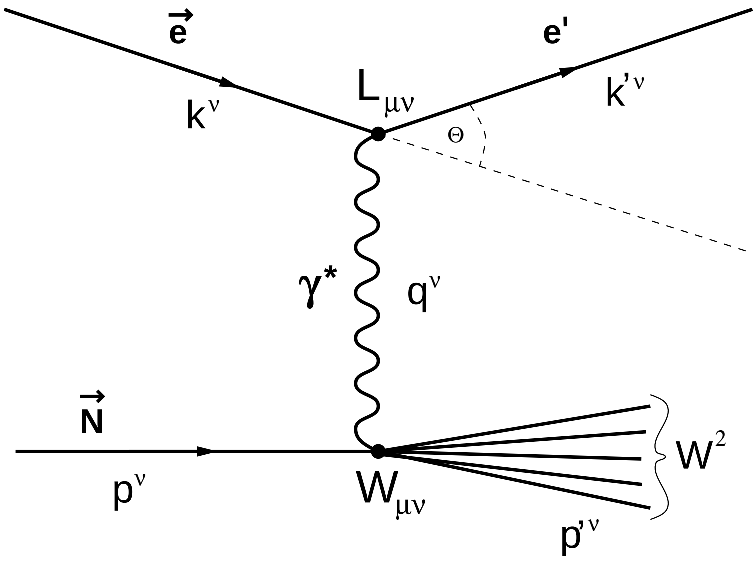

Figure 2.1: The Feynman Graph of deep inelastic scattering in the one-photon exchange approximation.

In the lab-frame, the incoming lepton e with four-momentum $k^\nu = (E, \vec{k})$ scatters with an angle Θ into its outgoing state $k'^\nu = (E', \vec{k}')$ by emitting a virtual photon γ^*. The four-momentum squared of the virtual photon is:

$$q^2 = (k - k')^2 \quad . \tag{2.1}$$

Assuming azimuthal symmetry and neglecting the electron mass ($k^{\nu}_{lab} = (E, E \cdot \vec{u_z})$) it can be expressed in the lab-system as:

$$-q^2 = Q^2 \overset{\text{lab}}{=} 4EE' \sin^2 \frac{\Theta}{2} \quad , \tag{2.2}$$

where E (E') is the energy of the incoming (outgoing) lepton. The negative momentum transfer squared Q^2 is positive and a measure of the scale the photon can resolve ($\lambda \propto \frac{1}{Q}$). The energy transferred by the virtual photon is:

$$\nu = \frac{p \cdot q}{M_N} \overset{\text{lab}}{=} E - E' \quad . \tag{2.3}$$

The nucleon with mass M_N and four-momentum p is assumed to be at rest in the lab-frame ($p^{\nu}_{lab} = (M_N, \vec{0})$). With p', the momentum sum of the outgoing hadron fragments X, the invariant mass squared of the hadronic final state W^2 can be expressed as:

$$W^2 = p'^2 \overset{\text{lab}}{=} M_N^2 + 2M_N\nu - Q^2 \quad . \tag{2.4}$$

DIS can be thought of as a scattering process in which $\frac{1}{Q}$ is much less than the size of the nucleon so that the lepton scatters off a single quark. Furthermore, W has to be large enough (> 2 GeV) to avoid excitations of hadronic resonances. For a further description, two dimensionless *scaling variables* are introduced:

$$y = \frac{p \cdot q}{p \cdot k} \overset{\text{lab}}{=} \frac{\nu}{E} \tag{2.5}$$

and

$$x = \frac{Q^2}{2\, p \cdot q} \overset{\text{lab}}{=} \frac{Q^2}{2M_N\nu} \quad (< 1 \text{ in DIS}) \quad . \tag{2.6}$$

Here y is the energy fraction transferred to the nucleon while x is a measure of the momentum of the struck quark (sect. 2.2). Deep Inelastic Scattering is formally defined as lepton-nucleon scattering for Q^2, $\nu \to \infty$ at fixed x. All the variables defined in eq.2.1 - 2.6 are Lorentz-invariant and can be calculated from the kinematics of the outgoing lepton e'. Thus, it is possible to perform a structure measurement of the nucleon by detecting just the scattered $e^{\pm}$ (*inclusive measurement*).

2.1.2 The DIS Cross-Section

The inclusive DIS cross-section[1] can be written as the matrix product of the leptonic tensor $L_{\mu\nu}$ and the hadronic tensor $W^{\mu\nu}$:

$$\frac{d^2\sigma}{dE'\, d\Omega} = \frac{\alpha^2}{Q^4} \frac{E'}{E} L_{\mu\nu} W^{\mu\nu} \quad , \tag{2.7}$$

with the fine structure constant $\alpha = \frac{1}{137}$. More detailed descriptions can be found in [1] [2] [3] [4].

[1] $\hbar \to 1$ and $c \to 1$

The tensor $L_{\mu\nu}$ describes the interaction at the leptonic vertex in the one-photon exchange approximation:

$$L_{\mu\nu} = \sum_{s'_e} \bar{u}(k', s'_e)\gamma_\nu u(k, s_e)\bar{u}(k, s_e)\gamma_\mu u(k', s'_e) \quad . \tag{2.8}$$

Employing some trace theorems and summing over the spin orientations s'_e of the final state [5] eq.2.8 leads to:

$$\begin{aligned} L_{\mu\nu} &= Tr(\not{k}' + m_e)\gamma_\nu(\not{k} + m_e)\frac{m_e + \gamma_5 \not{s}_e}{2m_e}\gamma_\mu \\ &= 2(k_\mu k'_\nu + k_\nu k'_\mu - g_{\mu\nu}(k \cdot k' - m_e^2) - i\epsilon_{\mu\nu\alpha\beta}\, q^\alpha s_e^\beta) \\ &\approx 2(k_\mu k'_\nu + k_\nu k'_\mu - g_{\mu\nu}\; k \cdot k' - i\epsilon_{\mu\nu\alpha\beta}\; q^\alpha s_e^\beta) \end{aligned} \tag{2.9}$$

The spin four-vector s_e^ν of the incoming lepton,

$$s_e^\nu = \frac{1}{2}\,\bar{u}(k, s_e)\gamma^\nu\gamma_5 u(k, s_e) \quad , \tag{2.10}$$

is defined to be $s_e^\nu = (0, \vec{s_e})$ in the rest frame of the particle.

The hadronic tensor $W^{\mu\nu}$ cannot be calculated directly because the absorption of the virtual photon by the nucleon is non-perturbative in QCD. To overcome this difficulty a general ansatz for $W_{\mu\nu}$ can be made using the fact that it depends only on p^ν, q^ν and s_e^ν. Using time-reversal invariance and parity conservation of the strong interaction, together with current conservation at the hadronic vertex it follows that:

$$\begin{aligned} W_{\mu\nu} = \; & F_1 \cdot \left(\frac{q_\mu q_\nu}{q^2} - g_{\mu\nu}\right) + \; F_2 \cdot \frac{1}{p \cdot q}\left(p_\mu - \frac{p \cdot q\; q_\mu}{q^2}\right)\left(p_\nu - \frac{p \cdot q\; q_\nu}{q^2}\right) \\ & + \; g_1 \cdot \frac{i}{p \cdot q}\,\epsilon_{\mu\nu\alpha\beta}\; q^\alpha\; s_N^\beta + \; g_2 \cdot \frac{i}{(p \cdot q)^2}\,\epsilon_{\mu\nu\alpha\beta}\; q^\alpha(p \cdot q\; s_N^\beta - s_N \cdot q\; p^\beta) \quad . \end{aligned} \tag{2.11}$$

This expression is valid for a spin $\frac{1}{2}$ target with polarization vector s_N^ν. The *structure functions* of the nucleon, $F_1(x, Q^2)$, $F_2(x, Q^2)$, $g_1(x, Q^2)$, and $g_2(x, Q^2)$, appear as coefficients in eq.2.11 and contain the actual structure information. In particular g_1 and g_2, the *spin-structure functions* of the nucleon, are of recent scientific interest. Since all spin-independent terms in eq.2.9 and 2.11 are symmetric in $\mu\nu$ and all spin-dependent terms are anti-symmetric, non-zero spin-dependent terms in the cross-section (eq.2.7) will contain only terms with both spins, s_N^ν and s_e^ν. Therefore, the projectile and the target must be polarized in an experiment to measure g_1 or g_2 (SMC, SLAC, HERMES).

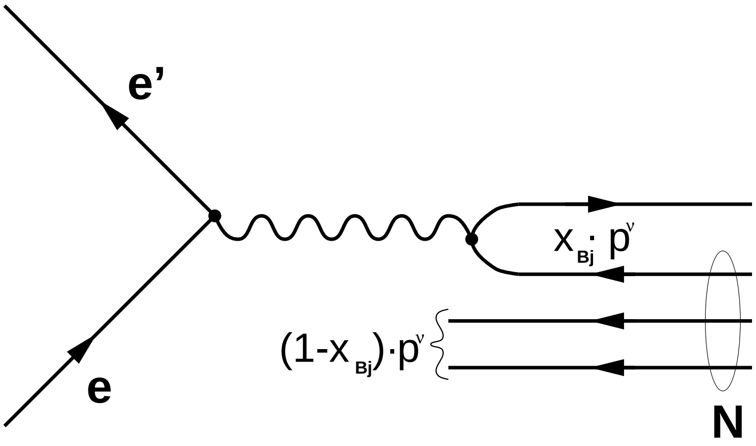

Figure 2.2: DIS in the Breit frame (infinite momentum or brick-wall frame). The quark that carries the fraction x_{Bj} of the nucleon's momentum turns around when hit by the virtual photon.

2.2 Scaling Behaviour

The unpolarized DIS cross-section can be calculated by contracting $L_{\mu\nu}$ with $W^{\mu\nu}$ in eq.2.7, averaging over initial, and summing over all final spin orientations:

$$\frac{d^2\sigma}{dE'\,d\Omega} = \frac{4\alpha^2 E'^2}{Q^4}\left(\frac{2F_1(x,Q^2)}{M_N}\sin^2\frac{\Theta}{2} + \frac{F_2(x,Q^2)}{\nu}\cos^2\frac{\Theta}{2}\right) \quad . \tag{2.12}$$

An alternate approach is to see the lepton simply as a provider of the virtual photon. The unpolarized cross-section can then be expressed as the sum of the longitudinal and transverse photon-absorption cross-section (σ_T and σ_L) of the nucleon:

$$\frac{d^2\sigma}{dE'\,d\Omega} = \frac{\alpha K}{2\pi^2 Q^2}\frac{E'}{E}\frac{1}{1-\varepsilon}\cdot(\sigma_T + \varepsilon\sigma_L) \quad \text{with} \quad K = \nu - \frac{Q^2}{2M_N} \quad \text{(Hand Convention)} \ , \tag{2.13}$$

where ε is the polarization parameter of the virtual photon:

$$\varepsilon = \frac{1-y}{1-y+\frac{1}{2}y^2} \quad . \tag{2.14}$$

By comparing eq.2.13 with eq.2.12, the ratio of σ_L and σ_T can be expressed in terms of the unpolarized structure functions:

$$R(x,Q^2) = \frac{\sigma_L}{\sigma_T} = (1 + \frac{4x^2M^2}{Q^2})\frac{F_2(x,Q^2)}{2xF_1(x,Q^2)} - 1 \quad . \tag{2.15}$$

For $Q^2 \to \infty$, $R(x,Q^2)$ is measured to go to zero [6] . In this case eq.2.15 leads to:

$$\lim_{Q^2\to\infty} F_2(x) = 2xF_1(x) \qquad \text{(Callan – Gross Relation)} \ . \tag{2.16}$$

The phenomenon that for $Q^2 \rightarrow \infty$, F_1 and F_2 become a function of x only is called *(Bjørken-)scaling*:

$$\lim_{Q^2 \rightarrow \infty} F_{1,2}(x, Q) = F_{1,2}(x) \quad . \tag{2.17}$$

The underlying reason is the elastic scattering on a point-like spin $\frac{1}{2}$ constituent of the nucleon. This can also be seen by comparing eq.2.12 with the e - μ cross-section or inserting 'structure functions' for Dirac-point particles (charge e_q) into eq.2.12:

$$\begin{aligned} F_1^{point} &= e_q^2 \, \frac{Q^2}{4M_N} \, \delta\left(\nu - \frac{Q^2}{2m_q}\right) = \frac{1}{2} \, e_q^2 \, x \, \delta\left(1 - \frac{x}{x_{Bj}}\right) \\ F_2^{point} &= e_q^2 \, \nu \, \delta\left(\nu - \frac{Q^2}{2m_q}\right) = e_q^2 \, \delta\left(1 - \frac{x}{x_{Bj}}\right) \end{aligned} \tag{2.18}$$

These *partons* are assumed to carry a fraction x_{Bj} of the four-momentum of the nucleon ($p_q = x_{Bj} p_N$) in the Breit frame (fig.2.2). Equations 2.18 automatically yield the Callan-Gross Relation (eq.2.16) and $x = x_{Bj}$. In this naive *Quark Parton Model* (QPM) the partons are identified with the quarks in the nucleon. Such a parton picture allows the derivation of the four-momentum fraction the struck quark carried in the nucleon from the kinematics of the scattered lepton.

2.3 (Polarized) Parton Distribution Functions

The arguments above lead to the QPM definition of F_1 and F_2 as the sum of the quark distribution functions:

$$F_2(x) = 2\,x\,F_1(x) = \sum_i e_i^2 \, x \, q_i(x) \quad , \tag{2.19}$$

where the function $q_i(x)$ gives the probability to find a (anti-)quark of the flavour i with momentum fraction x in the nucleon. This formalism can be extended to the scattering of a polarized photon on a polarized quark (fig.2.3). Helicity conservation dictates that the photon can be absorbed only by a quark with its z-component of spin opposite to the direction of the photon spin. Thus, by flipping the spin of the target, either the quarks with spin parallel (q^+) or anti-parallel (q^-) to the nucleon spin are probed. Under the assumption that none of the spins has a transverse component, the total cross-section is the sum of $\sigma_{1/2}$ and $\sigma_{3/2}$ with:

$$\sigma_{1/2} \propto q^+(x) \qquad \text{and} \qquad \sigma_{3/2} \propto q^-(x) \quad . \tag{2.20}$$

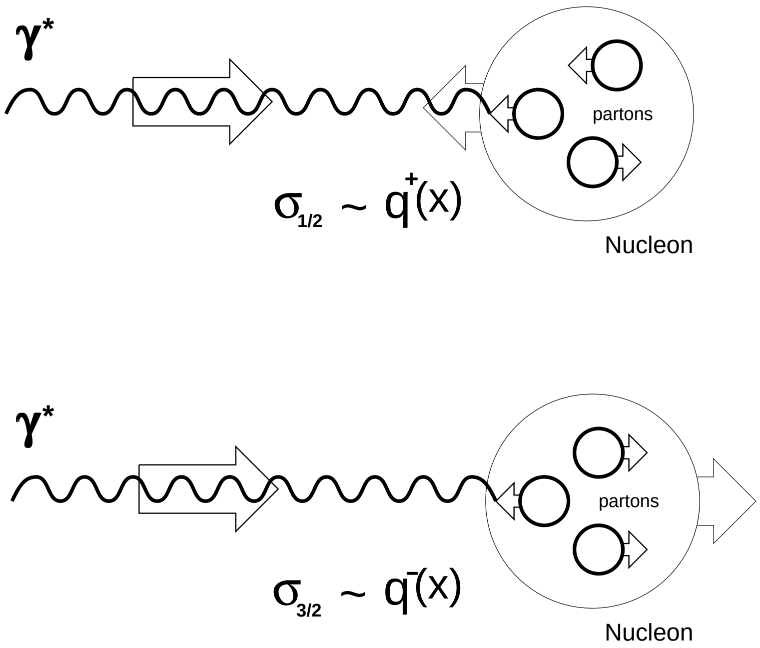

Figure 2.3: Polarized DIS: depending on the target polarization the polarized photon hits a parton with spin parallel (top) or anti-parallel (bottom) to the nucleon spin.

The structure functions are written as follows in the Quark Parton Model:

$$\begin{aligned}
F_1(x) &= \frac{1}{2}\sum_i e_i^2\ (q_i^+(x) + q_i^-(x)) \\
F_2(x) &= \sum_i e_i^2 x\,(q_i^+(x) + q_i^-(x)) \\
g_1(x) &= \frac{1}{2}\sum_i e_i^2\ (q_i^+(x) - q_i^-(x)) \\
g_2(x) &= 0 \qquad \text{(no transverse spin components)}\ .
\end{aligned} \tag{2.21}$$

In this simple model g_2 is zero, which is a reasonable approximation as measurements show [7] . The polarized and unpolarized quark distributions are defined as follows:

$$\begin{aligned}
q(x) &= q^+(x) + q^-(x) \qquad \text{(unpol.)} \\
\delta q(x) &= q^+(x) - q^-(x) \qquad \text{(pol.)}
\end{aligned} \tag{2.22}$$

The equations can be simplified if isospin symmetry between the proton and the neutron is assumed. Furthermore, the contribution of the three lightest quark flavours only (u, d, and s) is considered. This leads to the following definitions:

$$\begin{aligned}
u(x) &= u_p(x) = d_n(x) \\
d(x) &= d_p(x) = u_n(x) \\
s(x) &= s_p(x) = s_n(x) \quad .
\end{aligned} \tag{2.23}$$

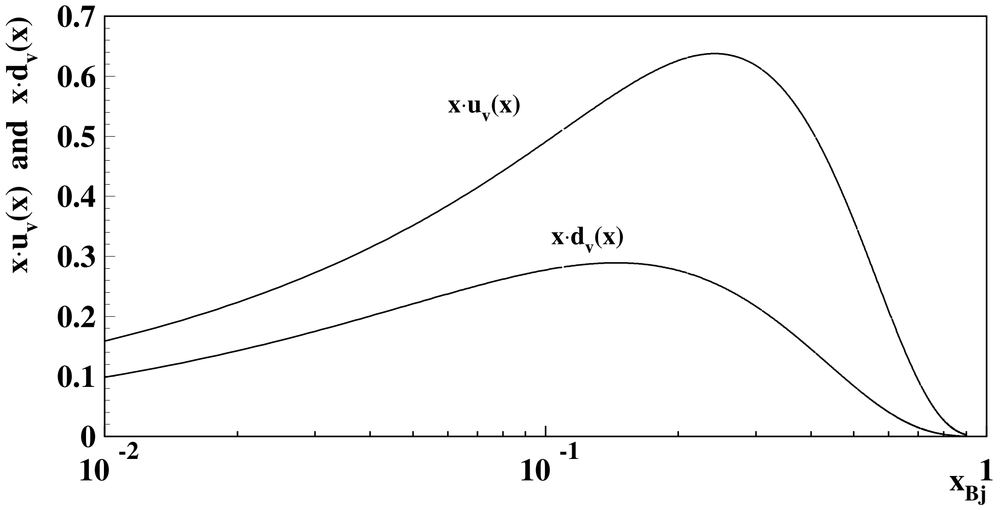

Figure 2.4: The unpolarized valence quark distributions (CTEQ, Standard DIS Scheme [8]).

Moreover, valence quark distributions are defined by:

$$\begin{aligned} u_v(x) &= u(x) - \bar{u}(x) \qquad \text{and} \qquad \delta u_v(x) = \delta u(x) - \delta\bar{u}(x) \\ d_v(x) &= d(x) - \bar{d}(x) \qquad \text{and} \qquad \delta d_v(x) = \delta d(x) - \delta\bar{d}(x) \ . \end{aligned} \tag{2.24}$$

The unpolarized valence quark distributions have been (implicitly) measured and parametrized [8] (fig.2.4). By an integration over x one obtains the correct numbers for the proton:

$$\begin{aligned} &\int_0^1 u_v(x)\ dx = 2 \\ &\int_0^1 d_v(x)\ dx = 1 \\ &\int_0^1 (s(x) - \bar{s}(x))\ dx = 0 \ . \end{aligned} \tag{2.25}$$

The same can be done for the spin-distributions of the proton:

$$\begin{aligned} &\int_0^1 \delta u_v(x)\ dx = \Delta u_v \\ &\int_0^1 \delta d_v(x)\ dx = \Delta d_v \\ &\int_0^1 \delta q_{sea}(x)\ dx = 2\int_0^1 (\delta\bar{u} + \delta\bar{d} + \delta\bar{s})\ dx = \Delta q_{sea} \end{aligned} \tag{2.26}$$

The sea-contribution Δq_{sea} arises from gluons fluctuating into quark/anti-quark pairs in the nucleon. Together with the gluon contribution ΔG and the orbital angular momentum

L_z, the helicity conservation formula for the nucleon can be written as:

$$\frac{1}{2}\underbrace{(\Delta u_v + \Delta d_v + \Delta q_{sea})}_{\Delta\Sigma} + \Delta G + L_z = \frac{1}{2} \ . \tag{2.27}$$

The *nucleon spin crisis* was triggered by EMC measurements that indicated $\Delta\Sigma \approx 0$ [9] . Recent measurements show that the quark contribution to the nucleon spin $\Delta\Sigma$ is $40 \pm 20\%$.

2.4 Semi-Inclusive Electroproduction

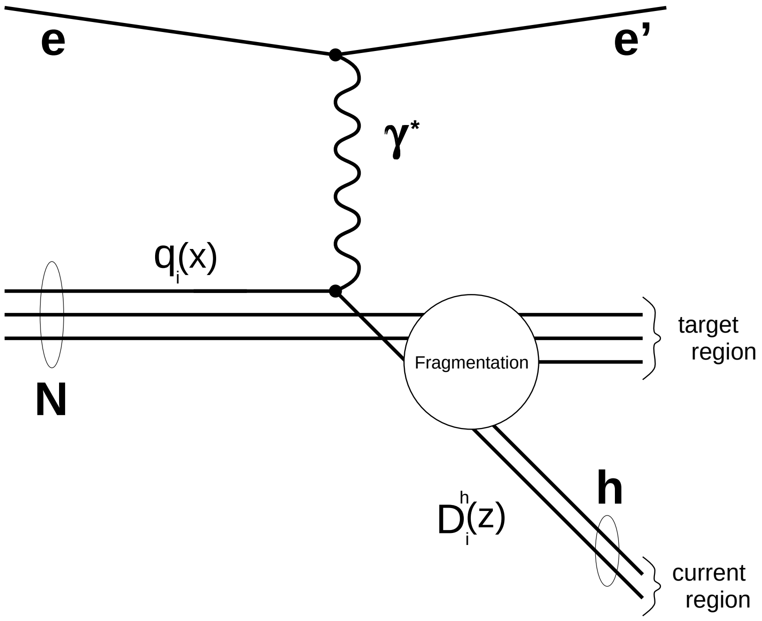

Figure 2.5: Deep inelastic electroproduction of a hadron h.

2.4.1 Fragmentation Functions

The detection of a hadron in coincidence with a DIS electron/positron yields information about the single quark distributions of the target (*semi-inclusive measurement*). The cross-section for the DIS reaction $e + N \rightarrow e' + h + X$ can be expressed in the QPM as:

$$\frac{1}{\sigma_T}\frac{d\sigma^h}{dz} = \frac{\sum_i e_i^2 q_i(x) D_i^h(z)}{\sum_i e_i^2 q_i(x)} \ , \tag{2.28}$$

where σ_T is the total DIS cross section and $z = \frac{E_h}{\nu}$ is the fraction of the energy of the virtual photon (and thus of the struck quark) that is carried away by the hadron. The *fragmentation functions* $D_i^h(z)$ contain the (unknown) structure of the fragmentation process. $D_i^h(z)$ is the probability that a (struck) quark of the flavour i fragments into a hadron h (fig.2.5). The fragmentation functions fulfill momentum conservation:

$$\sum_h \int_0^1 z D_i^h(z) dz = 1 \quad , \tag{2.29}$$

and are normalized to the total average hadron multiplicity $< n_h >$:

$$\sum_i \int_{z_{thresh}}^1 D_i^h(z) dz = < n_h > \quad , \tag{2.30}$$

for all quark and anti-quark flavours i and the threshold z_{thresh} of the process. In eq.2.28 it is assumed that the fragmentation functions depend only on z and the quark distribution functions only on x. In this picture the fragmentation into the hadronic final state is independent from the absorption of the virtual photon by the quark (*factorization*). The outgoing hadrons can be found in two kinematic regions: the *current fragmentation region* that consists of hadrons coming from the fragmentation of the struck quark, and the *target fragmentation region* which contains the debris coming from the rest of the target (fig.2.5). The fragmentation functions are usually defined for hadrons from the current region only. Moreover, they are assumed to be spin-independent and to scale for $Q^2 \rightarrow \infty$.

For charged pions the number of fragmentation functions can be reduced using isospin symmetry and charge conjugation:

$$\begin{aligned} D_1(z) &= D_u^{\pi^+}(z) = D_{\bar{u}}^{\pi^-}(z) = D_d^{\pi^-}(z) = D_{\bar{d}}^{\pi^+}(z) \\ D_2(z) &= D_u^{\pi^-}(z) = D_{\bar{u}}^{\pi^+}(z) = D_d^{\pi^+}(z) = D_{\bar{d}}^{\pi^-}(z) \\ D_s(z) &= D_s^{\pi^+}(z) = D_s^{\pi^-}(z) = D_{\bar{s}}^{\pi^+}(z) = D_{\bar{s}}^{\pi^-}(z) \quad . \end{aligned} \tag{2.31}$$

D_1 is called the *favoured*, D_2 the *unfavoured*, and D_s the *strange* fragmentation function. Observations show that $D_1 > D_2$ since the fragmentation into a hadron is favoured if the hadron contains the struck quark.

2.4.2 Pion Asymmetries

To be sensitive to the flavour of the struck quark, it is necessary to detect the hadron at high enough z and x_F (current region, fig.2.5). The quantity x_F (*x-Feynman*) is defined in terms of the longitudinal momentum of the hadron with respect to the virtual photon, in the photon-nucleon center of mass frame as:

$$x_F = \frac{2\, P_{cm}^{||}}{W} \quad . \tag{2.32}$$

If $x_F > 0$, then the hadron is in the forward hemisphere of the virtual photon frame and hence very likely in the current region. The higher z and x_F the more probable it is that the hadron contains the struck quark [10] . Consequently, a cut on these quantities is necessary for the interpretation of a semi-inclusive measurement.

The spin-distribution of the valence quarks can be found by measuring the pion yields N^{π} for different targets. From the discussion of sect.2.3 and eq.2.28 it is obvious that for a proton target N:

$$N_{\pm}^{\pi^+} \propto \frac{4}{9}u^{\pm}D_1 + \frac{4}{9}\bar{u}^{\pm}D_2 + \frac{1}{9}d^{\pm}D_2 + \frac{1}{9}\bar{d}^{\pm}D_1 + \frac{1}{9}s^{\pm}D_s + \frac{1}{9}\bar{s}^{\pm}D_s \tag{2.33}$$

and

$$N_{\pm}^{\pi^-} \propto \frac{4}{9}u^{\pm}D_2 + \frac{4}{9}\bar{u}^{\pm}D_1 + \frac{1}{9}d^{\pm}D_1 + \frac{1}{9}\bar{d}^{\pm}D_2 + \frac{1}{9}s^{\pm}D_s + \frac{1}{9}\bar{s}^{\pm}D_s \ . \tag{2.34}$$

Here N_+ is the yield in the case the nucleon spin is opposite to the photon spin and parallel to the spin of the probed quark (and vice versa for N_-). The sea quark contributions cancel in the following yield difference :

$$N_{\pm}^{\pi^+-\pi^-} = N_{\pm}^{\pi^+} - N_{\pm}^{\pi^-} \propto \frac{1}{9}\left[4\,\underbrace{(u^{\pm}-\bar{u}^{\pm})}_{u_v^{\pm}} - \underbrace{(d^{\pm}-\bar{d}^{\pm})}_{d_v^{\pm}}\right](D_1 - D_2) \tag{2.35}$$

The pion asymmetry on the proton is formed to eliminate the fragmentation functions and to determine the polarization of the valence quarks:

$$A_{\pi}^{p} = \frac{N_{+}^{\pi^+-\pi^-} - N_{-}^{\pi^+-\pi^-}}{N_{+}^{\pi^+-\pi^-} + N_{-}^{\pi^+-\pi^-}} = \frac{4\delta u_v - \delta d_v}{4u_v - d_v} \ . \tag{2.36}$$

For a ^{3}He target,

$$\begin{aligned} N_{\pm}^{\pi^+} \propto\ & \frac{1}{9}u^{\pm}D_2 + \frac{1}{9}\bar{u}^{\pm}D_1 + \frac{4}{9}d^{\pm}D_1 + \frac{4}{9}\bar{d}^{\pm}D_2 \\ & + \frac{4}{9}u\,D_1 + \frac{4}{9}\bar{u}\,D_2 + \frac{1}{9}d\,D_2 + \frac{1}{9}\bar{d}\,D_1 \\ & + \text{strange contrib.} \end{aligned} \tag{2.37}$$

leads to:

$$A_{\pi}^{^3\text{He}} = \frac{-\delta u_v + 4\delta d_v}{7u_v + 2d_v} \ . \tag{2.38}$$

The pion asymmetry on the deuteron is obtained in a similar way:

$$A_{\pi}^{d} = \frac{\delta u_v + \delta d_v}{u_v + d_v} \ . \tag{2.39}$$

2.4.3 The Goal of this Work

This thesis presents a first HERMES measurement of $\delta u_v(x)$ and $\delta d_v(x)$. With the semi-inclusive HERMES data on ^{3}He (1995) and ^{1}H (1996), the valence quark distributions of the nucleon spin are isolated using eq.2.38 and eq.2.36:

$$\begin{aligned}\delta u_v(x) &= \frac{1}{15}\left[4\left(4u_v(x) - d_v(x)\right) A_\pi^p(x) + \left(7u_v(x) + 2d_v(x)\right) A_\pi^{^3\mathrm{He}}(x)\right] \\ \delta d_v(x) &= \frac{1}{15}\left[\left(4u_v(x) - d_v(x)\right) A_\pi^p(x) + 4\left(7u_v(x) + 2d_v(x)\right) A_\pi^{^3\mathrm{He}}(x)\right]\end{aligned} \tag{2.40}$$

Taking account of the beam and target polarization P_B and P_T, the pion asymmetry is given by the number of counts $n_\pm^{\pi^\pm}$ for each spin state of the target with the corresponding luminosity $L_\pm$ as:

$$A_\pi = \frac{1}{< D >} \frac{(n_+^{\pi^+} - n_+^{\pi^-})L_- - (n_-^{\pi^+} - n_-^{\pi^-})L_+}{(n_+^{\pi^+} - n_+^{\pi^-})L_{p-} + (n_-^{\pi^+} - n_-^{\pi^-})L_{p+}} \tag{2.41}$$

with

$$L_\pm = \int_{\mathrm{time}} L_\pm(t)\, dt \qquad \text{and} \qquad L_{p\pm} = \int_{\mathrm{time}} P_{B\pm}(t) P_{T\pm}(t) L_\pm(t)\, dt \ . \tag{2.42}$$

The depolarization of the virtual photon $D(x, Q^2)$ can be expressed as [11] :

$$D(x, Q^2) = \frac{y(2-y)(1+\frac{1}{2}\gamma^2 y)}{y^2(1+\gamma^2) + 2(1-y-\frac{1}{4}\gamma^2 y^2)(1+R(x,Q^2))} \tag{2.43}$$

with

$$\gamma^2 = \frac{Q^2}{\nu^2} \ . \tag{2.44}$$

The expression for the statistical uncertainty of A_π is given by eq.7.1 in the appendix.

It can be concluded that a semi-inclusive measurement of pion spin-asymmetries on two different targets provides the information to calculate the valence quark distributions of the nucleon spin. The elegance of the approach given in the preceding sections lies in the independence on fragmentation effects, vector meson production (such as $\rho^0 \rightarrow \pi^+ + \pi^-$), and the strange sea. However, this model is only a first-order approximation since it assumes factorization and hadrons from the current region only. Moreover, it neglects contributions from transverse spin orientations, higher twist-effects, and heavy quark flavours.

3 The HERMES Experiment

3.1 The Polarized Beam

3.1.1 The HERA Storage Ring with Spin Rotators

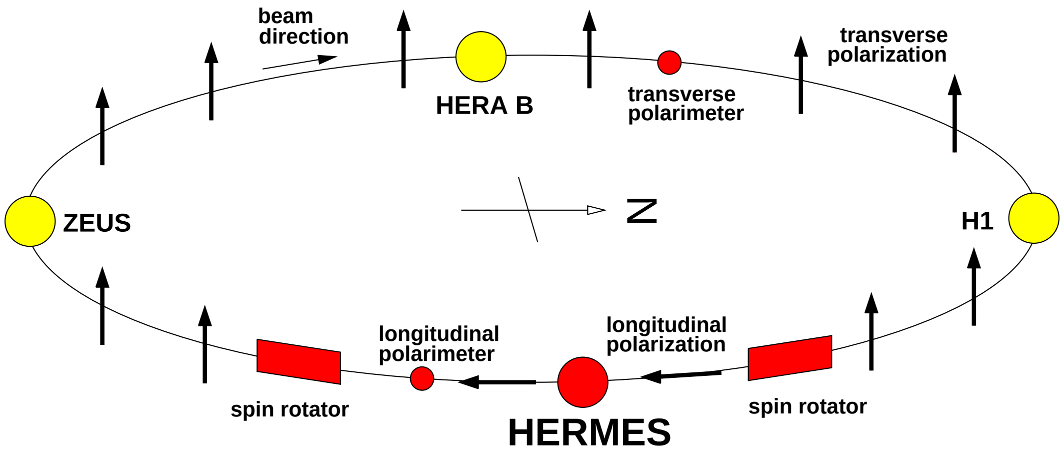

Figure 3.1: The HERA positron ring with spin rotators in Hamburg, Germany. The arrows indicate the direction of the beam polarization.

The 6.3 km long storage ring HERA (Hadron-Elektron-Ring-Anlage) at DESY consists of a 820 GeV proton beam and a 27.5 GeV positron (or electron) beam and accommodates the four high-energy physics experiments H1, ZEUS, HERMES, and HERA-B (fig.3.1). The HERMES experiment is located in the East-Hall and utilizes the positron beam only.

The positron beam becomes transversely polarized by the Sokolov-Ternov effect [12] . This can be explained by the asymmetric probability for a spin flip of a positron radiating synchrotron radiation. One state in the storage ring becomes more populated because the spin flip probability is different for the two spin states. As result the positron beam polarizes itself parallel (anti-parallel for electrons) to the magnetic guiding field of the ring. The polarization $P_{opt}(t)$ for an ideal ring builds up exponentially with a characteristic rise-time τ_{opt} :

$$P_{opt}(t) = \frac{8\sqrt{3}}{15}\left(1 - \mathrm{e}^{-\frac{t}{\tau_{opt}}}\right) \tag{3.1}$$

The Sokolov-Ternov effect competes with depolarizing resonances in the ring which limit the achievable polarization at HERA to about 70% . In this case, an effective rise-time τ can be defined that includes the depolarizing effects ($\tau < \tau_{opt}$). This leads to a more general description for the polarization build-up:

$$P(t) = \frac{8\sqrt{3}}{15}\frac{\tau}{\tau_{opt}}\left(1 - \mathrm{e}^{-\frac{t}{\tau}}\right) \tag{3.2}$$

On the one hand depolarizing effects shorten the rise-time, on the other hand they decrease the maximum achievable polarization. At HERA the measured rise-time τ is approximately 30 minutes at an energy of 27.5 GeV. The typical beam polarization observed at this energy is about 50 - 60%.

Two spin rotators are installed up- and downstream of HERMES to turn the transverse polarization of the positron beam into the longitudinal direction and back. In order to reduce systematic uncertainties for spin-dependent measurements, the spin rotators can also be arranged to give the reverse longitudinal beam polarization.

3.1.2 Beam Polarimetry

The transverse beam polarization is measured by a Compton polarimeter near the HERA West-Hall [13]. Circularly polarized light from a 514 nm argon ion laser is Compton backscattered into a position sensitive calorimeter. The polarization measurement exploits the asymmetric angular distribution of the polarized Compton cross-section which is measured as a small vertical asymmetry by the calorimeter. Because the magnitude of this spatial asymmetry is proportional to the (transverse) positron polarization, it allows a beam polarization measurement. For better systematics the sign of the asymmetry is flipped 90 times per second by switching the helicity of the polarized light with a pocket cell in the laser beam. The transverse polarimeter is calibrated employing eq.3.2 by taking rise-time curves of the polarization (with spin rotators off).

In addition to the transverse polarimeter, a longitudinal polarimeter was built in 1996 to measure the beam polarization in the HERMES area. In contrast to the transverse polarimeter, which measures the angular asymmetry for Compton-scattering, the longitudinal polarimeter measures asymmetries in the total cross-section. The longitudinal polarimeter became operational in 1997 so its measurements are not applicable for the data analysis of this thesis.

3.2 The Polarized Targets

3.2.1 The Internal Target Cell

The target vacuum chamber (fig.3.2), carrying the 40 cm long target cell, is built into the positron storage ring. The target cell, with an elliptical cross-section of $9.8 \times 29.0\,\mathrm{mm}^2$, is made out of 0.051 mm thin aluminum in order to reduce multiple scattering of outgoing particles. The cell is cooled to 25 - 100 K and coated with Drifilm to conserve the polarization of the bouncing atoms within. In order to avoid spin relaxation, the electron and nuclear spins are decoupled by a longitudinal magnetic holding field (0.003 T for ^{3}He, 0.34 T for ^{1}H) [14].

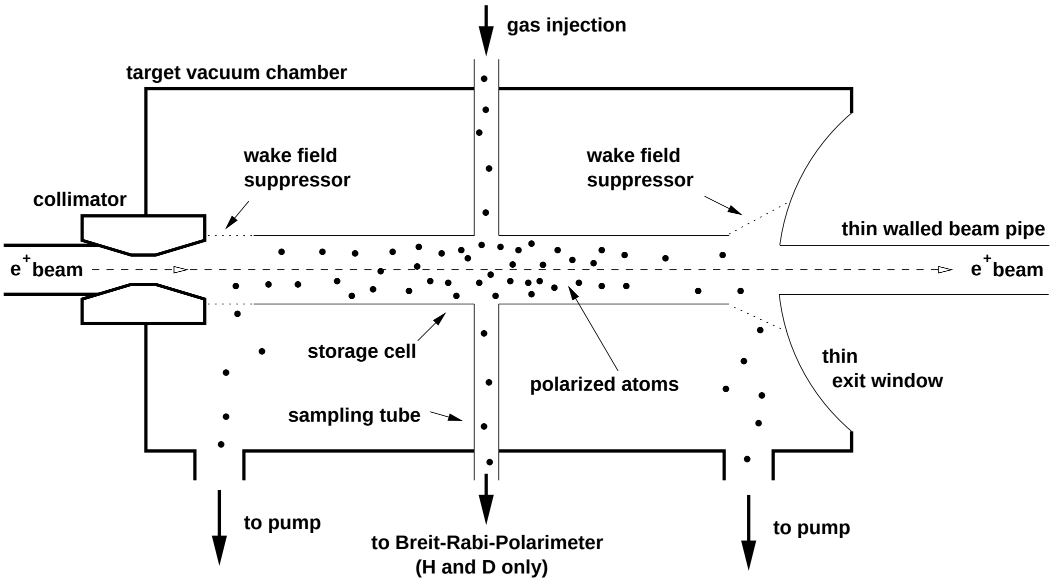

Figure 3.2: The internal gas target in the positron beam.

The polarized gas is injected in the middle of the cell and differentially pumped away at its open ends. Wake field suppressors made of thin titanium meshes provide a smooth conductive transition from the circular beam pipe to the elliptical target cell. This construction prevents the electro-magnetic fields induced by the positron bunches (wake fields) from heating the target. Upstream, the target is protected from synchrotron radiation by a set of collimators. Downstream, a 0.3 mm thin exit window and a beam pipe of similar thickness ensure minimal interaction between the material and the produced particles.

3.2.2 Polarized ^{3}He

The ^{3}He gas flowing into the target cell is polarized by optical pumping with polarized light (fig.3.3). A radio frequency (RF) discharge in the ^{3}He gas populates the metastable 2^3S_1 state. Then, in the presence of a magnetic field, transitions to selected 2^3P_0 hyperfine states are excited by illuminating the quartz pumping cell with 1083 nm circularly polarized infrared laser light. Atoms in the 2^3P_0 states decay to the metastable 2^3S_1 state by emitting unpolarized light. This decay can change the nuclear spin and so the 2^3S_1 atoms become nuclearly polarized. The polarization of the 2^3S_1 atoms is then transferred to the ^{3}He ground-state by metastability exchange collisions [15] .

Maintaining a steady flow of ^{3}He, this technique produces a target with 50 - 60% nuclear polarization [16] . The gas diffuses into the target cell where it reaches a density of $10^{15}\,\frac{\text{nucleons}}{\text{cm}^2}$. In 1995 the target polarization was reversed every 10 minutes to reduce systematic bias on spin-dependent measurements.

The polarization of the target is measured using the 667 nm transition in ^{3}He which is induced by the RF discharge. The de-excitation photons are detected by a polarimeter picking up the light from the quartz cell. The polarimeter determines the circular polarization of the ^{3}He 667 nm transition and allows the determination of the nuclear polarization of the gas [17] .

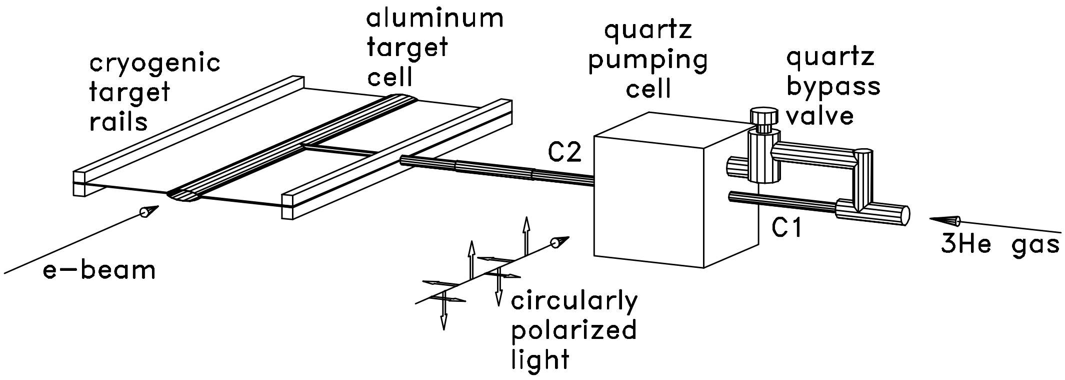

Figure 3.3: The optical ^{3}He pumping system.

A second measurement is provided by the Target Optical Monitor (TOM) that collects photons coming from the target cell by a mirror system upstream. These photons come from decays of atoms which were excited by the positron beam. The polarization of the light from the de-excitation is determined by the TOM and is a measure of the nuclear polarization of the atoms in the storage cell. The TOM measurements are in agreement with the target polarimeter proving that the target gas does not suffer beam induced depolarization. However, the TOM measurements are used for a cross-check only since they cannot compete statistically with the measurements of the target polarimeter.

3.2.3 Polarized ^{1}H

The polarized hydrogen target consists of an atomic beam source (ABS) and a Breit-Rabi polarimeter (BRP), both connected to the storage cell (fig.3.4). The ABS provides the target cell with polarized hydrogen, while the BRP measures the polarization of the gas leaving the cell through the sampling tube.

Using an RF discharge, the dissociator atomizes molecular hydrogen and ejects it through a cooled nozzle into a sextupole system. The sextupole magnets select the upper hydrogen hyperfine states with (electron) quantum number $m_J = +\frac{1}{2}$ by the principle of Stern-Gerlach separation. High frequency transitions, realized by the weak field transition unit (WFT) and the strong field transition unit (SFT), filter the nuclear substates desired. The ^{1}H-beam is directed into the target cell where it is stored at a density of $7 \times 10^{13}\ \frac{\text{nucleons}}{\text{cm}^2}$. Polarizations of up to 95% are achieved with the HERMES hydrogen target. In 1996 a reduction of the systematic uncertainties was achieved by flipping the target polarization every 1 - 3 minutes.

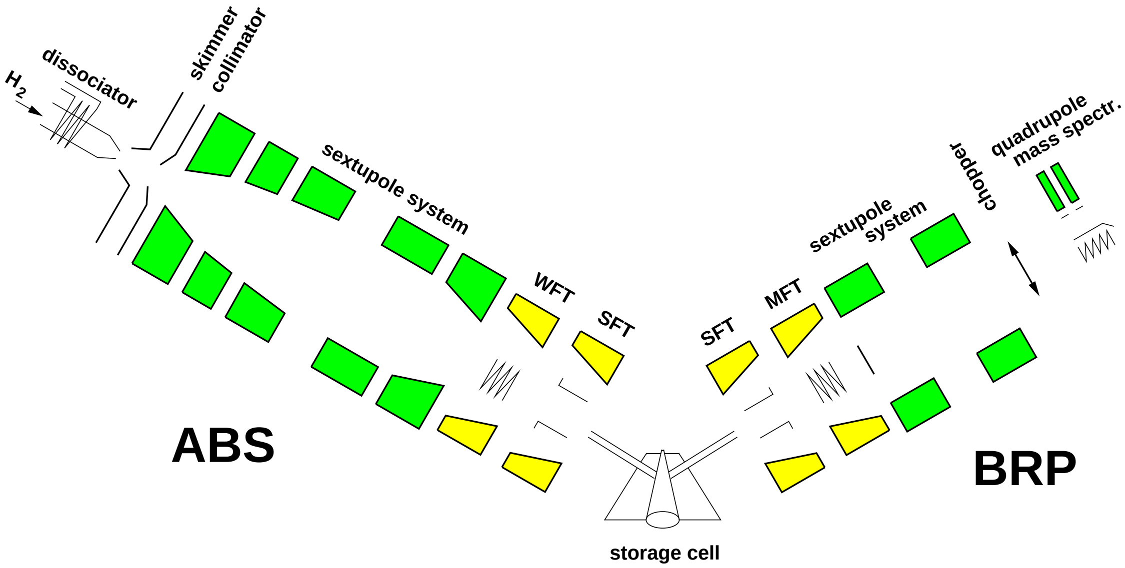

Figure 3.4: Schematic picture of the polarized hydrogen target.

The polarimetry of the target is realized by a structure that is in principle the reverse of the ABS: the Breit-Rabi polarimeter. It focuses a set of hyperfine states into a quadrupole mass spectrometer and deflects the other states. The measurement of the population of different hyperfine state combinations yields the information to calculate the electron and nuclear polarization of the target gas [18] [19] [20] .

3.3 The Spectrometer

The HERMES forward spectrometer (fig.3.5) consists of two identically constructed halves, one above and one below the HERA beam pipes. Both, the positron and the proton beam pass through the middle of the spectrometer and are shielded from the HERMES magnet by a steel plate. Each spectrometer half consists of a set of tracking chambers, (trigger) hodoscopes and four particle identification detectors. A luminosity monitor is installed at the rear of the spectrometer. The acceptance of the spectrometer extends vertically from 40 (shielding plate) to 140 mrad and horizontally to ± 170 mrad. The resulting total angular acceptance from 40 to 220 mrad covers a large kinematic region (fig.5.3).

3.3.1 Magnet and Tracking

The normal conducting HERMES spectrometer magnet deflects charged particles to analyze their momentum. For this purpose, the dipole magnet provides a vertical field with an field integral of $\int B\,dl = 1.3$ T$\cdot$m [21] [22] . Field clamps on both sides of the magnet protect the adjacent detectors from fringe fields. To shield the beam pipes, they are embedded in a 11 cm thick steel plate. The influence of the magnetic field on the positron beam is compensated additionally by a correction coil.

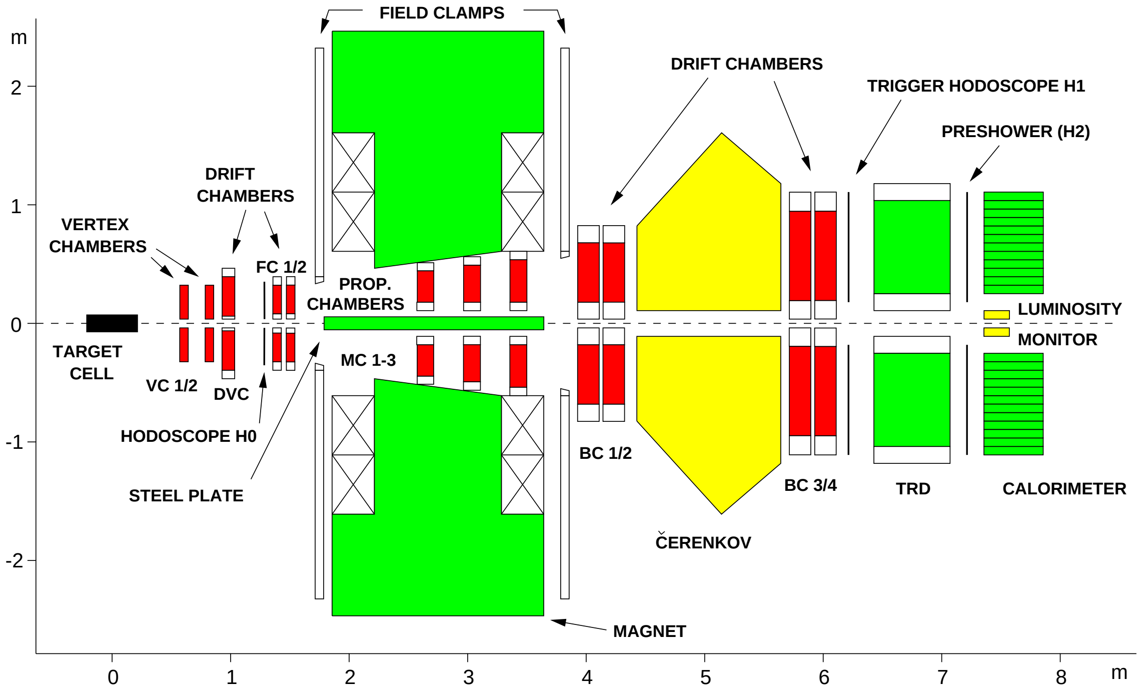

Figure 3.5: A schematic drawing of the HERMES spectrometer.

The HERMES detector contains a series of tracking chambers: two microstrip vertex chambers (VC 1/2) and three drift chambers (DVC, FC 1/2) in front of the magnet; three proportional chambers (MC 1-3) in the magnet; and two pairs of drift chambers (BC 1/2, BC 3/4) behind the magnet. A precise drift-time measurement leads to a spatial resolution of 0.2 -0.3 mm for the drift chambers (FC 1/2, BC 1-4). The FCs only were used to define the partial front track because the VCs and the DVC were not fully operational in 1995 and 1996. Hits in the BCs determine partial back tracks and allow to link the tracks to the responses of the particle identification detectors.

The event reconstruction is done by the HERMES Reconstruction Code (HRC) [23] . It reconstructs the partial front and back tracks from the drift chamber hits. To increase the precision for the front tracks, an additional artificial point in the middle of the magnet (where the partial backtrack points) is added (*forced bridging technique*). The momenta of the particles are measured by the slope differences between front and back tracks to a precision of 0.5% . An iterative fitting algorithm in HRC involving all front tracks finds primary and secondary vertices in the target region.

3.3.2 Particle Identification Detectors

Particle identification (PID) at HERMES is provided by a Čerenkov counter, a transition radiation detector (TRD), a preshower counter, and a lead glass calorimeter. The main task of the PID detectors is to separate reliably (DIS) positrons from hadrons.

The threshold Čerenkov counter is installed (fig.3.6) between the two pairs of back-tracking chambers (BC 1/2, BC 3/4). Particles faster than the speed of light in the detector gas radiate Čerenkov photons ($\beta_{thres} = 1/n_{med}$). The produced photons are reflected by two rows of 10 mirrors each into 20 corresponding photo-multiplier tubes (for each detector half). The thin entrance and exit windows (0.1 mm Mylar and 0.03 mm Tedlar) minimize multiple scattering of the traversing particles.

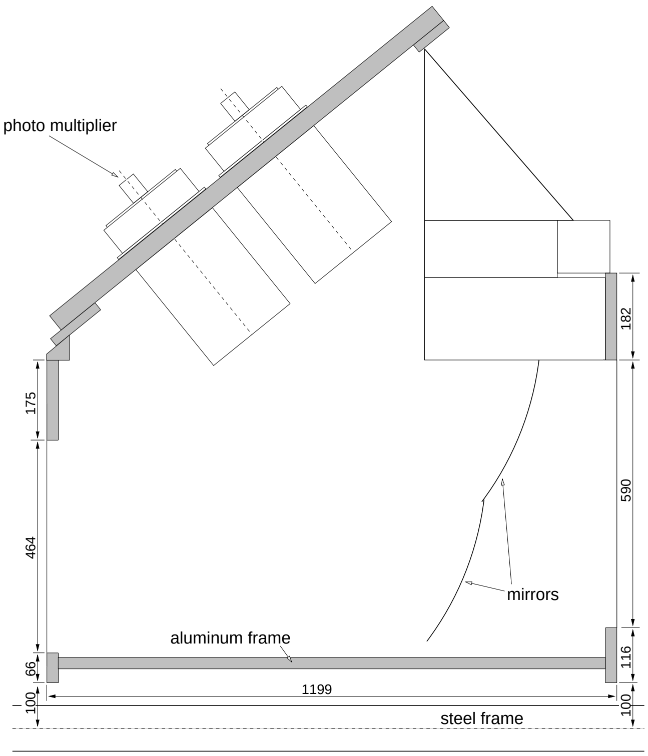

Figure 3.6: The upper threshold Čerenkov counter.

The size of photo-multiplier signals determines the number of photoelectrons (N_e) produced by the Čerenkov photons. Figure 3.7 shows that the majority of the hadrons do not *fire* the counter, meaning they do not produce Čerenkov photons. Since positrons yield about four photoelectrons on average ($\beta = 1$ at HERMES), the Čerenkov counter helps to separate them from hadrons. The momentum threshold for each particle type is given in tab.3.1. The Čerenkov detector can be used to separate pions from other hadrons between the momenta of the pion and kaon threshold. In 1996 the refractive index of the radiator gas was increased in order to gain more identified pions.

The preshower detector is located behind the TRD (see chapter 4). It consists of the hodoscope H2 and 11 mm of lead in front of it. The hodoscopes H2 and H1 consist of 42 vertical plastic scintillator paddles with photomultipliers mounted on the end away from the beam pipe (fig.3.8). Because the thickness of the lead corresponds to two radiation lengths, positrons have a relatively high probability of starting a shower which can be

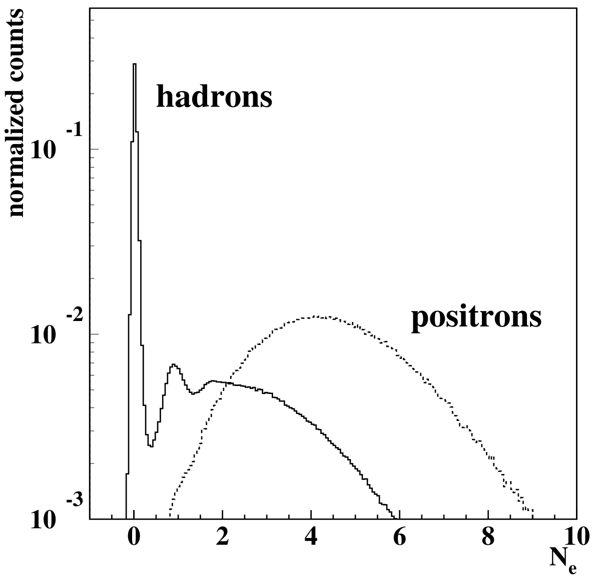

Figure 3.7: The normalized Čerenkov response for hadrons (solid line) and positrons (dashed line) from 1996 data integrated over all momenta.

Table 3.1: Threshold parameters of the Čerenkov counter for two running periods.

running period	1995	1996
radiator gas	N_2	$C_4F_{10}N_2$
n_{med}	1.000298	1.001223
π threshold	5.7 GeV	4.0 GeV
K threshold	20.2 GeV	14.1 GeV
p threshold	38.4 GeV	26.8 GeV

detected in the scintillators. The resulting light is captured by the photo-multipliers. Since a nuclear interaction length is much larger than a radiation length, hadrons have a much lower probability of showering than positrons. Hadrons will give only a minimum ionizing signal in hodoscope H2 (fig.3.9, left).

The lead glass calorimeter follows downstream of the preshower detector. The upper and lower half of the calorimeter can be moved 50 cm away from the beam to avoid radiation damage during beam injection. Each half consists of 42×10 lead glass blocks (9×9 cm) (fig.3.8). Each block is 50 cm long corresponding to 18 radiation lengths. The Čerenkov light from showering particles is collected in photo-multiplier tubes mounted at the rear of each block. Most particles leave signals in a cluster of blocks. The resolution for a 3×3 cluster is $5\%/\sqrt{E_{CALO}\,[GeV]} + 1.5\%$ [22]. By weighting the energies in each block of a cluster, a position resolution of about 1-2 cm is achieved.

The calorimeter and the preshower use the different showering behaviour of cascades induced by an electromagnetic or strong interaction for particle identification. The 18 radiation lengths provided by the calorimeter wall make it most likely that a shower started by a photon or a positron is completely contained in the material. Hence, for photons, positrons, and electrons the ratio of deposited energy to momentum (E_{CALO}/p) is equal to one (fig.3.9, right). Hadrons deposit only a fraction of their energy in the calorimeter ($E_{CALO}/p < 1$) because the nuclear interaction length is much larger than for electromagnetic interactions.

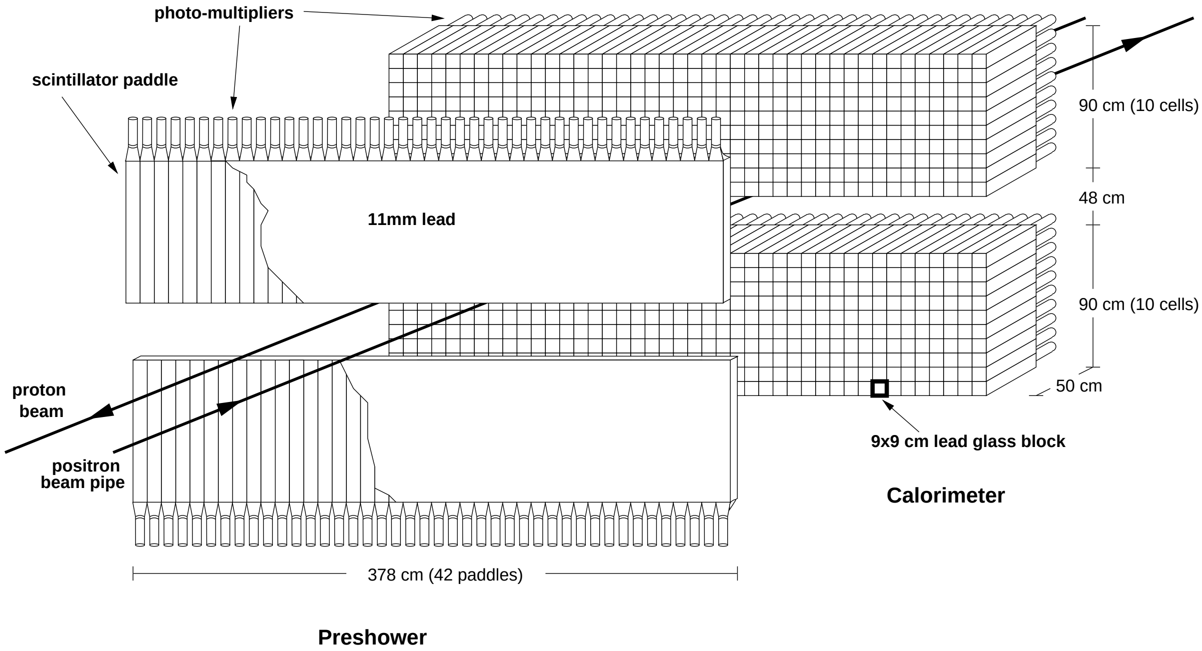

Figure 3.8: Perspective view of preshower detector and calorimeter.

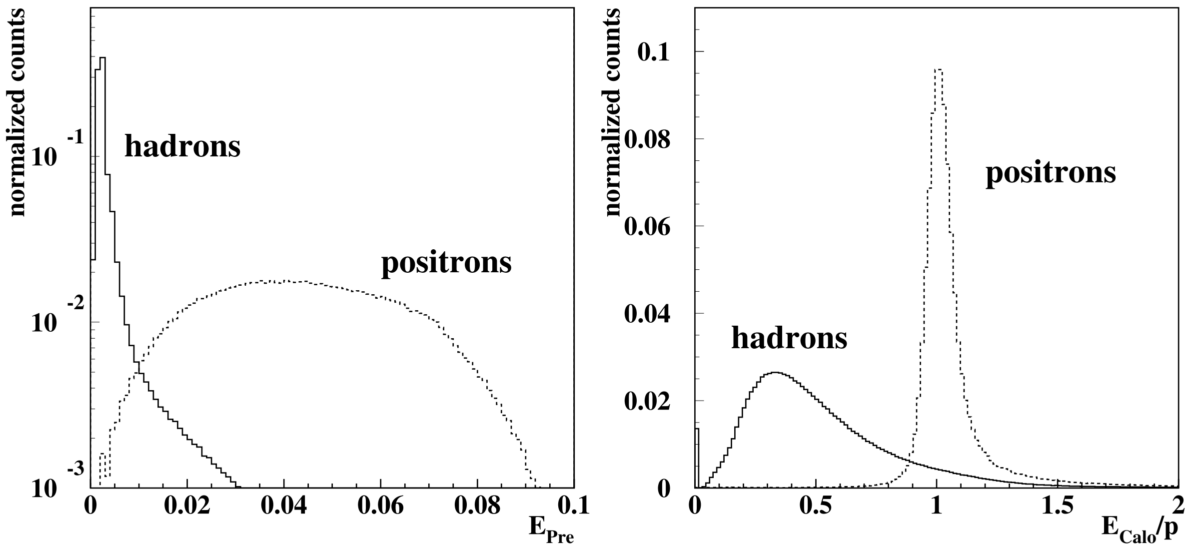

Figure 3.9: The normalized preshower (left) and calorimeter (right) responses for hadrons (solid line) and positrons (dashed line). The whole momentum range is shown (1996).

3.3.3 Luminosity Monitor

The luminosity monitor consists of two small calorimeters installed 7.2 m downstream the target on the left and right of the positron beam line (fig.3.10). The luminosity monitor is moved away from the beam during injection. Each calorimeter of the luminosity monitor consists of an array of 3×4 radiation resistant $NaBi(WO_4)_2$ crystals. An electromagnetic shower produces Čerenkov light in the more than 19 radiation lengths of the crystals. Photo multipliers collect the light and allow a measurement of the deposited energy.

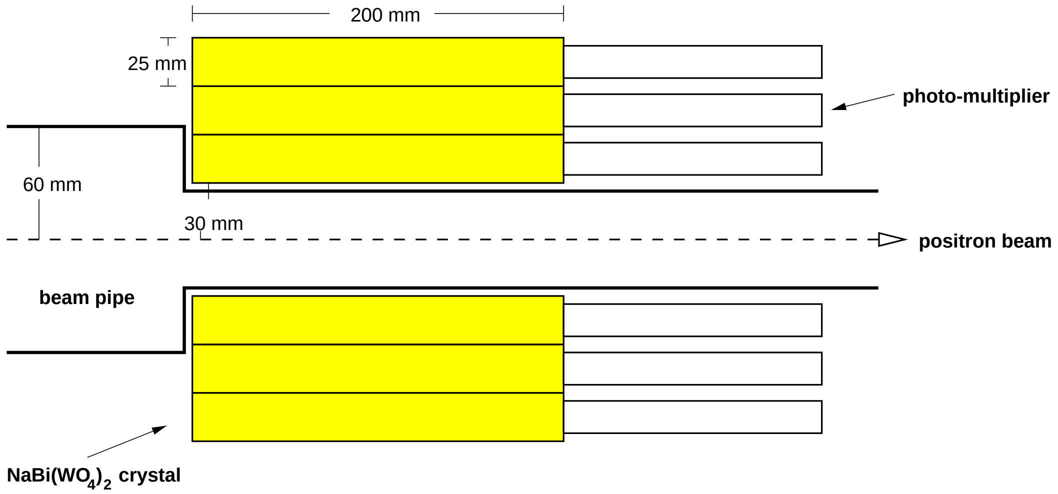

Figure 3.10: The HERMES luminosity monitor at the positron beam line.

The luminosity is measured by determining the rate of Bhabha scattering events where a beam positron collides with an electron of a target atom. (For an electron beam the Møller rate is measured.) The events selected are quasi symmetric Bhabha events where each of the participating particles hits one of the calorimeters. Background is suppressed by requiring coincident hits of more that 5 GeV in each calorimeter. The rate of these events is proportional to the luminosity. False asymmetries from the small spin-dependence of the Bhabha process are corrected in the offline analysis [24] .

3.3.4 Trigger

A first level trigger is an electronic circuit that decides whether an event that occurred in the detector is recorded or not. It is designed to select the physics events desired and reject background events. The most important trigger at HERMES is *Trigger 21*, the DIS trigger. The conditions defining Trigger 21 optimize the chance of recording an event with a DIS positron by requiring the following three conditions to occur in the time window defined by a positron bunch crossing the interaction point:

- Hodoscope H1 and H2 fire. Photons are suppressed by this condition since they do not leave signals in the scintillators. (The threshold for H2 is set *below* the signal of a minimum ionizing particle.)

- In 1996, a signal in hodoscope H0 is required also. In addition to the suppression of photons, this condition reduces the chance of triggers from protons originating from the proton beam by using time of flight to distinguish between forward and backward going tracks.
- The sum of two adjacent calorimeter columns results in more than E_{thr} deposited energy. Thus, rejection of hadrons is achieved.

For unpolarized running and polarized running in 1995 and the beginning of 1996, the *calorimeter threshold* E_{thr} was set to 3.5 GeV. For the second half of the 1996 polarized running the threshold was set to 1.4 GeV. About 4 - 6% of the Trigger 21 events recorded are DIS events. They are filtered in the offline analysis (see sect.5.1.2).

In order to keep the overall trigger rate low enough, most of the other triggers are prescaled, meaning that only every second, fourth, eighth... one is recorded. This prohibits an overload of the data acquisition due to a too high overall trigger rate. In contrast to other triggers, Trigger 21 is not prescaled to collect the largest DIS sample possible.

3.3.5 Data Acquisition, Slow Control and Data Flow

The task of the data acquisition system (DAQ) is to digitize the detector readouts and store the information for the offline analysis. The specific readout electronics for each detector component are hosted in FASTBUS crates mounted in the electronics trailer in the East Hall (fig.3.11). The crates have either a CHI (CERN Host Interface) front end connection to the actual bus or they are linked to such a crate by a CI (Cluster Interconnect). After a trigger has occurred, the FASTBUS event builder at the end of the bus bundles the information from all crates and sends it over an optical link to a FASTBUS/VME interface. The interface also receives (and sends) slowcontrol information (i.e. chamber pressures, target status...) via an optical link from FASTBUS/CAMAC branch drivers located in the electronics trailer. The CAMAC branch driver handles the incoming and outgoing slowcontrol information to and from the CAMAC crates which interface to the detector.

The FASTBUS/VME interface transfers the data to a DEC/ALPHA online cluster. The online cluster buffers the information temporarily on its NFS mounted disk system. The data are sent to the DESY main site via a FDDI link and written locally to EXABYTE or DLT tapes between fills of the storage rings. The information is staged on disk and backed up by a tape robot in the DESY computer centre. Computers in the control room (101) handle the slowcontrol information using a client-server architecture. The DAD (Distributed ADAMO Database) servers collect the slow control data while the clients provide control tools and display the data to the user. The system utilizes a script language called PINK that enables interactive displays. The ADAMO standard (a relational database) is used to store the slowcontrol in cross-referenced tables.

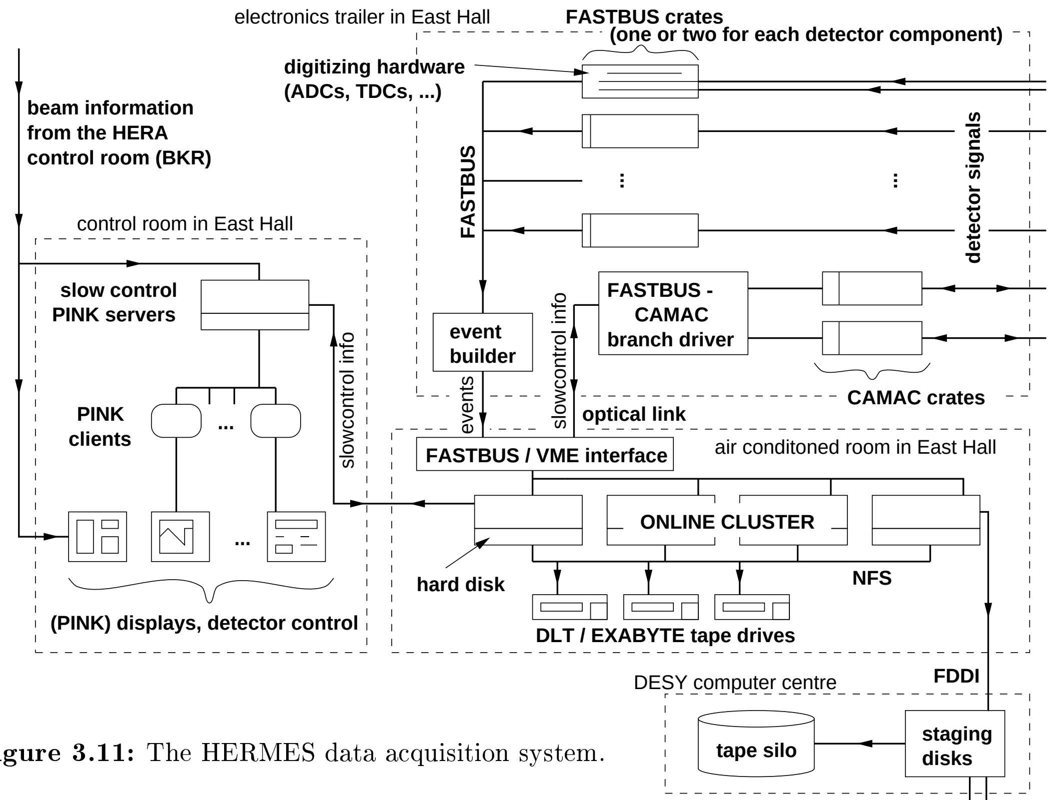

Figure 3.11: The HERMES data acquisition system.

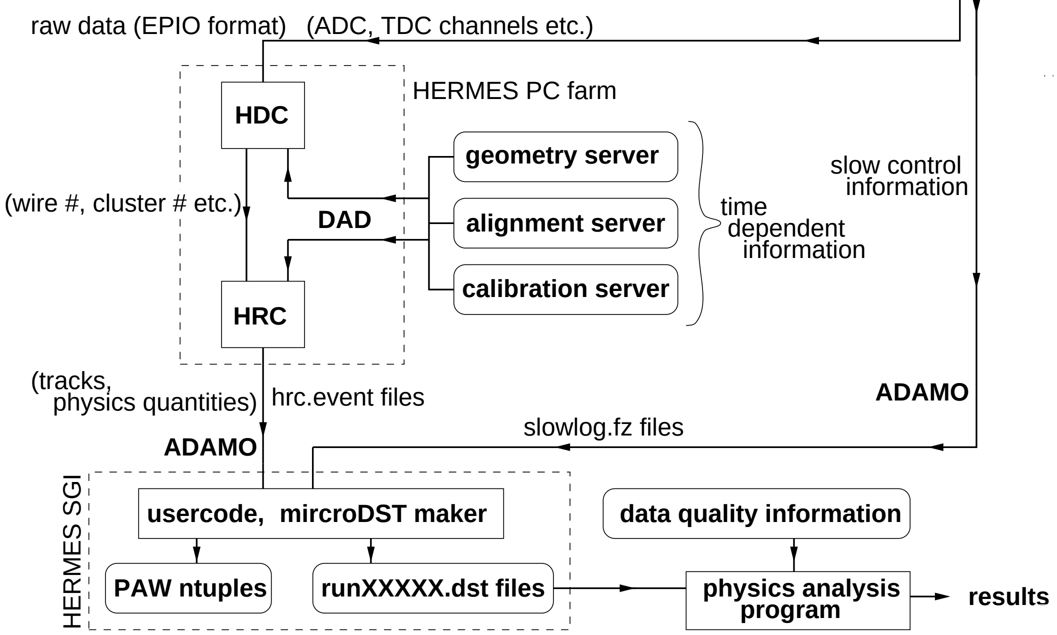

Figure 3.12: Diagram of the offline-dataflow.

After the DAQ system has recorded the raw event data (EPIO format) they are processed by the HERMES Decoder program (HDC) on a high performance PC farm (fig.3.12). HDC translates the electronic detector information, such as ADC or TDC channels, to hit positions and energy depositions, for example. The information is passed on to HRC which calculates the physics quantities as measured by the detector (tracks, angles, momenta ...). HDC and HRC retrieve geometry, calibration and alignment information from a DAD database that is based on a client-server system. The database is updated corresponding to changes in calibrations and detector geometry.

The next step consists of programs that synchronize the HRC event output (hrc.event files) with the slow control information (slowlog.fz files). Usercodes produce data sets (ntuples) that can be processed by PAW (Physics Analysis Workstation) for a convenient analysis. The most common way to handle the data is to process them by a DST-production program. Its output consists of run-wise data files in ADAMO format, called DSTs (Data Summary Tapes). Because the DST files contain the relevant physics quantities only, they enable reasonably fast physics analysis.

Data are recorded at HERMES using three basic time scales. The longest one is the *fill*, the time span of a positron fill in the HERA positron ring. Because the positron beam suffers losses, it has a finite lifetime of 8 - 10 hours. The second time scale is about 10 min long and is called a *run*. This subdivision splits the dataset into small enough pieces for storage. Additionally, the time between runs is used by the system to reinitialize certain hardware components. The smallest time interval is a so called *burst* defined as the time between two scaler readouts. Because it lasts 10 seconds, it allows to split the data with respect to the target polarization state. A burst is also the time scale on which the slowcontrol information is synchronized to the event data.

The DAQ cannot record every event occurring since it is busy for a finite time interval once it has started to record an event. A measure for the efficiency of the data acquisition system is its *livetime*. It is computed burst-wise by the ratio of accepted to generated triggers (usually above 90%). The livetime is needed for cross-section measurements and is also used to rescale the luminosity rate to the data set taken.

4 The HERMES Transition Radiation Detector

4.1 The Detector

The Transition Radiation Detector (TRD) is the main Canadian hardware contribution to the HERMES experiment. It was designed and fabricated at TRIUMF, Vancouver B.C.. This chapter summarizes the physics, the calibration, and the details of the PID using the HERMES Transition Radiation Detector.

4.1.1 Transition Radiation

A highly relativistic point charge can emit electro-magnetic radiation while passing through a boundary between two dielectric media (fig.4.1). This can be explained either by an image charge induced in the second medium, or by the necessity to add an additional

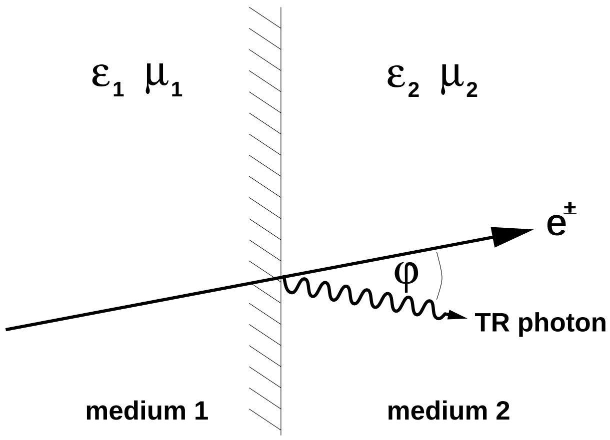

Figure 4.1: When a point charge passes the boundary between two dielectric media, it emits transition radiation (TR).

transition radiation field (TR) to satisfy Maxwell Equations at the boundary (see for instance [25] [26]). The additional TR field appears in form of X-ray photons. For a particle with Lorentz factor γ, the photons are emitted on a cone with an opening angle of $\varphi \propto \frac{1}{\gamma}$ relative to the track. If one treats the first medium as a free electron gas (with plasma frequency ω_p) and the second one as vacuum, the mean energy radiated (W_{TR}) can be expressed as [27]:

$$W_{TR} = \frac{2}{3}\alpha\gamma\omega_p \quad , \tag{4.1}$$

where α is the fine structure constant. The proportionality of transition radiation to the γ factor of the particle enables the identification of highly relativistic ($\beta \approx 1$) particles where conventional, velocity dependent methods (Čerenkov radiation, ionization) fail. Because transition radiation is a relatively small effect ($\alpha = \frac{1}{137}$, see eq.4.1), many surfaces are required for a practical detector.

A closer investigation of the radiation from an equidistant stack of foils (*ideal radiator*) reveals two effects that are due to the coherent nature of transition radiation: an effective threshold in γ and the *formation zone effect*. The threshold effect arises partially from interference terms of TR in adjacent foils, partially from reabsorption of low energy TR quanta by the material. For periodic arrangements the quasi-threshold can be designed to be around $\gamma_{thr} \approx 1000$. The formation zone effect arises from the geometry of the foil stack. Since the electro-magnetic field requires space to reach its equilibrium between surfaces, the foils and gaps cannot be infinitely thin. At least a *formation length* l_f is needed, otherwise the field of the charged particle sees a quasi-continuous medium. Furthermore, saturation of the TR yield above a certain γ_{sat} can be observed.

The parameters γ_{thr}, γ_{sat}, and l_f depend on the material and geometry of the radiator and have to be optimized. Instead of foil stacks, which are difficult to realize [28] for large surfaces, foams and fibers can be used as radiators. Because of their quasi-random structure, they provide dielectric boundaries on a statistical basis. These materials are easy to handle and produce almost the same TR as ideal radiators.

The main principle for building a transition radiation detector is to fabricate a sandwich structure of radiators and X-ray detectors to produce and detect the TR. While the atomic number of the radiator material has to be reasonably low to avoid reabsorption, the X-ray detector has to have a high-Z component for maximal absorption. A good example for such a sandwich structure is the HERMES TRD.

4.1.2 Design of the HERMES TRD

The two halves (top and bottom) of the HERMES TRD are located between the two hodoscopes H1 and H2. Each half consists of six identically constructed modules in a row (fig.4.2). A single module contains a 6.35 cm thick matrix of polypropylene/polyethylene fibers as radiator in front of a 2.54 cm thick multi-wire proportional chamber (MWPC). The MWPC is filled with a mixture of 90% Xenon and 10% CH_4 and detects the generated transition radiation photons as well as the energy lost by the charged particle through ionization ($\frac{dE}{dx}$). The anode wires of the MWPC are strung vertically every 1.27 cm. Thus, the signals are resolved horizontally, making it possible to link the single wire responses to the partial backtracks of the particles in an event. The gas volume of each MWPC is defined by two cathode foils the position of which is constrained precisely by a sophisticated gas system in order to keep the gain of the chamber stable. The system maintains a constant differential pressure (± 0.01 mbar) between the chamber itself and two flush gaps on either side of the detector. Carbon dioxide flowing in the flush gaps transports away other gases coming from the outside thus preventing them from diffusing through the cathode foils into the MWPCs. The large active area of $72.4 \times 325\,\mathrm{cm}^2$ of the TRD covers the entire HERMES acceptance.

Positrons leave a larger signal in the MWPC than hadrons because in addition to the higher ionization energy loss, TR photons contribute to the deposited energy (tab.4.1). Thus, it is possible to distinguish incident hadrons from positrons in the HERMES energy range.

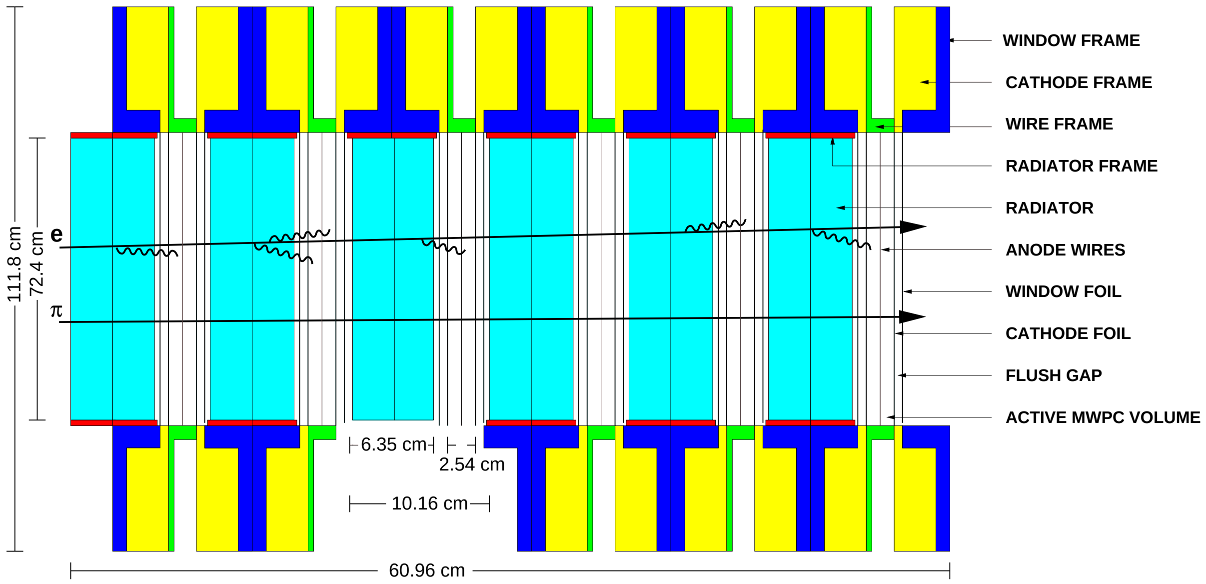

Figure 4.2: One half of the HERMES Transition Radiation Detector. The opening angles of the transition radiation photons emitted by the electron/positron are exaggerated.

Figure 4.3 shows the response of a single module of the TRD. The positrons in this spectrum are overlaid by the high energy tail of a five times larger number of pions. This Landau tail of the pions is caused by delta electrons knocked out by the pions in the radiator and the detector gas. These secondary electrons produce $\frac{dE}{dx}$ and so increase the measured pion signal.

The responses of the six modules are combined into a truncated mean value ($\mathrm{TRD_{tmean}}$) to achieve a reasonable separation between positrons and hadrons. The truncated mean is the average value of the five lowest module responses. Throwing away the highest response reduces the pion tail and the positrons in the spectrum can be separated (fig.4.4). The averaging of the five module responses leads to a better separation because the value tends toward the mean value of the statistically occurring transition radiation. Furthermore, TR photons produced in one of the first modules can 'punch through' several MWPCs and can be detected by one of the subsequent modules, hence increasing the positron/pion discrimination.

Table 4.1: Effects that contribute to the energy deposition in the MWPC of the TRD for particles at $p = 5\,\mathrm{GeV}$.

particle	γ	effect in MWPC
pion	36	dE/dx (10 - 12 keV)
positron	9800	dE/dx + TR (1 - 100 keV)

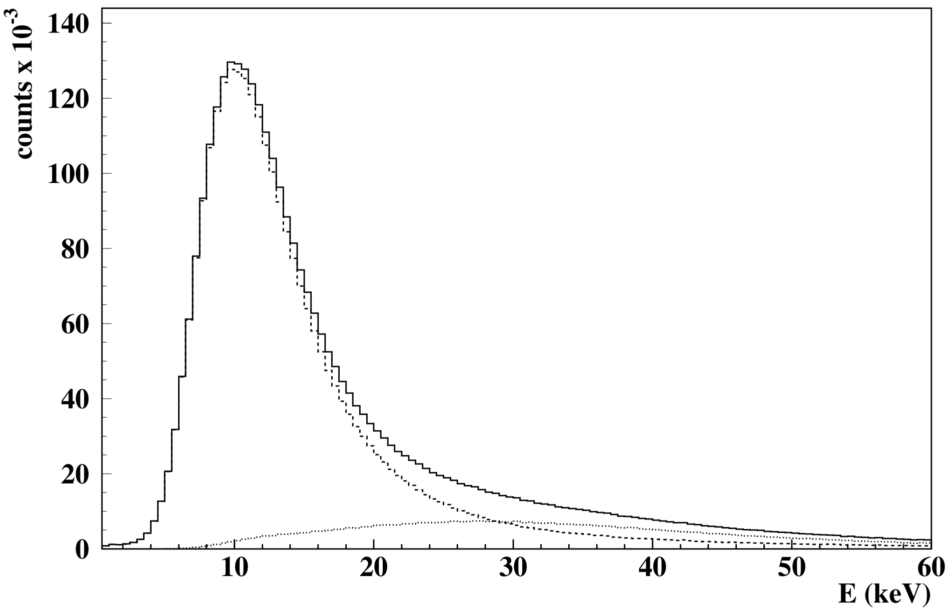

Figure 4.3: Response of TRD module number 3 from selected fills from 1996 (solid line). The response is the sum of a hadron (dashed line) and a positron (dotted line) contribution. The positron/hadron samples are determined by hard cuts on the other detectors (see tab.4.2).

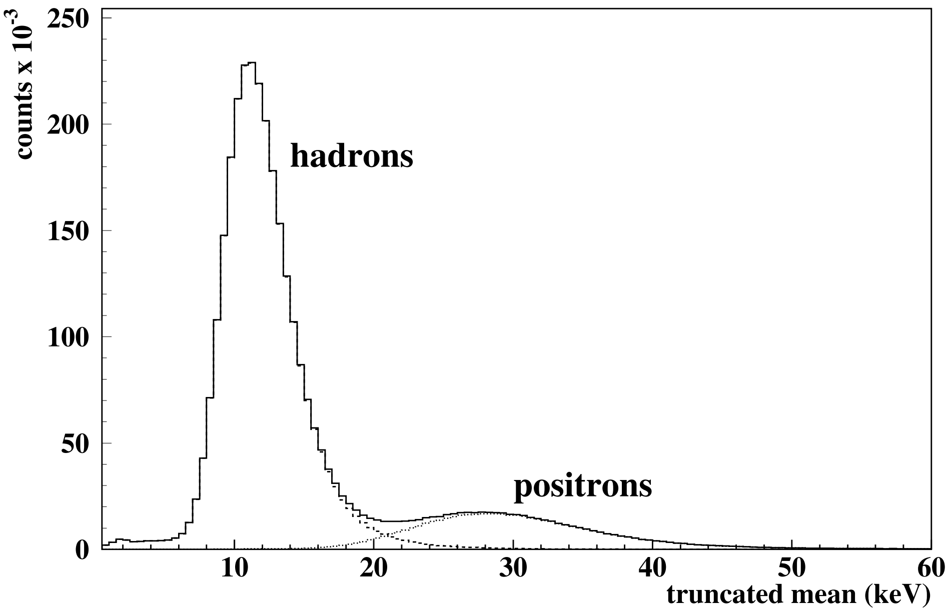

Figure 4.4: Truncated mean of the six TRD modules from selected fills from 1996 (solid line). The hadron response is displayed as dashed line, the positron response as dotted line. Both samples are determined by hard cuts on the other detectors (see tab.4.2).

4.1.3 Atmospheric Pressure Correction of the TRD Response

The TRD response has to be calibrated run by run since the gains of the proportional chambers of the TRD are not entirely stable. The gain varies with the absolute pressure of the detector gas and while the differential pressure is controlled, the chambers follow atmospheric pressure. The pion-peak positions of the single module spectra are set to a fixed value (11.25 GeV) by scaling the spectrum during the calibration procedure. Prior to the calibration, the TRD data quality has to be checked quasi-online, otherwise malfunctions (e.g. wrong voltage) could be calibrated away.

One crude indicator for a possible malfunction of one of the MWPCs is the non-calibrated value of the pion peak position of the truncated mean. Since this value varies considerably as a function of time (fig.4.5), it is not a sensitive enough indicator. The change of the atmospheric pressure is known to give the main contribution to the effect shown in fig.4.5. This is verified by fig.4.6 which shows that peak position and atmospheric pressure are highly correlated. A linear fit seems to be the most reasonable but a hyperbolic fit is motivated by the fact that the gains of MWPCs are a function of E_{MWPC}/p_{atm}. The empirical fit $f(p)$ leads to a correction of the pion peak position:

$$peak_{corr} = peak - f(p) + 11.25\,\text{keV} \quad \text{with} \quad f(p) = \frac{771.5\ \text{mbar keV}}{p - 913.32\ \text{mbar}} + 4.17\ \text{keV}\ , \quad (4.2)$$

which reduces the scatter of fig.4.5 by about a factor of three (fig.4.7). This new peak position can be used for a data quality check. Any major deviation from the set value (11.25 keV) can now be considered to indicate a problem with TRD operation.

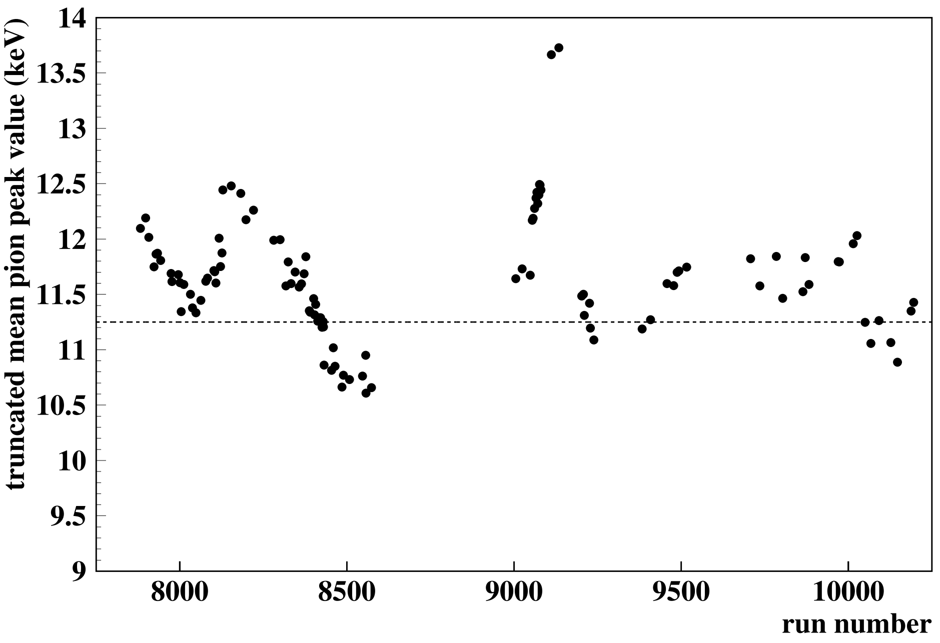

Figure 4.5: Non-calibrated pion peak position for 108 good runs versus run number (1996).

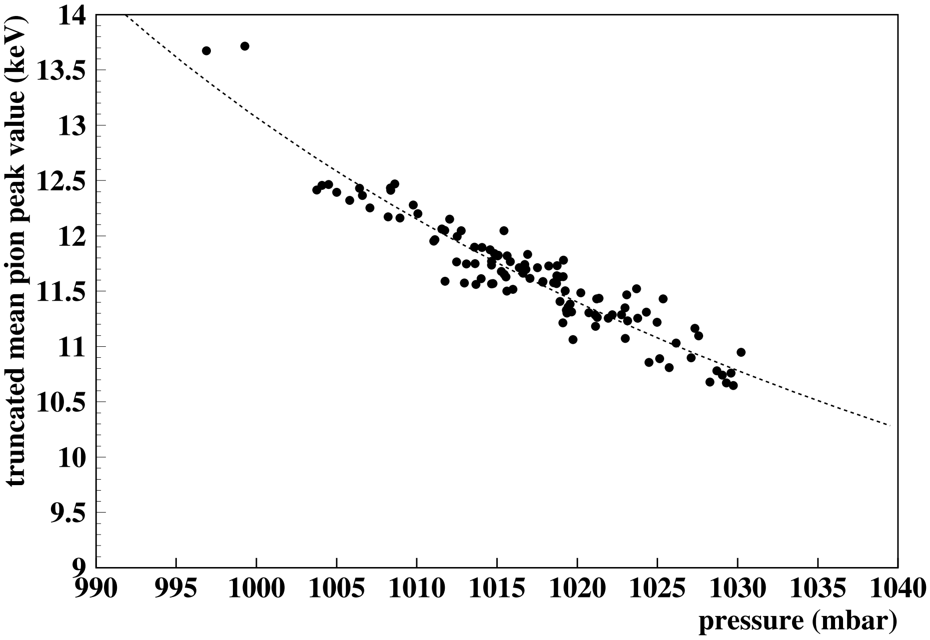

Figure 4.6: Non-calibrated pion peak position for 108 good runs versus atmospheric pressure with a hyperbolic fit $f(p_{atm}) = \frac{771.5 \text{ mbar keV}}{\text{p}_{\text{atm}} - 913.32 \text{ mbar}} + 4.17\,\text{keV}$.

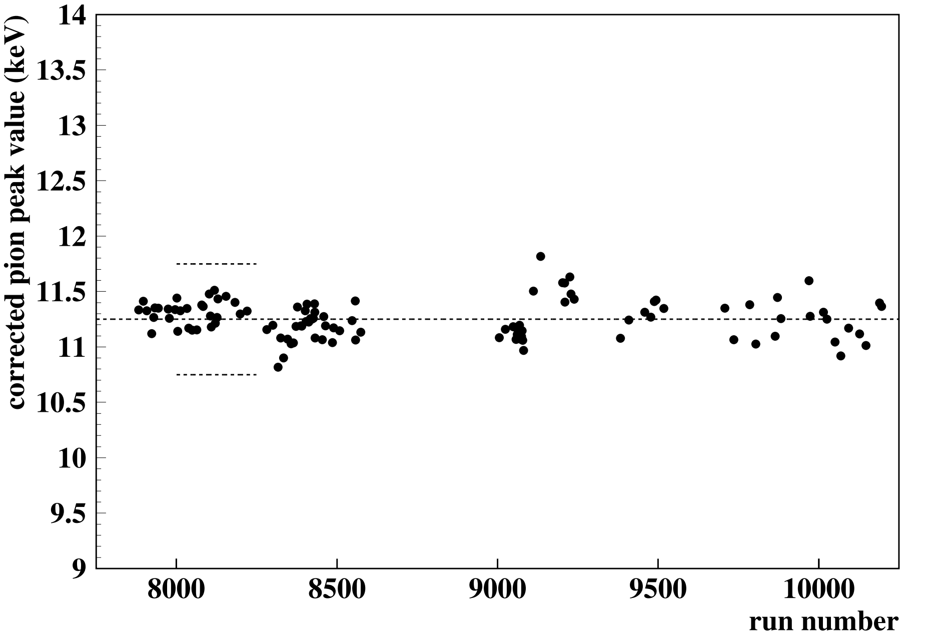

Figure 4.7: Corrected (non-calibrated) pion peak position for 108 good runs versus run number. Correction: $peak_{corr} = peak - f(p_{atm}) + 11.25\,\text{keV}$.

4.2 PID Concepts

4.2.1 Hard Cuts

Because a particle within the HERMES acceptance gives a signal in all four PID detectors, three of them can be used to filter pure particle samples for a study of the response of the fourth one. Strict conditions (*hard cuts*) on each track define a particle subset. Every particle that does not pass the conditions is rejected. The cuts are called *hard* because a clean sample of one particle type is achieved at the price of a low efficiency. For the following TRD analysis, such a set of hard cuts on the other HERMES PID detector responses provides pure subsets of hadrons and positrons (tab.4.2).

A measure for the purity of a sample is the *contamination*. The positron contamination of the hadron sample c_h is defined as the fraction of all measured hadrons that in reality are positrons. (Analogously, c_e is defined.) The overall contaminations c_h and c_e for subsets defined by hard cuts can be estimated by the contaminations for each individual PID detector. (How this can be done, is shown in reference [29] .)

Table 4.2: PID cuts used to obtain clean pion and positron samples for the TRD analysis.

PID detector	quantity	(coll.name)	positron sample	hadron sample
preshower	E_{PRE}	(pulspre)	> 0.025	< 0.004
calorimeter	E_{CALO}/p	(ecalor/p)	> 0.92 and < 1.1	< 0.8
Čerenkov	N_e	(pulcer)	> 1.5	< 0.1
estimated positron contamination of the hadron sample: $c_h = 4.4 \times 10^{-7}$				
estimated hadron contamination of the positron sample: $c_e = 1.6 \times 10^{-3}$				

4.2.2 Likelihoods

A function of the detector signal E that gives the probability for a particle to cause the response E is called a *parent distribution*. For each particle type i and momentum bin p (or any other kinematic quantity the response depends on), a parent distribution $\rho^i(p, E)$ is defined as the normalized detector response such that:

$$\int_{E_{min}}^{E_{max}} dE\, \rho^i(p, E) = 1 \quad . \tag{4.3}$$

The parent distributions can be obtained either from a Monte Carlo simulation of the detector or they can be extracted from data (see sect.4.3.2).

Evaluating parent distributions gives *conditional probabilities*. The name *conditional* refers to the fact that these likelihoods do not take into account the fluxes of the incident particles and hence are not the *real* probabilities (see eq.4.12 in sect.4.3.1). The likelihoods for different detectors can be multiplied to give an overall probability for a track to cause the observed detector responses. Cuts on such likelihood quantities have the advantage of achieving higher efficiencies at the same contaminations obtained by hard cuts. The disadvantage of combined likelihoods lies in the reliance on Monte Carlo simulations to determine efficiencies and contaminations.

4.2.3 Figures of Merit: Efficiencies and Rejection Factors

High *efficiencies* of the clean-up cuts are desired for practical and unbiased analyses of particle samples. The efficiency is the fraction left over after applying one or more cuts to a sample. For the following it is presumed that the main part of the pion distribution is at lower values in the particle spectrum than the positron distribution (see for example figures 3.7, 3.9, or 4.8). A cut placed in the particle spectrum defines the positron sample as all particles that lie above the cut. The positron efficiency is then:

$$\epsilon_e = \frac{e_{m_a}}{e_m} \quad , \tag{4.4}$$

with e_m the total number of positrons and e_{m_a} the number of positrons above the cut. The detector response can be divided into a pion and a positron distribution by hard cuts on the other detector responses (see sect.4.2.1) for the purpose of determining e_m and e_{m_a}.

The pion rejection factor (PRF) defined below is a measure of the ability of a detector to reject pions (hadrons) for a positron detection efficiency ϵ_e. (Usually quoted for ϵ_e= 90% or 95%.) The measured pion rejection factor, η_m, can be computed from the measured total number of pions h_m and the measured number of pions above the cut h_{m_a}:

$$\eta_m = \frac{h_m}{h_{m_a}} \quad . \tag{4.5}$$

One out of η_m hadrons falls above the cut and contaminates the positron sample. The uncertainty on the pion rejection factor is determined by the statistics of h_m and h_{m_a}, the uncertainty of the cut position, and the contaminations of the pion and positron samples used to calculate the PRF. The first two uncertainties are combined and labeled as Δh_m for h_m, and Δh_{m_a} for h_{m_a}.

The influence of the contaminations needs more careful study: the measured numbers h_m and h_{m_a} can be corrected if the fraction of mis-identified positrons in the hadron sample c_h and the fraction of mis-identified hadrons in the positron sample c_e is known. Using the assumption that the pion contamination in the positrons c_e is distributed like the pions (and vice versa), the corrected total number of hadrons h, and the corrected number of hadrons above the positron efficiency cut h_a can be deduced:

$$h = (1 - c_h)h_m + c_e e_m \qquad \text{and} \qquad e = (1 - c_e)e_m + c_h h_m \quad , \tag{4.6}$$

and

$$h_a = h_{m_a} - \frac{e_a}{e} c_h h_m + \frac{h_a}{h} c_e e_m \qquad \text{and} \qquad e_a = e_{m_a} - \frac{h_a}{h} c_e e_m + \frac{e_a}{e} c_h h_m \quad . \tag{4.7}$$

Here e is the corrected number of positrons and e_a the corrected number of positrons above the cut. Using this ansatz, a corrected pion rejection factor η can be derived:

$$\eta = \frac{h}{h_a} = \eta_m \cdot \frac{\delta - 1}{\delta - \frac{\Phi_m}{\Phi_{m_a}}} = \eta_m \cdot C \quad , \tag{4.8}$$

where $\Phi_m = h_m/e_m$ is the measured total flux ratio, $\Phi_{m_a} = h_{m_a}/e_{m_a}$ is the measured flux ratio of the particles above the cut, and $\delta = \frac{(1-c_e)}{c_h}$ is the contamination ratio. An expression for the uncertainty on η can be found in the appendix (eq.7.3). High positron efficiencies and low contaminations lead to:

$$\delta \gg 1 \quad , \quad \frac{\Phi_m}{\Phi_{m_a}\delta} \ll 1 \quad , \quad \text{and} \quad C \approx 1 \ . \tag{4.9}$$

In this case, the correction C is close to and greater than one so that eq.4.5 underestimates the PRF slightly and can therefore be used as a worst-case but reasonable estimate. The contribution from the uncertainty of the contaminations (Δc_h and Δc_e) and the positrons (Δe_m and Δe_{m_a}) to the overall uncertainty in eq.7.3 is then also negligible.

Moreover, the finite resolution of the detector causes an additional uncertainty in the position of the positron efficiency cut due to a smearing of the response spectrum and hence contributes to the uncertainty on the pion rejection. This effect still has to be studied.

4.3 A Probability Analysis of the TRD Response

4.3.1 The Bayesian Approach

The object of the following section is the extraction of the probability P_i that the measured detector responses E_m were caused by the particle type i. The following likelihood method, based on Bayes' Theorem, provides this probability. (For further discussion see [30] .) Momentum dependent parent distributions for pions and positrons are defined for each module m with the signals E_m as normalized responses such that (see sect.4.2.2):

$$\int_{0\,keV}^{100\,keV} dE_m\, \rho_m^i(p, E_m) = 1 \qquad \text{with} \qquad i = e^+, \pi \ . \tag{4.10}$$

Because the responses E_m are caused by the same particle, a combined conditional probability P_i' can be calculated as the product of the single module probabilities $\rho_m^i(E_m)$:

$$P_i'(E_1, \cdots, E_M) = \prod_m^M \rho_m^i(p, E_m) \qquad \text{with} \qquad i = e^+, \pi \ . \tag{4.11}$$

Here M is the number of modules that gave a physically reasonable response (six in 96.2%, non-zero in 99.4% of all cases). P_{e^+}', for instance, is the likelihood that a positron leaves the signals E_m in the TRD.

The next step after computing the conditional probabilities P'_{e+} and P'_h, which are properties of the detector, is to derive the *real probabilities* P_{e+} and P_h that make a statement about the incident particle. Real probabilities give the likelihood for a set E_m to be the result of a positron or a hadron passing through the TRD. They depend on the flux ratio Φ, which is the ratio of hadrons to positrons incident on the detector, and on the conditional probabilities. Together with the condition $P_{e+} + P_h = 1$ this leads to:

$$P_{e+} = \frac{P'_{e+}}{P'_{e+} + \Phi P'_h} \qquad \text{and} \qquad P_h = \frac{P'_h}{P'_h + \Phi^{-1} P'_{e+}} \ , \tag{4.12}$$

where

$$\Phi(p,\Theta) = \frac{\text{number of incident hadrons } (p,\Theta)}{\text{number of incident positrons } (p,\Theta)} \ . \tag{4.13}$$

The flux ratio Φ is a function of momentum and scattering angle because the e-N cross-section depends on these quantities. In practice, Φ is binned in p (momentum) and Θ (scattering angle). $\Phi(p,\Theta)$ cannot be generated directly since it depends on the physics of the experiment and the acceptance of the spectrometer. A Bayesian iteration is necessary to compute the flux ratios Φ from a data set.

For a given set of tracks, the probability analysis is applied starting with an initial estimate Φ_0 for the flux ratios. In each iteration P_{e+} is calculated for every track of the data set. Then the tracks are divided into positrons ($P_{e+} > \frac{1}{2}$) and hadrons ($P_{e+} < \frac{1}{2}$). This provides the flux ratios for the next iteration. The iteration starts with:

$$P^{(1)}_{e+} = \frac{P'^{(1)}_{e+}}{P'^{(1)}_{e+} + \Phi^{(0)} P'^{(1)}_h} \qquad \text{with} \qquad \Phi^{(0)} = \Phi_0 \ \ (= 1 \ \text{ here}) \ . \tag{4.14}$$

Then $\Phi(p,\Theta)^{(1)}$, used in the next iteration step, is calculated from the $P^{(1)}_{e+}$ by:

$$\Phi^{(1)} = \frac{\text{number of tracks with } P^{(1)}_{e+} < 0.5}{\text{number of tracks with } P^{(1)}_{e+} > 0.5} \ . \tag{4.15}$$

This scheme is repeated and can be expressed for the nth iteration as:

$$P^{(n)}_{e+} = \frac{P'^{(n)}_{e+}}{P'^{(n)}_{e+} + \Phi^{(n-1)} P'^{(n)}_h} \qquad \text{and} \qquad \Phi^{(n-1)} = \frac{\text{tracks with } P^{(n-1)}_{e+} < 0.5}{\text{tracks with } P^{(n-1)}_{e+} > 0.5} \tag{4.16}$$

The iterative procedure for $\Phi(p,\Theta)$ usually converges in less than ten steps. Convergence is achieved when $|\Phi^{(n-1)} - \Phi^{(n)}|$ becomes much smaller than the uncertainty of $\Phi^{(n)}$.

4.3.2 Technical Realization

The parent distributions for the TRD are generated from 1995 HERMES data, and most recently also from 1996 data. Runs with any unstable conditions in the spectrometer or the PID detectors are omitted. The necessary identification of positrons and hadrons is done by applying the hard cuts defined in tab.4.2. These cuts on the Čerenkov, preshower, and calorimeter responses have an efficiency of $\approx 50\%$ and produce positron and hadron samples with negligible contaminations.

A binning in E_m of 0.5 keV corresponding to the TRD resolution and a range from 0.5 to 100 keV are chosen for the parent distributions ρ. Sometimes the modules do not respond due to inefficiencies or they are not hit by the particle (e.g. low-energy particles that are bent out of the acceptance by the magnet). Because these module responses contain no information about the actual particle, any response below 0.5 keV is not used in the probability analysis. A relatively broad momentum binning (6 bins for $p \in [0; 30\,\mathrm{GeV/c}]$) is a compromise between the highest possible momentum resolution and reasonable statistics for the distributions. A different momentum binning for positron and hadron parent distributions is used to cover the different momentum dependence as well as the different statistical behaviour (tab.4.3, left).

The results are smooth parent distributions for hadrons and positrons (fig.4.8). The shoulder in the positron parent distribution at 13 keV in fig.4.8 is not due to hadron contamination in the positron sample. It is caused by positrons that only give a $\frac{dE}{dx}$ signal but no transition radiation in the TRD. This effect is also seen in the TRD Monte Carlo simulation [31] .

For the TRD study $\Phi(p, \Theta)$ is binned in 1 GeV/c momentum bins from 1 to 25 GeV/c and in 6 bins for the scattering angle Θ from 40 to 250 mrad (tab.4.3, right). Because the flux ratios vary by up to four orders of magnitude (fig.4.9), they contribute significantly to the particle identification (see next section). The pion rejection of the trigger below 3.5 GeV can be seen in fig.4.9 as a marked decrease in the flux ratio Φ.

Table 4.3: Left: Momentum binning used for the parent distributions in the TRD probability analysis. Right: Binning of the scattering angle for the calculation of Φ.

bin	e^+ (GeV)	π (GeV)
1	0 - 6	0 - 2
2	6 - 12	2 - 4
3	12 - 18	4 - 6
4	18 - 23	6 - 8
5	23 - 30	8 - 10
6		10 - 30

bin	Θ (mrad)
1	40 - 75
2	75 - 100
3	100 - 125
4	125 - 150
5	150 - 175
6	175 - 220

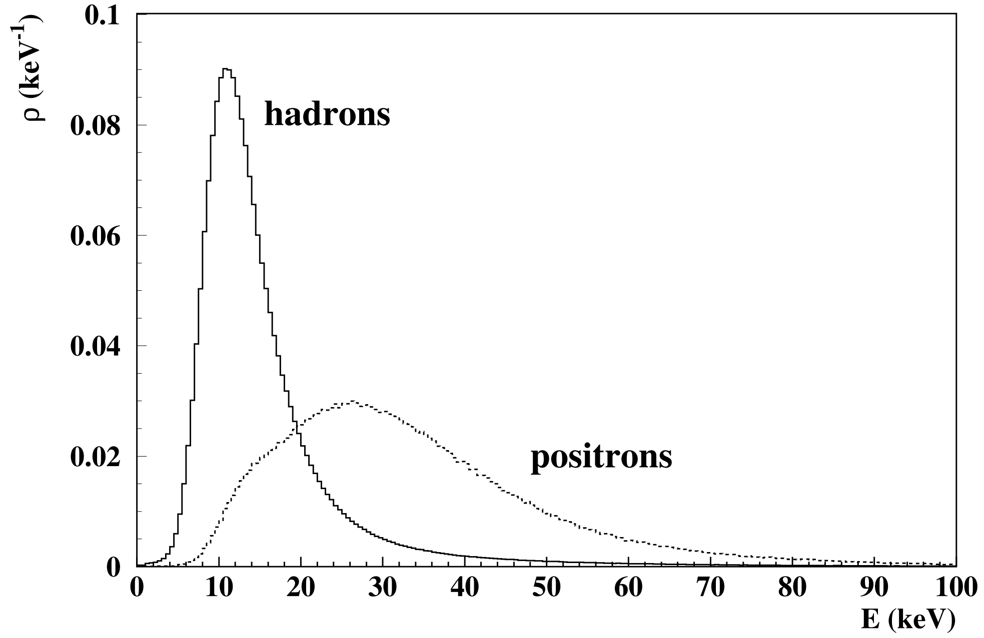

Figure 4.8: Parent distributions for module 1: normalized hadron response ρ_1^h for $p \in [6; 8\,\mathrm{GeV}]$ (solid line); normalized positron response $\rho_1^{e^+}$ for $p \in [6; 12\,\mathrm{GeV}]$ (dashed line).

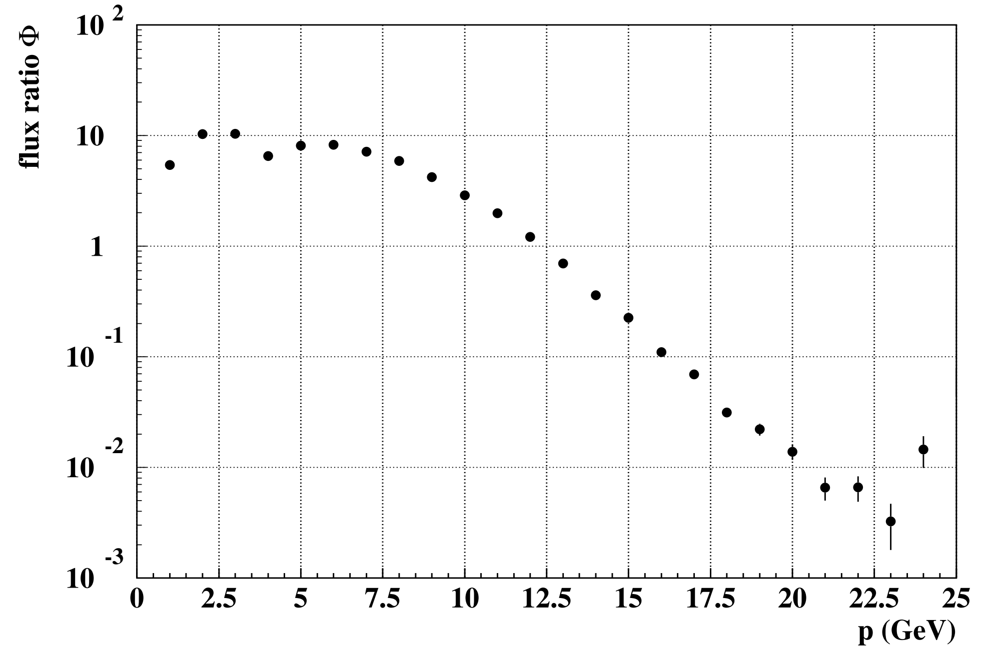

Figure 4.9: Flux ratio $\Phi(p, \Theta)$ from 2×10^6 events from 95 data (only good runs from 3139-5120); $\Theta \in [75; 100\,\mathrm{mrad}]$.

4.4 Results

4.4.1 PID Performance of the TRD

The final result of the probability analysis applied to a set of events is displayed in fig.4.10 [2]. As expected, the positrons concentrate around $P_e = 1$ while the hadrons can be found where the positron probability is zero.

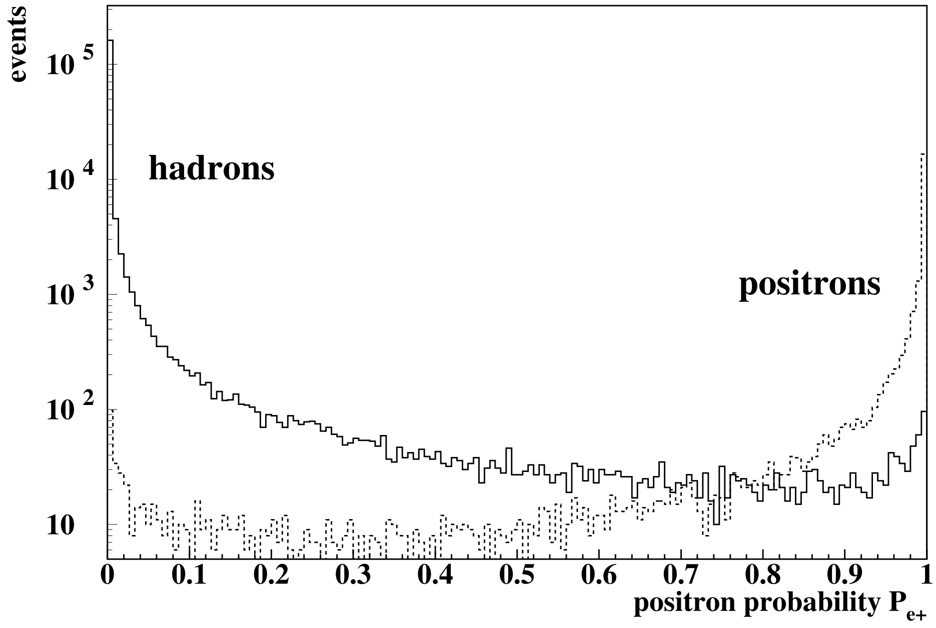

Figure 4.10: Result of the probability analysis: the positron probability P_{e^+} given by the TRD likelihood method for runs 4216-4240. For the distinction of hadrons (solid line) and positrons (dashed line) see tab.4.2.

For a better comparison with other quantities, Γ'_{TRD} and Γ_{TRD} are defined as follows:

$$\Gamma'_{TRD} = \log_{10} \frac{P'_{e^+}}{P'_h} \qquad \text{and} \qquad \Gamma_{TRD} = \log_{10} \frac{P_{e^+}}{P_h} = \Gamma'_{TRD} - \log_{10} \Phi(p, \Theta)$$

Γ'_{TRD} and Γ_{TRD} are so-called *logarithmic likelihoods*. A comparison between the logarithmic likelihood Γ_{TRD}, Γ'_{TRD} and the truncated mean is shown in fig.4.11. The pion rejection factor (PRF) has been calculated for a data set of 25 runs using the truncated mean, the whole probability analysis (Γ_{TRD}), and the probability analysis with $\Phi \equiv 1$ (Γ'_{TRD}) (tab.4.4). The PRF computed with Γ_{TRD} gives an impression of the performance of the TRD, while Γ'_{TRD} is the new contribution of the TRD to an overall HERMES PID.

[2]Mainly because of a tracking mis-alignment, there are a few tracks which do not give a response in any of the TRD modules. Therefore, these tracks (0.6%) are taken out in case of a detector performance study, such as here.

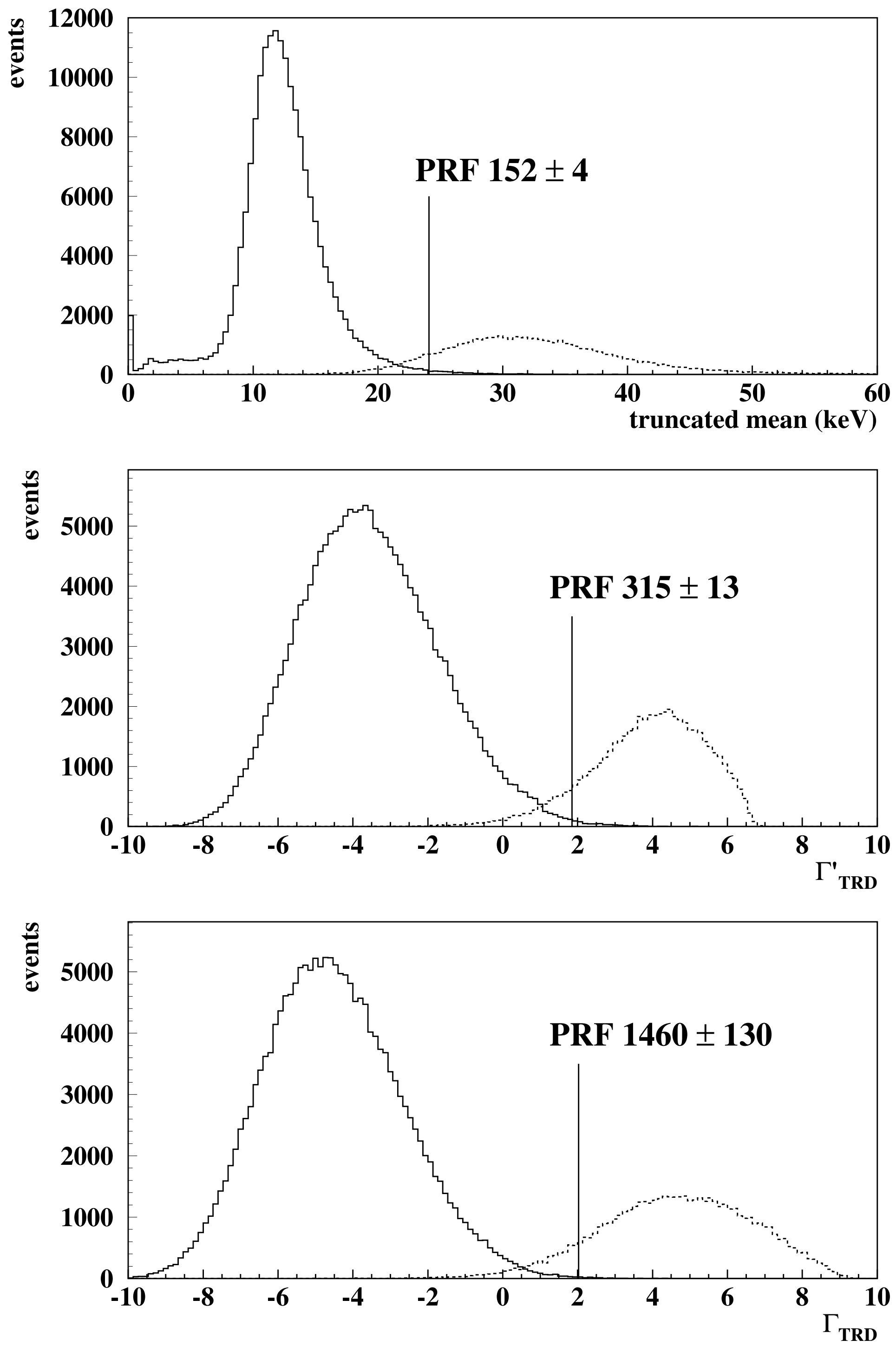

Figure 4.11: Truncated mean and logarithmic likelihoods (Γ'_{TRD} and Γ_{TRD}) for runs 4216-4240. For the separation of hadrons (solid line) and positrons (dashed line) see tab.4.2. The cut for 90% positron efficiency for the calculation of the PRF is indicated by a vertical line.

Additionally, the whole set of values were produced for six and less modules to see the possible consequences of removing one or more TRD modules (e.g for a larger ring imaging Čerenkov detector that would replace the threshold counter).

modules (eff.)	PRF with Γ_{TRD}	PRF with Γ'_{TRD}	PRF with tmean
6 (95%)	489 $\pm$ 25	122 $\pm$ 3	85 $\pm$ 2
6 (90%)	1462 $\pm$ 131	315 $\pm$ 13	152 $\pm$ 4
5 (90%)	731 $\pm$ 47	132 $\pm$ 4	89 $\pm$ 2
4 (90%)	311 $\pm$ 13	54 $\pm$ 1	48 $\pm$ 1
3 (90%)	110 $\pm$ 3	21 $\pm$ 0.2	21 $\pm$ 0.2

Table 4.4: Pion Rejection Factors for six or less modules with different methods with 95%/90% positron efficiency (runs 4216-4240).

The better pion rejection of the likelihood method can be explained by the better use of the information available. Six modules are used instead of five as in the calculation of the truncated mean value. Also the quantity Γ'_{TRD} accounts for zero module responses (inefficiencies) where the truncated mean mis-identifies particles as hadrons by including a zero into the averaging.

The above 1995 analysis was realized by a small package of FORTRAN programs and PAW scripts that handled the data ntuples (fig.3.12, bottom). The main subroutine that calculates Γ'_{TRD} was translated into C [32] and implemented into the g1DST/smDST production for 1996. All analyses from 1996 on use Γ'_{TRD} instead of the truncated mean to identify particles with the TRD. For 1996 the parent distributions are calculated by a new program that uses special DSTs as input (pidDSTs).

4.4.2 (New) PID Quantities at HERMES

A probability analysis was also made for the Čerenkov counter, the preshower detector, and the calorimeter (by the responsible groups). The results are the corresponding logarithmic likelihoods given by the conditional probabilities:

$$\text{Čerenkov}: \quad \Gamma'_{Cer} = \log_{10}\frac{P'_{e\ Cer}}{P'_{h\ Cer}} \quad , \qquad \text{preshower}: \quad \Gamma'_{Pre} = \log_{10}\frac{P'_{e\ Pre}}{P'_{h\ Pre}} \quad ,$$

$$\text{and} \quad \text{calorimeter}: \quad \Gamma'_{Cal} = \log_{10}\frac{P'_{e\ Cal}}{P'_{h\ Cal}} \quad . \tag{4.17}$$

These logarithmic likelihoods are combined to a value known as PID3:

$$\text{PID3} = \Gamma'_{Cer} + \Gamma'_{Pre} + \Gamma'_{Cal} = \log_{10}\left(\frac{P'_{e\ Cer}P'_{e\ Pre}P'_{e\ Cal}}{P'_{h\ Cer}P'_{h\ Pre}P'_{h\ Cal}}\right) \quad . \tag{4.18}$$

The old scheme, used in 1995, combined PID3 with the TRD truncated mean by a linear combination. This linear combination is known as *valley projection* or *valley cut* and minimizes the number of particles around zero:

$$\mathrm{oldPID} = \mathrm{PID3} + 0.31 \cdot \mathrm{TRD}_{\mathrm{tmean}} - 5.48 \tag{4.19}$$

The quantity $\Gamma'_{\mathrm{HERMES}}$ (for the naming see sect.7.2 in the appendix) similar to PID3, but now including contributions from all four HERMES PID detectors, can be calculated employing the result of the TRD probability analysis:

$$\Gamma'_{\mathrm{HERMES}} = \Gamma'_{Cer} + \Gamma'_{Pre} + \Gamma'_{Cal} + \Gamma'_{TRD} = \log_{10}\left(\frac{P'_{e\ Cer}P'_{e\ Pre}P'_{e\ Cal}P'_{e\ TRD}}{P'_{h\ Cer}P'_{h\ Pre}P'_{h\ Cal}P'_{h\ TRD}}\right) \quad . \tag{4.20}$$

The new $\Gamma'_{\mathrm{HERMES}}$ has a pion rejection twice as high as the old scheme (at 90% positron efficiency) because the pion rejection of Γ'_{TRD} is roughly a factor two higher than the truncated mean value (see fig.4.11 and tab.4.4). A comparison between the old PID scheme and Γ'_{TRD} is shown in fig.4.12.

The quantity $\Gamma'_{\mathrm{HERMES}}$ can be used for a Bayesian iteration (similar to sect.4.3.1) to obtain the flux ratios for the whole PID detector setup. The difference between the measurement of positively and negatively charged particles was implicitly neglected up to now because the TRD parent distributions did not depend on the charge of the particle. Since the incident flux of particles differs for each charge, separate flux ratios for positive and negative particles are introduced by:

$$\Phi^{+}(p,\Theta) = \frac{\text{number of incident positive hadrons } (p,\Theta)}{\text{number of incident positrons } (p,\Theta)} \qquad \text{and} \tag{4.21}$$

$$\Phi^{-}(p,\Theta) = \frac{\text{number of incident negative hadrons } (p,\Theta)}{\text{number of incident electrons } (p,\Theta)} \quad . \tag{4.22}$$

The flux Φ^{+} (Φ^{-}) is used for all positively (negatively) charged particles. This exploits all available information for an overall PID. The flux ratios $\Phi^{\pm}(p,\Theta)$ calculated by iteration are shown in fig.4.14 for a 95 data sample. The flux ratios have to be computed for each HERMES target type and trigger threshold since physics processes determine the ratio of hadrons to positrons.

The flux ratios $\Phi^{\pm}(p,\Theta)$ can be used to convert $\Gamma'_{\mathrm{HERMES}}$ into Γ_{HERMES}, the logarithmic likelihood corresponding to the real probabilities:

$$\begin{aligned}\Gamma_{\mathrm{HERMES}} &= \Gamma'_{\mathrm{HERMES}} - \log_{10}\Phi^{\pm} = \\ &= \log_{10}\left(\frac{P'_{e\ Cer}P'_{e\ Pre}P'_{e\ Cal}P'_{e\ TRD}}{\Phi^{\pm}P'_{h\ Cer}P'_{h\ Pre}P'_{h\ Cal}P'_{h\ TRD}}\right) = \log_{10}\frac{P_e}{P_h} \quad .\end{aligned} \tag{4.23}$$

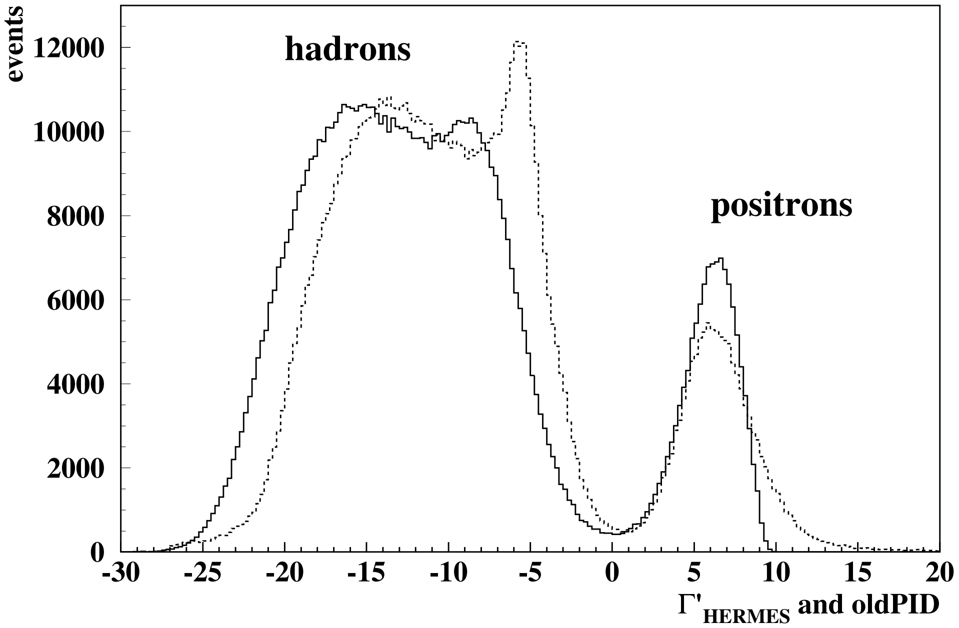

Figure 4.12: PID5 $\Gamma'_{\mathrm{HERMES}}$ (solid line) and the old PID scheme (dashed line) for good PID runs from 4611-5120 (multiplicity>1, caused by the limited database used.)

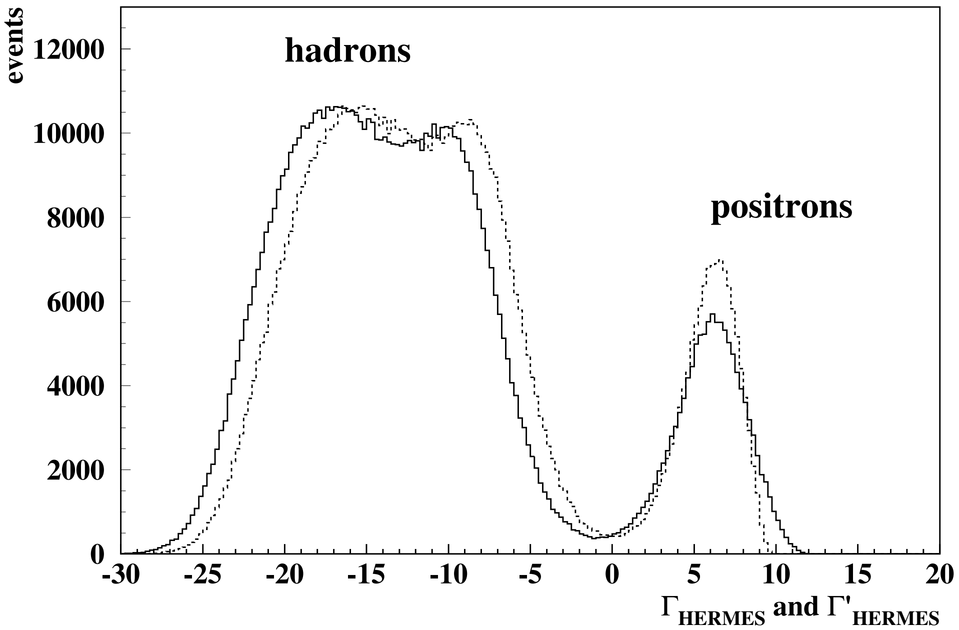

Figure 4.13: The overall PID value Γ_{HERMES} (solid line) in comparison with $\Gamma'_{\mathrm{HERMES}}$ (dashed line) for good PID runs from 4611-5120 (1995 data) (multiplicity>1).

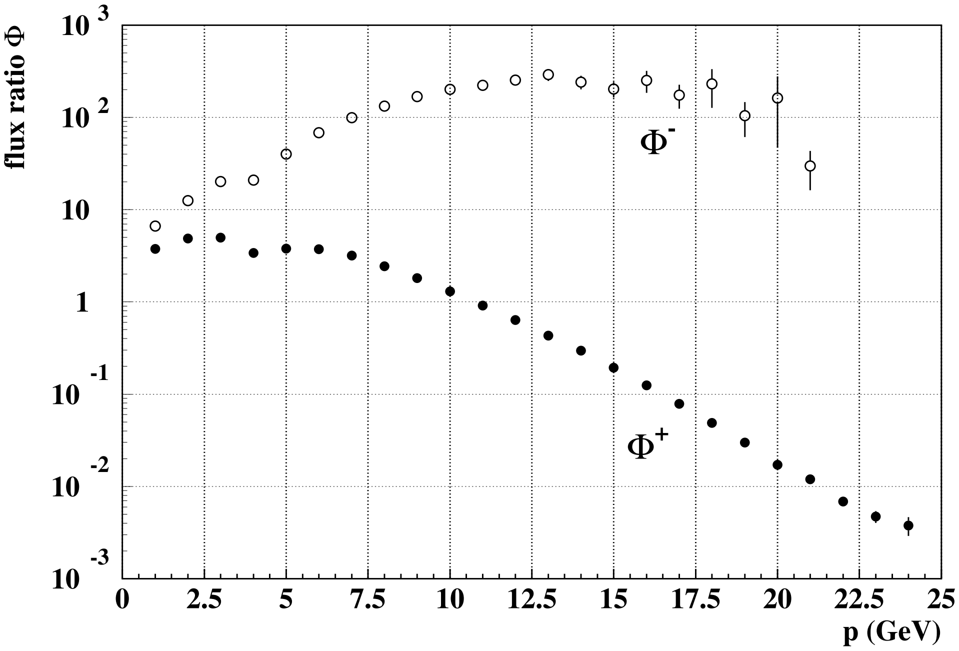

Figure 4.14: The flux ratios Φ^+ (solid circles) and Φ^- (empty circles) obtained by an Bayesian iteration using $\Gamma'_{\mathrm{HERMES}}$ and all good PID runs from 1995 (multiplicity>1 and $\Theta \in [40; 70\ \mathrm{mrad}]$).

The quantity Γ_{HERMES} shown in fig.4.13 has a two to three times higher pion rejection than $\Gamma'_{\mathrm{HERMES}}$ and a four to six times higher pion rejection than the old PID scheme (at 90% pos.eff.). Γ_{HERMES} has a straightforward interpretation: for example, a positron cut $\Gamma_{\mathrm{HERMES}} > 2$ selects all particles for which the probability to be an positron is more than 100 times larger than to be a positive hadron. However, an accurate Monte Carlo simulation is necessary to make definite statements about contaminations, efficiencies and rejection factors of the overall PID quantities $\Gamma'_{\mathrm{HERMES}}$ and Γ_{HERMES}.

It can be concluded that a detailed probability analysis of the TRD detector response and the use of flux ratios yield a more powerful PID at HERMES. The next step will be the implementation of flux ratios into the HERMES PID scheme.

5 Measurement of The Charged Pion Asymmetries

5.1 Data Selection

5.1.1 Data Quality

A clean and unbiased subset of the data is chosen for the analysis. Run-, burst-, and track-wise data quality cuts ensure a stable operating detector, good beam conditions, and high target performance. This section defines the 1996 criteria for *good data*. The detailed data quality applied to the 1995 data set can be found in references [33] and [34] , for example. From all 2132 polarized runs with good beam, target and detector conditions in 1995, 289 runs with at least one bad Čerenkov half (e.g.high voltage trip) have been rejected for this semi-inclusive analysis. This ensures a clean pion identification within the remaining 1843 runs. The run- and burst-criteria of the 1995 analysis are largely the same as for 1996 described below.

Two time periods have to be cut from the polarized running in 1996 for the following reasons: Fills 95-101 (417 runs) are rejected because the target surface was destroyed after the positron beam was dumped into the target cell. Fills 108-110 (173 runs) are excluded due to problems with the data acquisition. Unfortunately, these two reasons reject about 21% of the original data set. The remaining 2784 runs undergo the burst-wise data quality selection.

The burst-quality used is stored in so-called *bad-bit-files* that contain bit-patterns for each existing burst [35] . The bad-bit-files are a summary of the data-quality contributions of the different detector groups. Each bit corresponds to a malfunction of a detector component. The resulting burst selection used is summarized in tab.5.1. The criteria ensure high beam and target polarization to limit the uncertainty in the weighting of the asymmetries. The livetime of the DAQ has to be above 80% to avoid large dead-time corrections. In addition, the first and last bursts of a run are discarded because of DAQ overhead. Cuts on beam current and luminosity ensure stable running of the accelerator.

Another check is done on the entries of the spectrometer, target, and polarimeter logbooks to exclude periods with operational problems. Furthermore, high voltage trip detection from the GMS (Gain Monitoring System) and offline analyses of the detectors (FCs, BCs, TRD, H0, H1, H2, calorimeter, and luminosity monitor) lead to the rejection of bursts. Data quality information for the Čerenkov was not available for the b3 data-version analyzed. The logbook and fig.7.1 suggest fairly stable operation of the Čerenkov counter in 1996. Data quality plots of the PID detectors that show stable operation for the data analyzed can be found in sect.7.3 of the appendix.

Table 5.1: The burst-wise data quality cuts applied in the 1996 semi-inclusive analysis. The bad TRD bursts are not rejected; they are handled by a special PID scheme (see sect.5.1.2).

test quantity	condition imposed	records	DIS events	fraction
raw target polarization, P_{Traw}	$0.8 < P_{T_{raw}} < 0.99$	37480	55271	6.3%
fitted beam polarization, P_{Bfit}	$0.3 < P_{B_{fit}} < 0.8$	4458	19998	2.3%
livetime of the DAQ, t_{DAQ}	$0.8 < t_{DAQ} \leq 1.0$	21442	23654	2.7%
burst length, l_{burst}	$0 < l_{burst} \leq 11\ s$	12	14	>0.1%
beam current, I_B	$8 < I_B < 50\ mA$	692	592	>0.1%
luminosity rate, r_{lumi}	$5 < r_{lumi} < 60\ s^{-1}$	5080	20332	2.3%

reason for removal	records	DIS events	fraction
logbook/VC plate in bottom acceptance	4718	18056	2.1%
beam polarimeter logbook	948	5573	0.6%
malfunction of a target component	5593	29409	3.4%
target gas other than ^{1}H	3148	15925	1.8%
measurement of the molecular fraction not available	2306	13195	1.5%
target spin is flipping	29188	16331	1.9%
first and wrongly numbered records of a run	4278	17217	2.0%
last and wrongly numbered records of a run	5021	18563	2.1%
slow control inf.could not be synchronized	34228	83140	9.5%
too many bad calorimeter blocks (one bad block in the bottom allowed in 1996)	3140	11957	1.4%
One or more bad paddles in H2 or one or more bad blocks in the lumi-monitor	3530	13692	1.6%
HV trip in one of the FCs or BCs	3140	11381	1.3%
bad top or bottom TRD lead to PID downshifting	(1998)	(8267)	(0.9%)
data-quality for Čerenkov was not avail.for b3	-	-	-

total data set	235816	877976	100.0%
fraction rejected	106103	305633	34.8%
remaining data set	**129713**	**572343**	**65.2%**

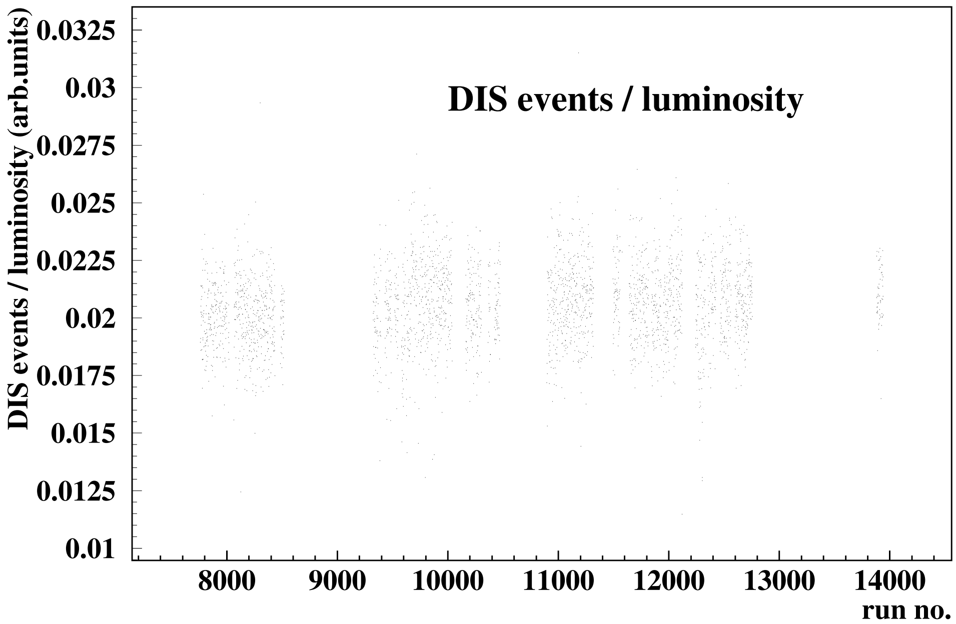

Figure 5.1: The ratio of DIS events to integrated luminosity versus all analyzed runs in 1996. (The luminosity is dead-time corrected, see sect.5.2.3.)

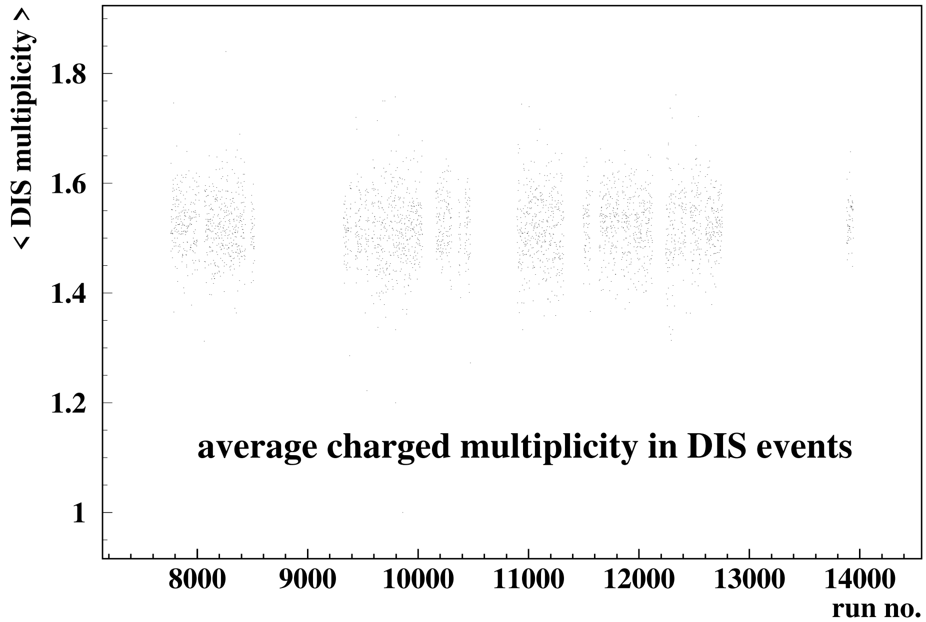

Figure 5.2: The average charged particle multiplicity in DIS events versus all analyzed runs in 1996. (The multiplicity includes the DIS positron.)

Table 5.2: Acceptance cuts applied to the tracks in the event data. Θ is the scattering angle and Φ the azimuthal angle of the tracks.

quantity	cut	reason
x-position at calorimeter	$\|x\| < 170$ cm	calorimeter measures
y-position at calorimeter	$\|y\| > 30$ cm	calorimeter measures
$\Theta_y = \tan^{-1}(\sin(\Phi)\tan(\Theta))$	$\|\Theta_y\| > 40$ mrad	shielding plate
vertex position 1995	$-20 < z_{vertex} < 20$ cm	tracks have to come
vertex position 1996	$-18 < z_{vertex} < 18$ cm	from the target gas
vertex distance from beam	$r_{vertex} < 7.5$ mm	stored in the cell

The two reasons which reduce the data sample the most are periods which cannot be synchronized to the slowcontrol information due to wrong and missing time information (9.5%) and data with low target polarization (6.3%). The applied data-quality cuts in tab.5.1 on the burst level remove about 35% of the data.

Two very important cross checks, the ratio of DIS events to luminosity, and the average DIS multiplicity are plotted versus time (runs) in figures 5.1 and 5.2. The graphs show stable reconstruction of DIS events during 1996 data taking period. All data quality criteria as explained for 1996 were applied for the 1995 analysis as well.

All tracks have to pass an acceptance check (tab.5.2). The cuts on the acceptance ensure that the tracks go through the entire spectrometer. The conditions on the vertex position cut out tracks that do not come from the target, such as particles from collimator scattering.

5.1.2 Kinematic Cuts and PID

Events that pass the data-quality conditions are scanned to determine whether they contain a DIS positron. At least one positron track (PID see below) with $Q^2 > 1$ GeV^2 and $W^2 > 10$ GeV^2 is required for an event to be labeled a DIS event. The Q^2-cut selects the DIS/scaling region while the condition W^2 cuts out hadronic resonances. In addition, a calorimeter signal larger than 3.5 GeV is forced for the DIS positron in 1996. This simulates the 1995 trigger in order to have the same kinematics for both years. The next step is to filter semi-inclusive events by requiring at least one identified hadron in coincidence with a DIS positron. Hadrons from the current region are selected by $z > 0.2$ and $x_F > 0.1$. Together with the W^2-cut, these cuts fulfill the Berger-criterion [10]. The z distributions of hadrons and pions are shown in fig.5.4. The thresholds of the Čerenkov counter act as effective momentum and z cuts for the pions. Since for HERMES kinematics $z \approx x_F$, a harder cut on z instead of x_F is preferred for two reasons: the fragmentation functions depend on z, and x_f has a larger uncertainty compared to z because it is calculated from six measured quantities. The resulting kinematic distribution of the positrons in semi-inclusive events as selected by the cuts discussed (tab.5.3) is shown

Table 5.3: The cuts and the x_{Bj} binning used in the analysis. The binning and the cuts are also indicated in fig.5.3.

$\Theta > 40$ mrad	acceptance
$(\Theta < 220$ mrad$)$	acceptance
$Q^2 > 1$ GeV^2	scaling region
$W^2 > 10$ GeV^2	no hadronic resonances
$z > 0.2$	current region
$x_F > 0.1$	current region

bin no.	x_{Bj} range
1	0.023 - 0.040
2	0.040 - 0.055
3	0.055 - 0.075
4	0.075 - 0.100
5	0.100 - 0.140
6	0.140 - 0.200
7	0.200 - 0.300
8	0.300 - 0.600

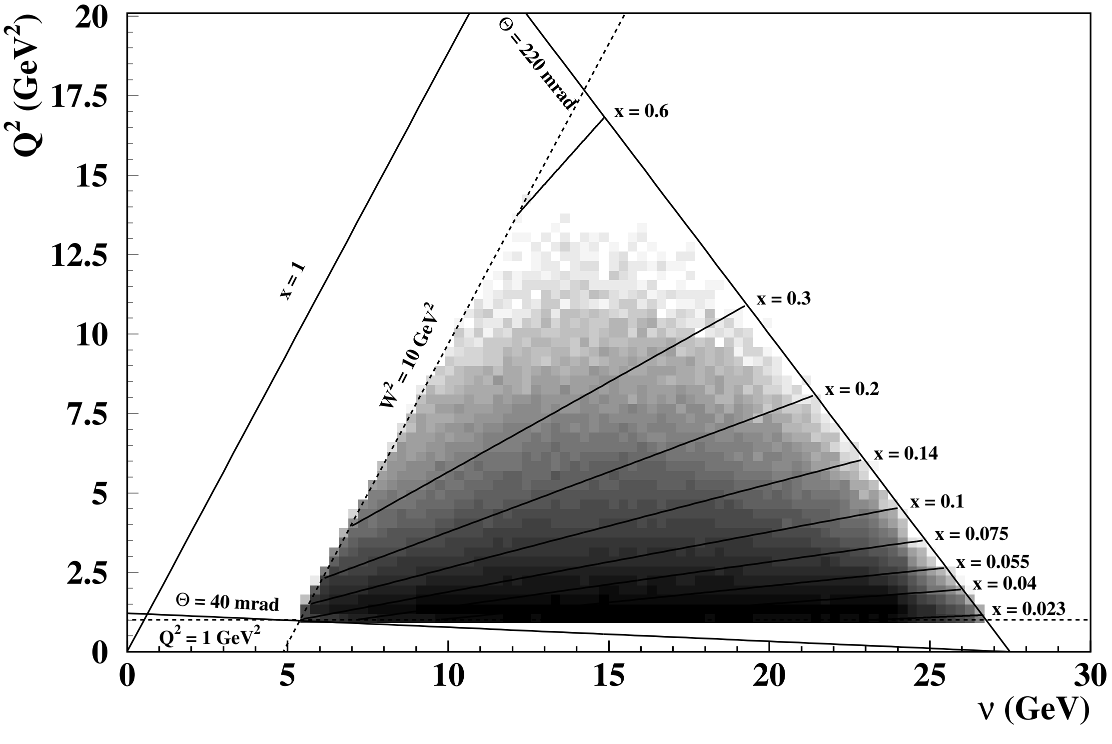

Figure 5.3: The kinematic plane of the HERMES experiment. Lines indicate the cuts and x-binning used in the analysis. The semi-inclusive event distribution of the positrons is plotted for 1995 data (using a logarithmic grey scale).

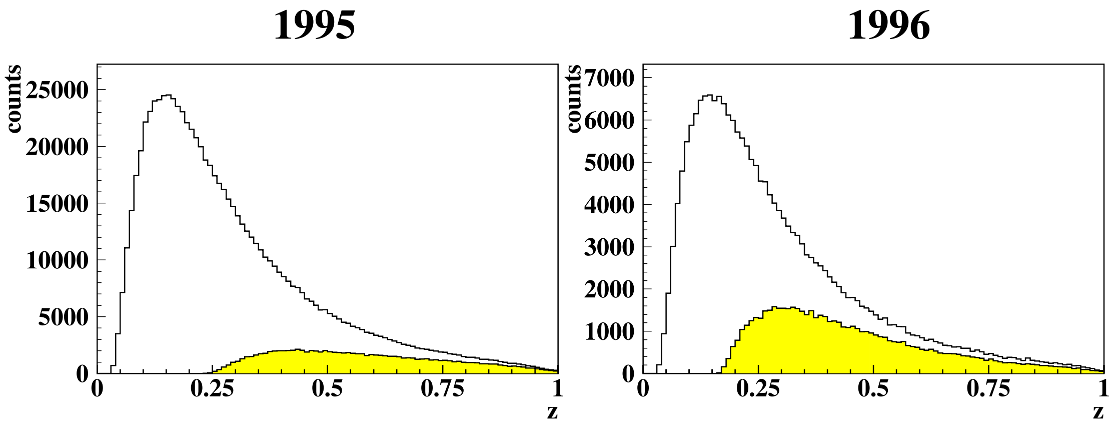

Figure 5.4: The z-distributions of hadrons (empty histogram) and the fraction of identified pions (grey area) in DIS events.

in fig.5.3. The HERMES acceptance allows to collect the majority of the events within the defined DIS region. The chosen x_{Bj}-binning is a compromise between statistics and x_{Bj}-resolution.

The separation of hadrons and positrons/electrons is achieved by cuts on the overall PID values oldPID (1995) and $\Gamma'_{\mathrm{HERMES}}$ (1996) (tab.5.4 and fig.5.5). These cuts ensure reasonably low contaminations at high efficiency (see sect.5.3.5). To enlarge the overall statistics, the PID3 value is used instead of the quantities $\Gamma'_{\mathrm{HERMES}}$ and oldPID when the TRD is not working (PID-downshifting). The PID-downshifting is applied on 6.4% of the events in 1995 and on 0.9% of the events in 1996.

A subset of identified pions is determined from the hadrons by requiring a Čerenkov signal for the track within the corresponding momentum range (tab.5.4). Figure 5.6 shows the kinematic distribution of hadrons and identified pions for 1995 and 1996. At HERMES energies the hadron sample is dominated by pions but not all of them can be identified with the threshold Čerenkov counter.

Table 5.4: PID cuts used for hadron (pion) and positron/electron identification. The PID quantities are defined in sect.4.4.2.

year	1995	1996
positrons/electrons	oldPID> 2.0	$\Gamma'_{\mathrm{HERMES}} > 1.5$
hadrons	oldPID< -1.0	$\Gamma'_{\mathrm{HERMES}} < -1.5$
additionally for pions	$6.0 < p < 20.0$ GeV Čer.: $N_e > 0.25$	$4.0 < p < 13.5$ GeV Čer.: $N_e > 0.25$

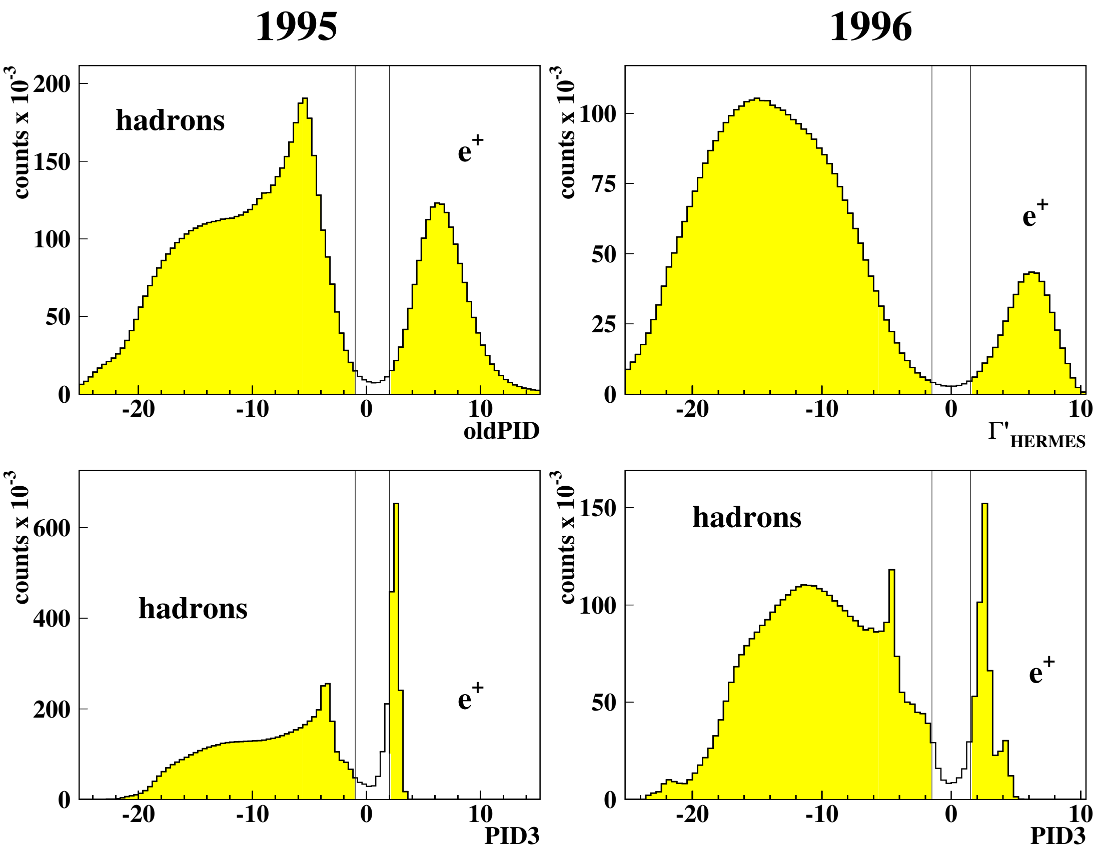

Figure 5.5: The PID schemes used for hadron and positron identification for 1995 and 1996. Top: All detectors. Bottom: PID downshifting used (PID3) in case of a bad the TRD. The cuts applied are indicated by vertical lines.

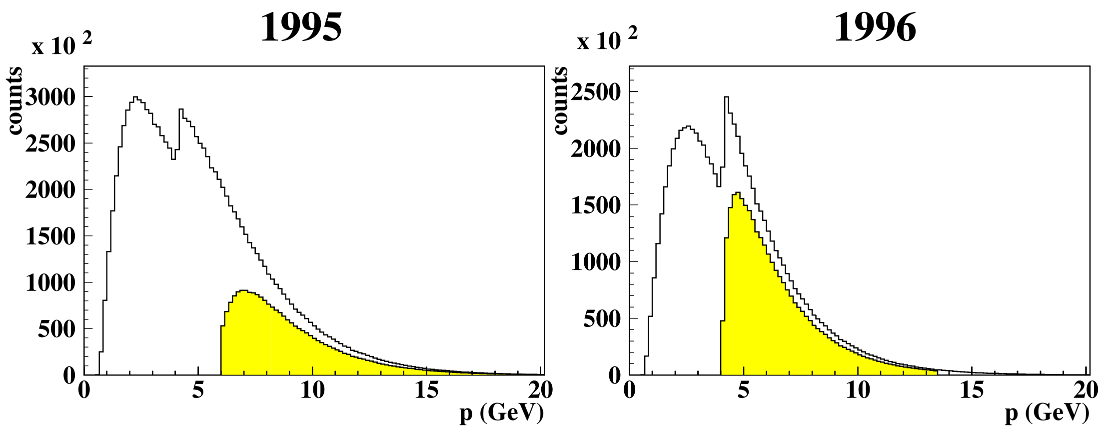

Figure 5.6: Kinematic distribution of all measured hadrons (empty histogram) with the fraction of all identified pions (grey area). The benefit of the lower Čerenkov threshold in 1996 is clearly visible as an increase in the pion identification efficiency. The marked decrease around 3.5 GeV is an effect of the calorimeter threshold.

5.2 The Extraction of the Spin Distribution Functions

5.2.1 Background Correction for Charge Symmetric Processes

For the following analysis, the DIS events as identified so far have to be corrected for charge symmetric background. Background events are processes where the identified DIS positron is not the one that scattered off the nucleon. An example is the decay of a π^0 to $\gamma\gamma \rightarrow \gamma\ e^+e^-$ (pair production in the detector material) in which the produced positron appears as a 'DIS' particle due to its kinematics.

The correction algorithm counts all 'DIS' electron events and subtracts them from the 'DIS' positron events. For example, if there are two potential 'DIS' positrons in an event, then the hadron is counted twice (with variables z, x_F, and x_{Bj} with respect to each positron); if a 'DIS' electron is measured, the hadron is subtracted from the overall statistics. This algorithm exploits the charge symmetry of the background. The sample left over accounts for the real number of semi-inclusive DIS events.

The distribution of all DIS and background events is shown for 1995 in fig.5.7. The actual correction turns out to be around 25% at $x_{Bj} \approx 0.023$ but it disappears with rising x_{Bj} and becomes negligible for $x_{Bj} > 0.04$. All spin-asymmetries of the analysis below are corrected as described.

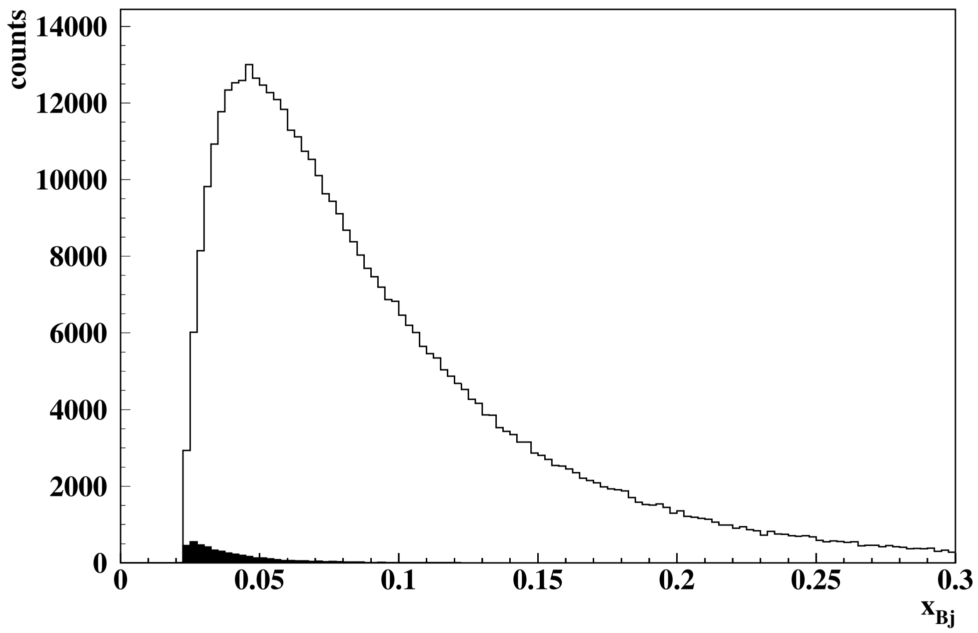

Figure 5.7: The x_{Bj} distribution of all events that appear to be semi-inclusive DIS (empty histogram) and the fraction that is charge symmetric background (black area) (1995 ^{3}He data). The background counts are subtracted from the total counts for the analysis.

5.2.2 Single Charge Asymmetries

The *single charge asymmetries* for hadrons and pions can be formed:

$$A^s_{h^\pm} = \frac{1}{<D>} \frac{n_+^{h^\pm} L_- - n_-^{h^\pm} L_+}{n_+^{h^\pm} L_{p-} + n_-^{h^\pm} L_{p+}} \quad , \tag{5.1}$$

with the definitions of sect.2.4.3 for L and L_p. The $n^{h^\pm}$ are the number of semi-inclusive hadron (pion) events for a single hadron charge. The h^+ and h^- semi-inclusive asymmetries should sum up to the *inclusive asymmetry*:

$$A_{incl} = \frac{1}{<D>} \frac{n_+^{e^+} L_- - n_-^{e^+} L_+}{n_+^{e^+} L_{p-} + n_-^{e^+} L_{p+}} \quad . \tag{5.2}$$

The inclusive asymmetry can be used to determine g_1. A cross-check between the single charge asymmetries and A_{incl} for the 1996 proton target is displayed in fig.5.8. The inclusive asymmetry was calculated using a $W^2 > 4\ GeV^2$ and a $y < 0.85$ cut. The y-cut rejects a region that would lead to large radiative corrections. The statistical consistency of $A^s_{h^+}$, $A^s_{h^-}$, $A^s_{\pi^+}$, and $A^s_{\pi^-}$ with the inclusive asymmetry indicates that the differences between the spin asymmetries are small. No systematic differences in the inclusive and semi-inclusive detection of events can be inferred.

The asymmetries $A^s_{h^+}$ and $A^s_{h^-}$ of the proton were also measured by SMC [36] . A comparison that shows that HERMES and SMC results are consistent for these asymmetries is shown in fig.5.9. The statistical significance of the HERMES data will increase substantially taking into account that twice the number of events from 1996 has been collected already during the 1997 run.

5.2.3 $\delta u_v(x)$ and $\delta d_v(x)$

The charge difference asymmetries $A_\pi^{^3\mathrm{He}}$ and A_π^p were calculated as described in sect.2.4.3 to determine the spin dependent valence quark distributions. The luminosity was rescaled to the data set employing a dead-time correction with the livetime of the DAQ and the length of each burst:

$$L(t) = \mathrm{lumirate(t) \cdot livetime(t) \cdot burstlength(t)} \quad . \tag{5.3}$$

The summation over all bursts gives the total luminosity:

$$L_{tot} = \sum_t^{\mathrm{bursts}} L(t) \quad . \tag{5.4}$$

The average product of target and beam polarization:

$$< \mathrm{P_B P_T} >= \frac{\sum_{\mathrm{t}}^{\mathrm{bursts}} \mathrm{P_B(t) P_T(t) L(t)}}{\mathrm{L_{tot}}} = \frac{\mathrm{L_P}}{\mathrm{L_{tot}}} \quad , \tag{5.5}$$

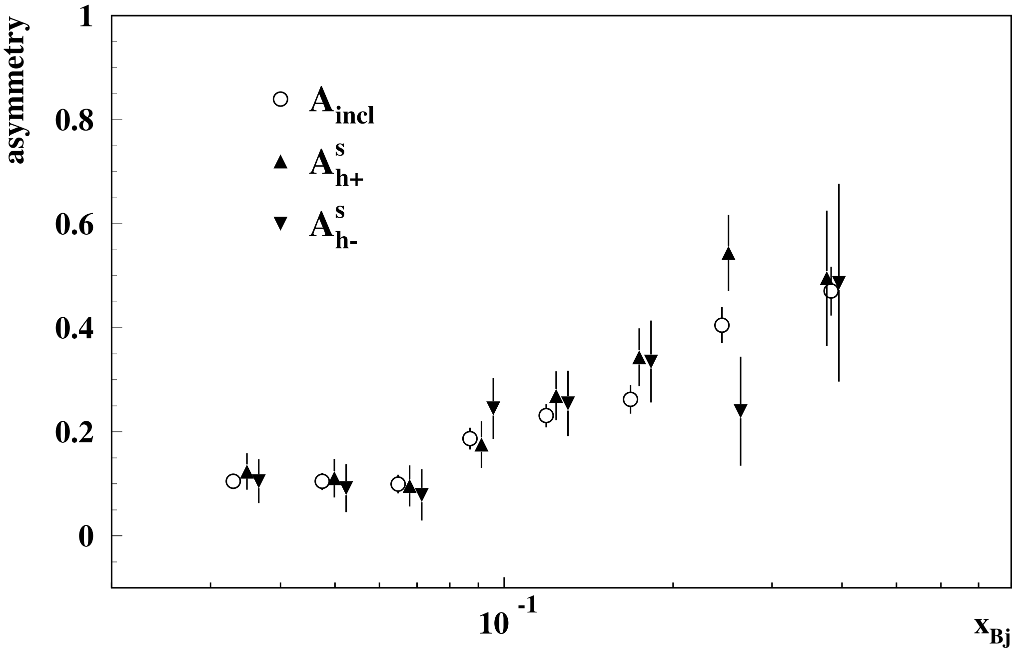

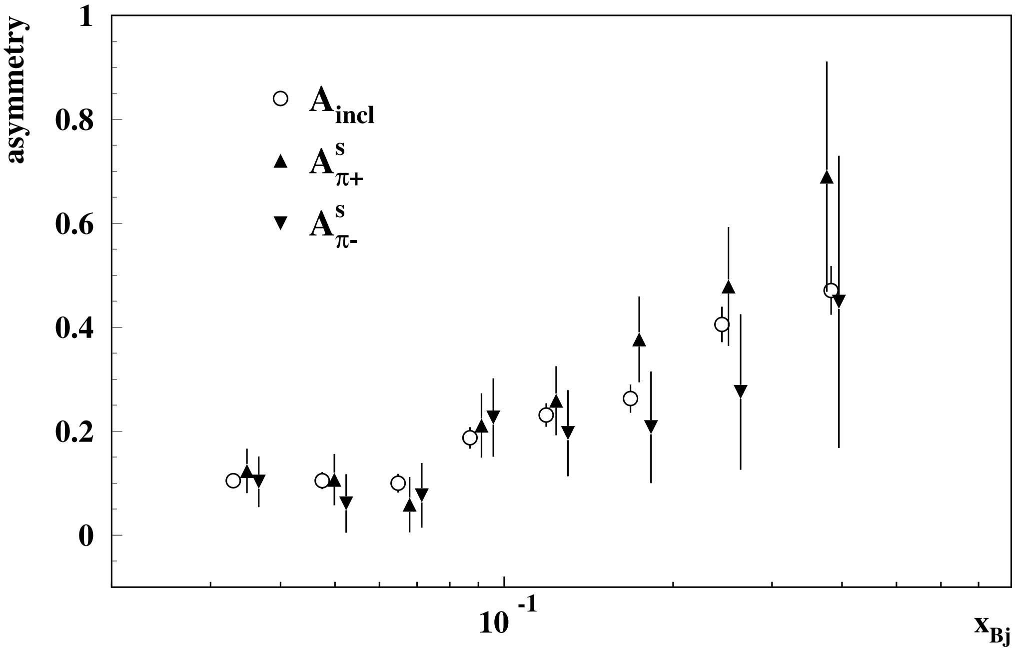

Figure 5.8: The single charge asymmetries on the proton (1996 data) for hadrons (top picture) and identified pions (bottom picture) in comparison with the inclusive asymmetry. The x_{Bj} values of the different data sets are intentionally shifted to allow a clear representation.

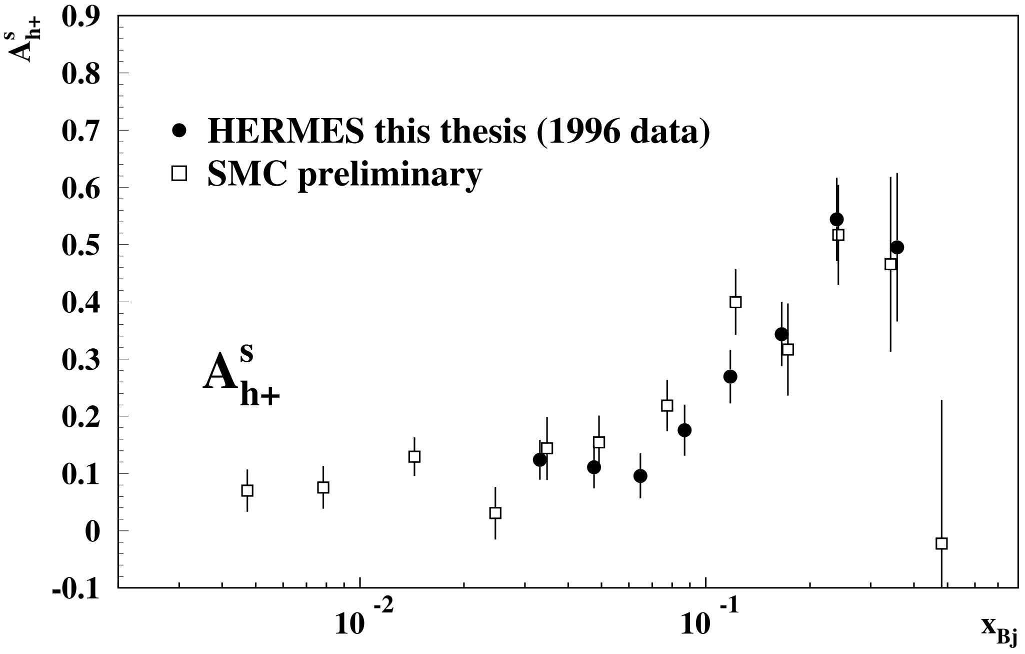

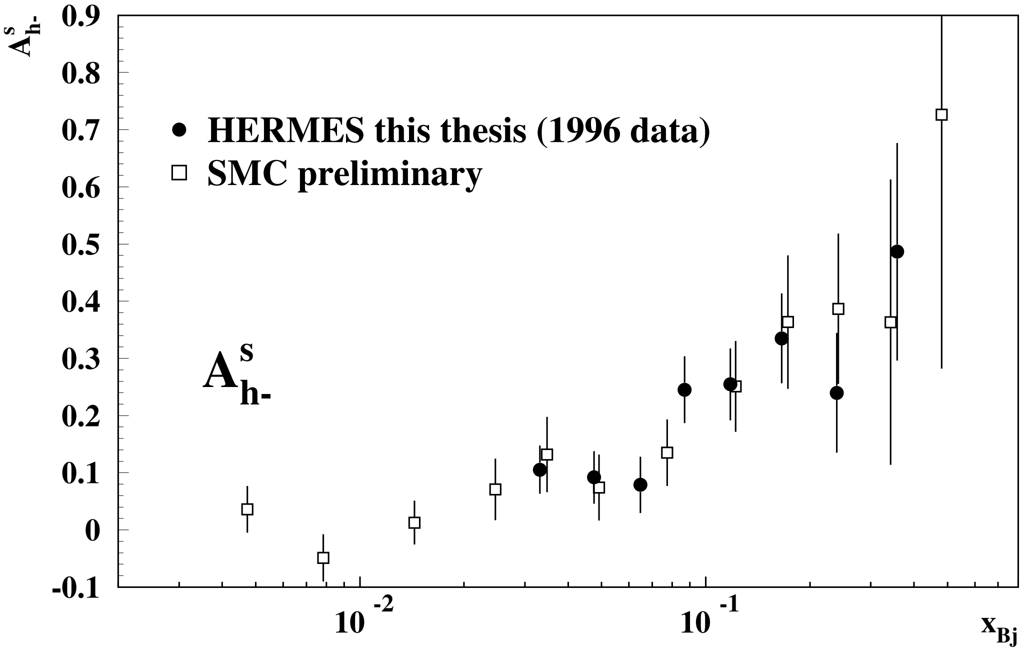

Figure 5.9: The HERMES single charge asymmetries for positive (top picture) and negative (bottom picture) hadrons in comparison with a preliminary SMC measurement [36]. Both data sets, HERMES and SMC, are consistent.

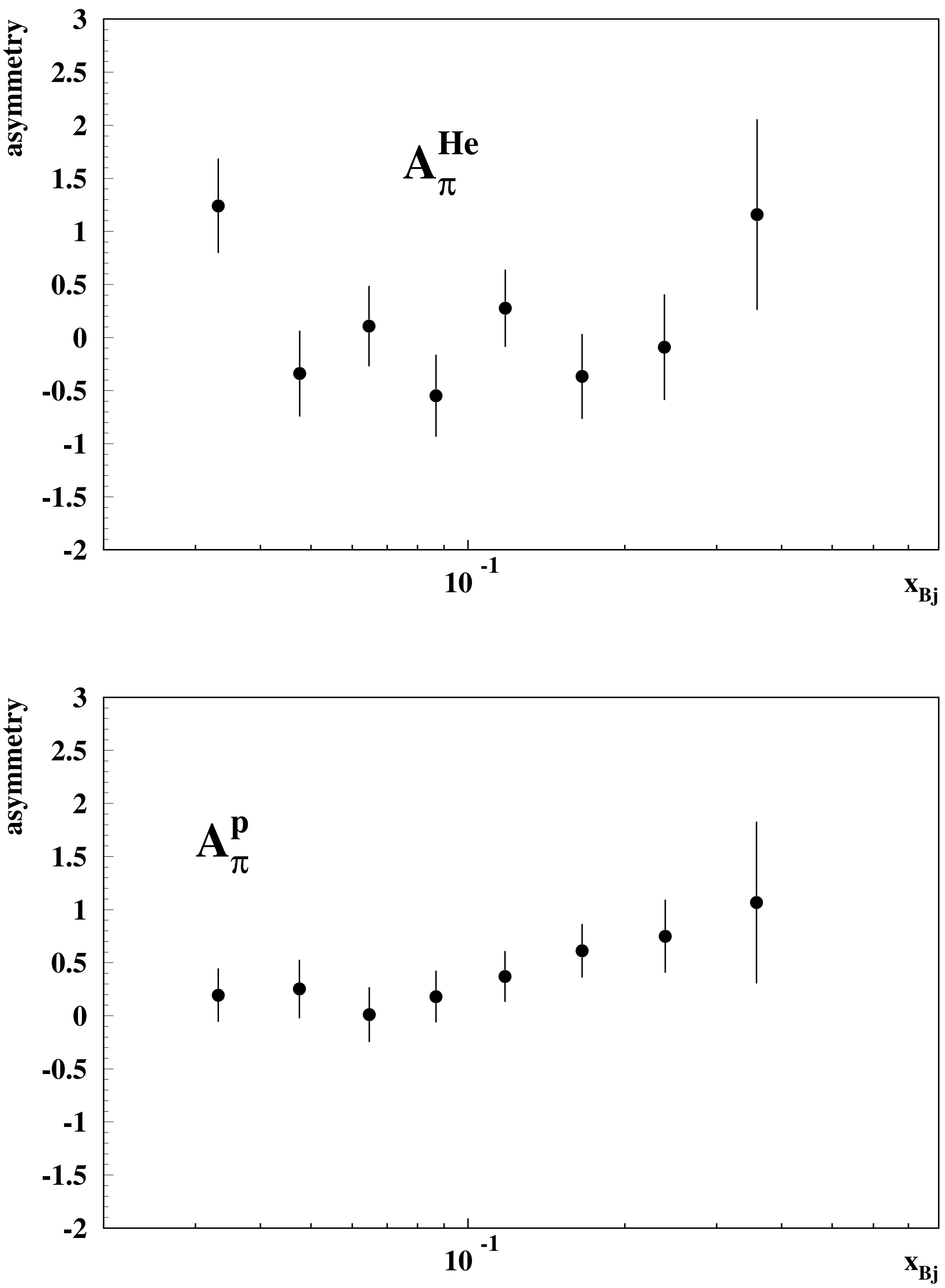

Figure 5.10: The charged pion difference asymmetries as determined from the HERMES 1995 helium (top picture) and 1996 hydrogen data (bottom picture).

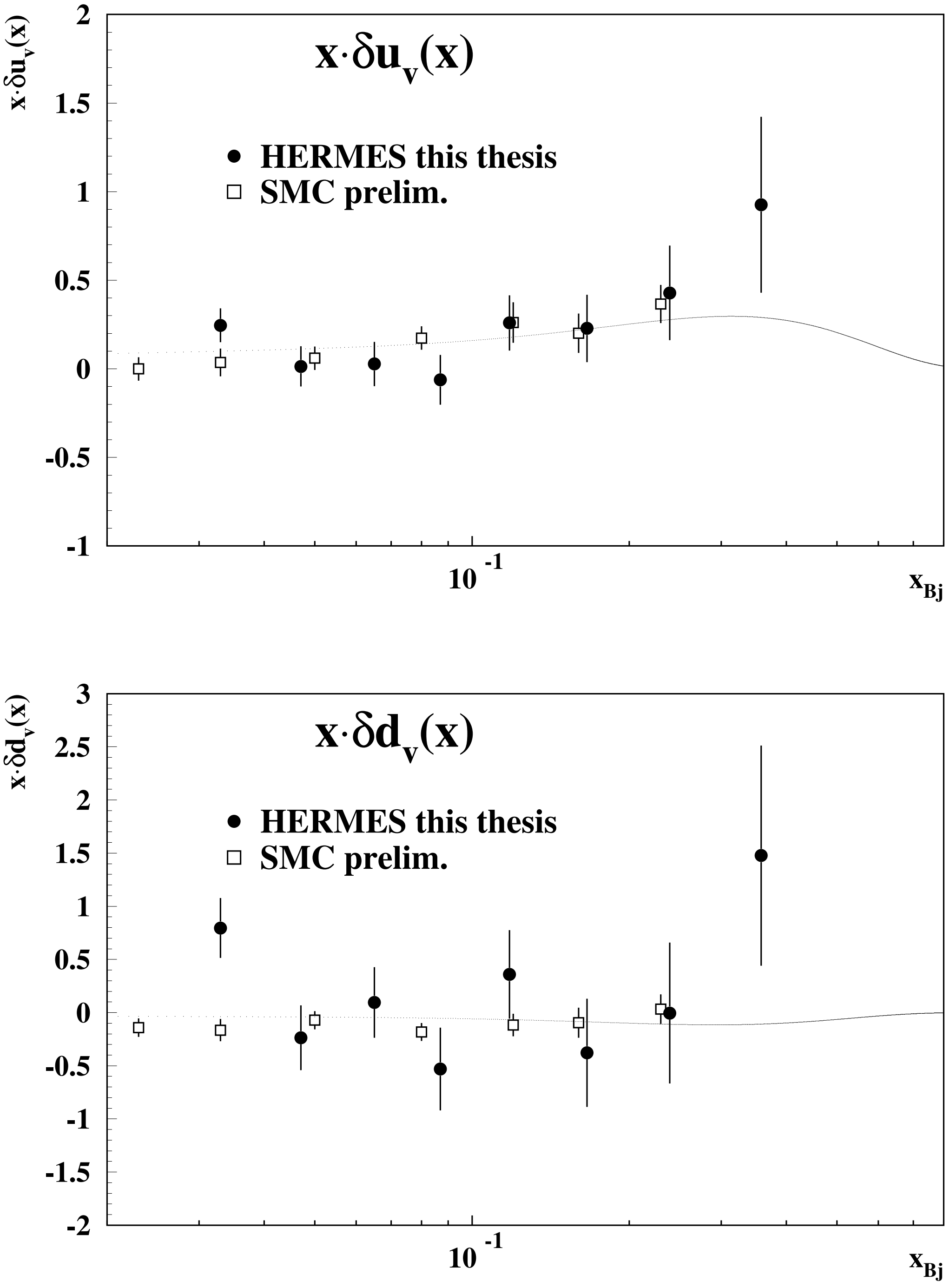

Figure 5.11: The valence quark distributions of the nucleon spin extracted using $A_\pi^{^3\mathrm{He}}$ and A_π^p with the simple Quark Parton Model. The lines show a parametrization from Gehrmann *et al.* [38].

is 25% for 1995 and 42% for 1996. (For the determination of the target polarization in 1996 see sect.5.3.4.)

Figure 5.10 shows the charge difference asymmetries from the helium and hydrogen data. The helium asymmetry $A_\pi^{^3\mathrm{He}}$ is corrected additionally for the effective neutron polarization due to S' and D states in ^{3}He :

$$A_\pi^{^3\mathrm{He}} = \frac{1}{< D > P_n} \frac{(n_+^{\pi^+} - n_+^{\pi^-})L_- - (n_-^{\pi^+} - n_-^{\pi^-})L_+}{(n_+^{\pi^+} - n_+^{\pi^-})L_{p-} + (n_-^{\pi^+} - n_-^{\pi^-})L_{p+}} \quad , \tag{5.6}$$

with the effective neutron polarization $P_n = 0.86 \pm 0.02$ [37] . Unfortunately the statistics collected in the 1995 HERMES commissioning year do not allow a non-zero measurement of $A_\pi^{^3\mathrm{He}}$.

The charge difference asymmetries are used for an extraction of $\delta u_v(x)$ and $\delta d_v(x)$ as outlined in sect.2.4.3 using the unpolarized distributions from a CTEQ parametrization [8] . The results are displayed in fig.5.11 and compared with a parametrization of Gehrmann *et al.* [38] . The extracted valence spin distributions are consistent with a SMC preliminary measurement which was done by using the hadron asymmetries in combination with fragmentation functions. Similar approaches at HERMES are under way.

HERMES is the first experiment that uses pion asymmetries to access the spin distributions of the nucleon. First results from pion asymmetries match to the world data and indicate the advantages of the HERMES semi-inclusive measurements since the results only represent a fraction of the anticipated HERMES statistics. The uncertainties of the results shown in fig.5.11 are dominated by the poor statistics from the 1995 HERMES commissioning year.

5.3 Systematic Studies

5.3.1 Acceptance

The measurement of the charge difference asymmetries relies on equal acceptance for positively and negatively charged hadrons (pions). The validity of this assumption is checked by the ratio of the charged hadron yields from DIS events for the left and right detector halves (fig.5.12). The acceptance is flat for the important momentum range above 4 GeV and the ratios for positive and negative hadrons agree. However, the relatively low statistics cannot exclude acceptance effects at an order of 2%. Below 3 GeV some particles are bent out of the acceptance by the magnet introducing an asymmetry in the acceptance.

Another implicit assumption made in the analysis concerns the momentum range in which the 1996 pion asymmetry is measured. On one hand a 6 GeV cut on the 1996 pions would be necessary in order to simulate the 1995 pion momentum range, on the other hand this should not matter because factorization is assumed. A test of the factorization assumption is shown in fig.5.13. It can be seen that the 1996 pion asymmetries as measured within

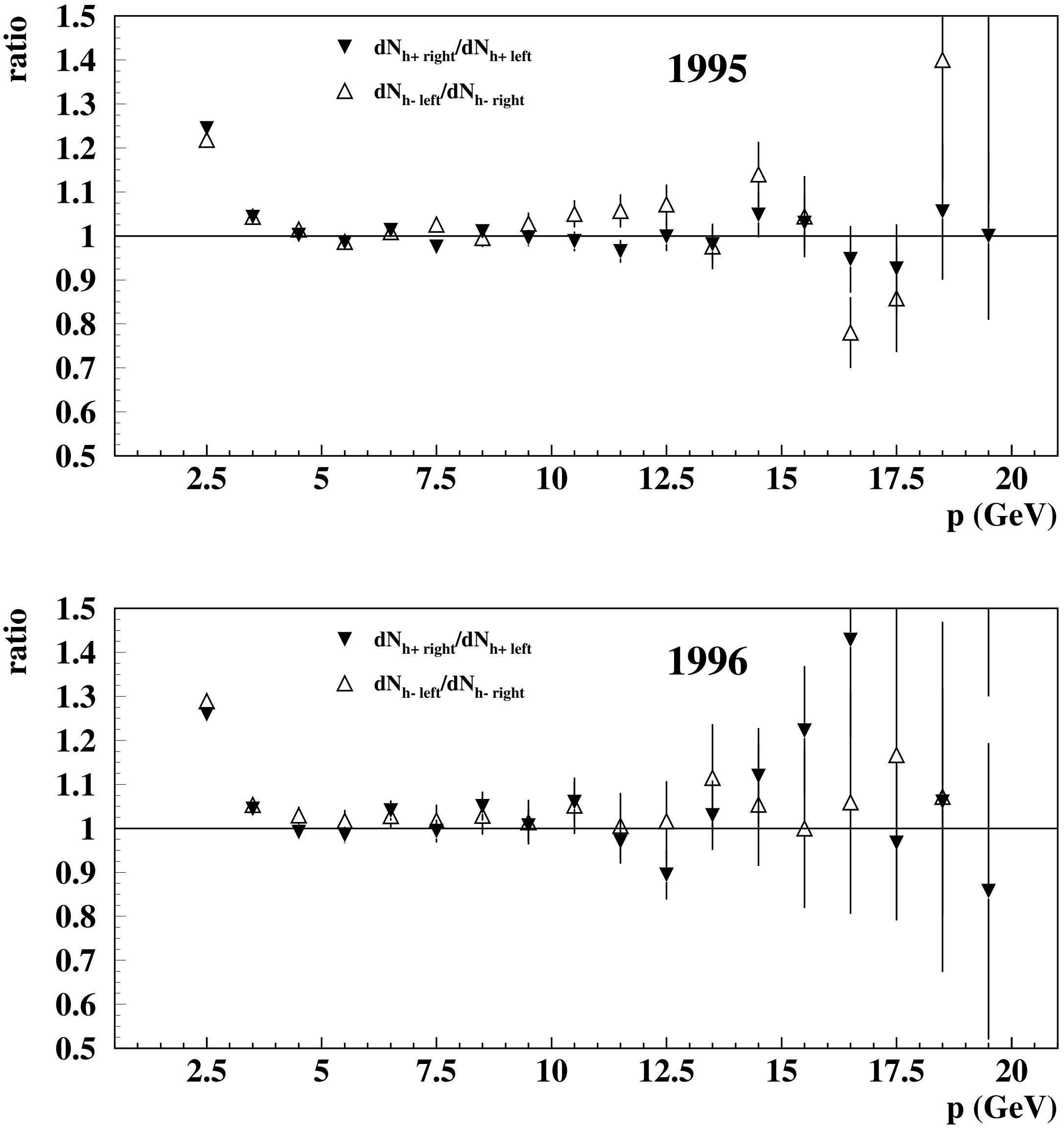

Figure 5.12: Ratios of charged (DIS) hadrons in the left and right detector halves (top: 1996, bottom:1996). The rise at low momenta comes from loss of particles that are bent out of the acceptance by the magnet.

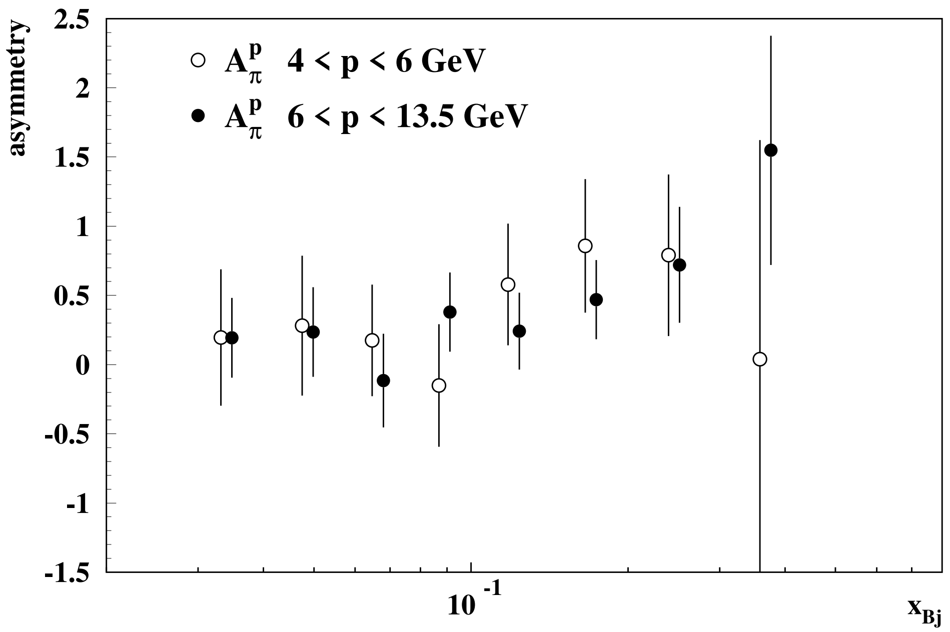

Figure 5.13: The asymmetry A^p_π measured in two different pion momentum ranges (1996). The two asymmetries agree on a confidence level of 94.6%. The x_{Bj} values of the second asymmetry are intentionally shifted to allow a clear representation.

the momentum ranges from 4 - 6 GeV and 6 - 13.5 GeV do not differ significantly. Thus, the entire pion data set from $4 - 13.5$ GeV can be used when combining with the helium data. No additional systematic uncertainty is assumed in this case.

5.3.2 Leading Particles and Rhos

This section deals with the question of whether the 'signal' in the charge difference asymmetries can be enhanced by counting only the *leading* hadrons in semi-inclusive events. The idea is that the hadron that carries the largest momentum (*the leading hadron*) should be correlated the most to the fragmentation of the struck quark. Hence, a measurement using leading particles only should increase the information in the asymmetry. Furthermore, two Monte Carlo Studies are made to investigate pions that come from ρ decays and the validity of flavour tagging by charge in this case.

Two schemes to define leading particles are introduced. The first scheme (*charge-leading*) labels a hadron/pion as leading if it has the largest momentum among the charged hadrons as detected in the spectrometer. The second scheme (*total-leading*) additionally rejects charged hadrons if a π^0 with larger momentum could be reconstructed from trackless calorimeter clusters. In this case the energy of the two clusters is assumed to be caused by the two γ's from a π^0 decay. Figure 5.14 shows the invariant mass of trackless calorimeter cluster pairs in 1996 with the cuts applied to define a π^0 in the total-leading scheme. Also single calorimeter clusters that have a higher energy than all of the hadrons lead to a rejection of charged particles.

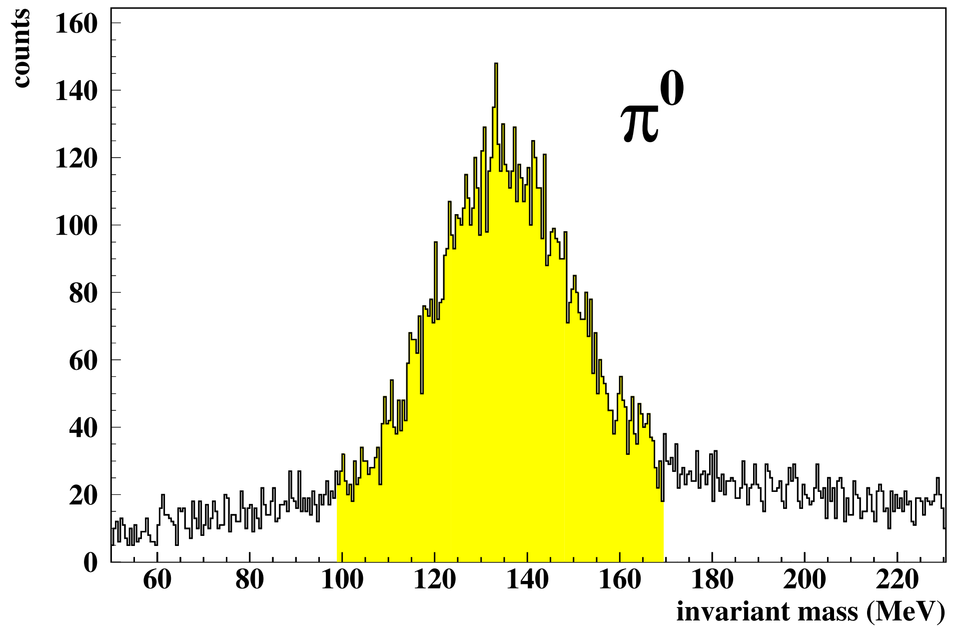

Figure 5.14: The invariant mass of trackless calorimeter cluster pairs for fill 115 (1996) and $p_{\pi^0} > 5\,\mathrm{GeV}$. The grey area is a symmetric window around the π^0 mass and defines the reconstructed π^0's used in the total-leading scheme.

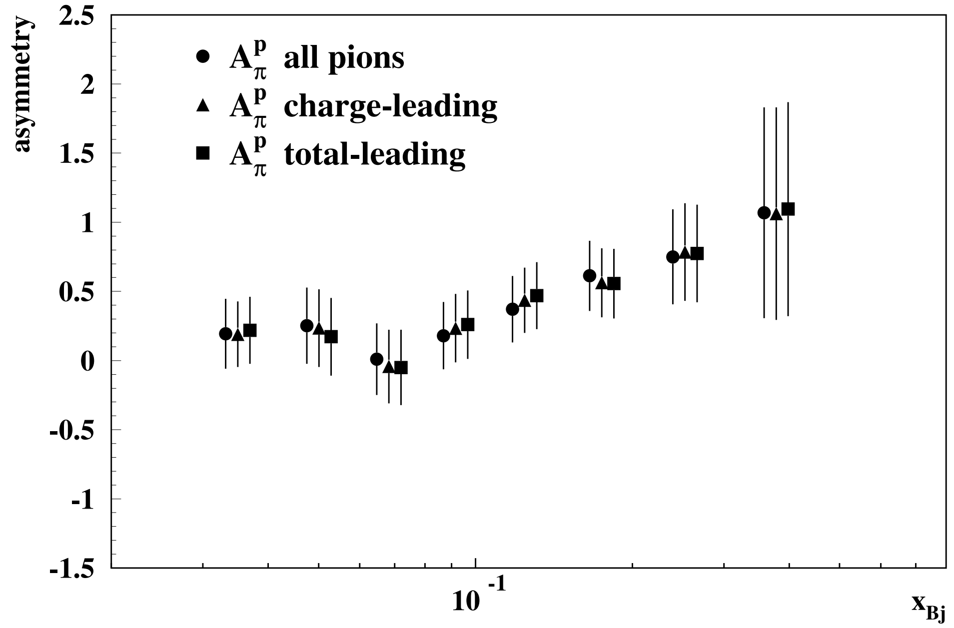

Figure 5.15: The pion asymmetry A^p_π of the proton formed using all pions, *charged-leading* pions, and *total-leading* pions (1996 data). The x_{Bj} values of the different asymmetries are intentionally shifted to allow a clear representation.

The three leading schemes including all particles, charge-leading, and total-leading are compared in fig.5.15. The limited statistics do not allow to make a statement about an enhancement of the signal. One reason lies in the observed average hadron multiplicity which is close to one for the HERMES acceptance. Most of the non-leading and low-z particles go down the beam pipe or are incident on the steel plate. Also, the low reconstruction efficiency ($\approx$ 20%) of π^0's reduces the impact the total-leading scheme could have. Therefore all coincident hadrons were used for the analysis for two reasons: the formalism as written down in sect.2.4.2 requires all pions due to the definition of the fragmentation functions, and the acceptance corrections necessary for the charge-leading, and total-leading scheme are highly complex and would rely on a Monte Carlo simulation of the fragmentation process.

Another question is whether the asymmetry analysis is biased by pions that come from decays of non-diffractive ρ's. This is investigated by employing the 1995 HERMES Monte Carlo (HMC). This simulation models all the HERMES detectors and generates deep inelastic events using the LUND model [39] . The following study assumes an ideal neutron target and the 1995 HERMES acceptance (with the proper Čerenkov threshold). Data from the smDSTs of the HMC84 Heidelberg production were used. The Monte Carlo simulation shows that the fraction of identified pions that do not come directly from the fragmentation dominate at lower z values (fig.5.16). These pions come from the decay of short-lived particles, predominantly from ρ's that originate in the fragmentation.

A separation of pions from ρ decays in the actual data is impossible for several reasons. The low multiplicity results in the detection of only one pion in most cases and does not allow the ρ mass to be reconstructed. In addition, the Monte Carlo simulation shows that pions from ρ's are indistinguishable kinematically from pions that come from the fragmentation directly. The total information about the reaction delivered by the spectrometer does not allow a separation. On the other hand, the contribution of pions coming from ρ^0 decays cancels in the ansatz used to extract the spin distribution. Furthermore, the formalism can be written down for pions from $\rho^{\pm}$'s introducing fragmentation functions that include decays from ρ's. This works if isospin-symmetry is valid for ρ-production in the fragmentation so that the number of independent fragmentation functions can be reduced in the same way as for pions only.

The only concern left is whether the measured pion still carries the 'leading' information. This is answered by fig.5.17 which shows that the fraction of pions that come neither from leading particles of the original reaction, nor directly from the fragmentation, is concentrated at lower z. It is assumed that the extraction of the spin distribution functions via all identified pions is valid since in the case of charged ρ's the charge of the pion is the same as the original ρ. Moreover, none of the studies indicate measured (z>0.2) hadrons coming from the target fragmentation region. The HERMES acceptance itself acts as an effective current-region filter.

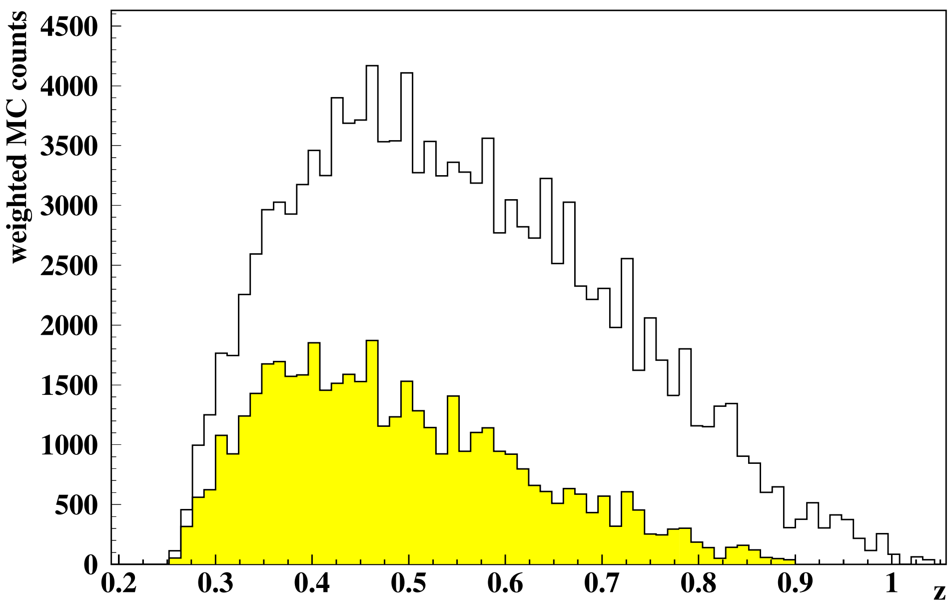

Figure 5.16: Hermes Monte Carlo: leading identified pions (empty histogram) and the fraction that comes from decays (grey area). More than 99% of the particles that do not come directly from the fragmentation come from ρ decays.

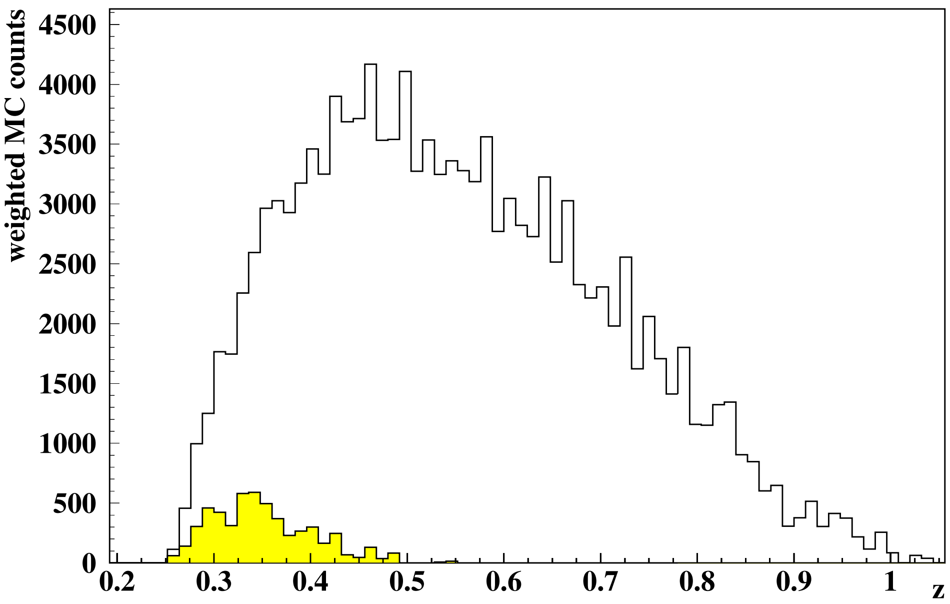

Figure 5.17: Hermes Monte Carlo: the empty histogram shows charged-leading pions. The grey area is the fraction that neither is leading in the original reaction nor comes from a decay of a particle that was leading in the original reaction.

5.3.3 Yield Stability

One difficulty a high energy experiment has to cope with is keeping the experimental conditions stable over the long time period during which the data are collected. Time dependent studies are performed to ensure stable conditions and disclose possible undiscovered problems. The behaviour of the DIS yield versus time (fig.5.1) is the most important example. Although major changes (i.e.new calorimeter threshold) occurred during the 1996 data taking, the DIS yield is constant over time (simulated 3.5 GeV threshold in 1996). Another systematic test is to plot the measured asymmetry versus time and assure that the seen fluctuations are statistical only. This was done for 1995 and 1996 for all x-bins. An example is shown in fig.5.18.

There are two reasonable ways to calculate the actual asymmetry: collect all events for the year and form the asymmetry or calculate A_π fillwise and then average over the fills. The latter is motivated by the idea that most of the systematics remain constant over the time of a fill. Both methods give consistent answers (fig.5.19). For the higher x-bins the statistics within a fill become very low ($<$ 10 events per spin state). In this case the uncertainties have to be treated binomially (not Gaussian) and the result becomes more sensitive to statistical fluctuations. The more stable behaviour at high x_{Bj} and the proven stable running lead to the choice of the scheme that integrates over the entire running period.

5.3.4 Normalization of the Hydrogen Data

The target polarization for 1996 is calculated by:

$$P_T = P_{BRP}\ \alpha_0\ [\ \alpha_r + \ (1-\alpha_r)\ \beta\ ] \qquad \text{with} \qquad \beta = 0.5\ , \tag{5.7}$$

where the raw polarization P_{BRP} of the hydrogen atoms is measured by the BRP. Here α_0 is the atomic fraction of the injected gas, and α_r is the fraction of the atoms that *does not* recombine to molecules within the cell. The quantities P_{BRP}, α_0, and α_r are measured to an absolute precision of $\pm\,0.01$ [40].

The unknown parameter β is defined as the nuclear polarization of H_2 molecules which recombined from polarized atoms. From the analyzed data set a systematic uncertainty of 6.4% can be inferred covering all possible β-values ($0 < \beta < 1$). Measurements to determine β and reduce this systematic uncertainty were done in 1997.

The largest systematic uncertainty arises from the unknown spatial distribution of the recombination process in the storage cell. The measurement of α_r represents only the recombined gas fraction near the exit of the sampling tube. Therefore, a sampling correction for α_r is necessary. Depending on the assumption this leads to different non-uniform distributions of the polarization over the cell. This and the question of the influence of a non-uniform target cell surface (caused by beam dumps) lead to a systematic uncertainty of 20% of the total polarization. The current studies of the processes in the target are expected to reduce this uncertainty significantly.

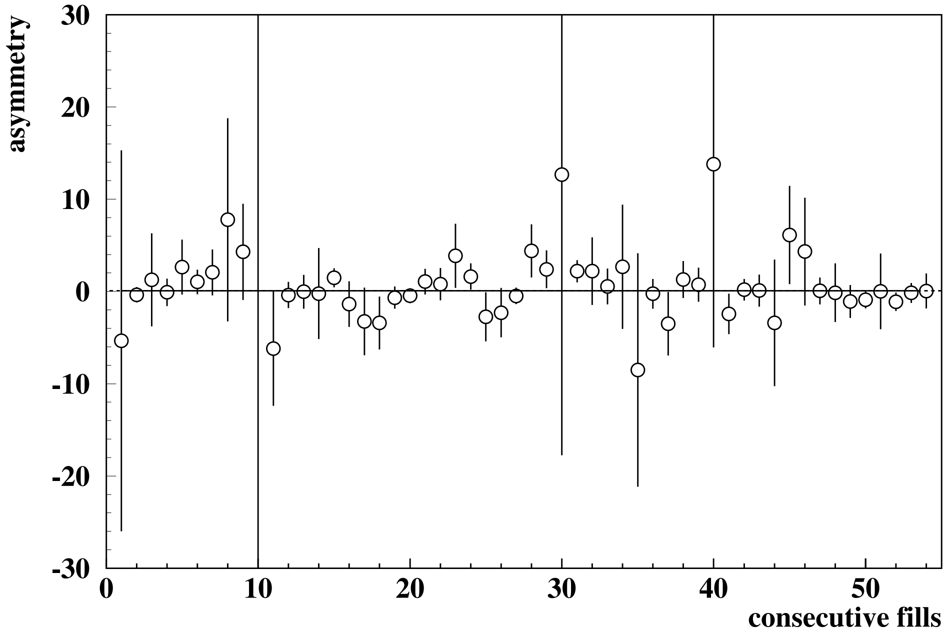

Figure 5.18: The asymmetry A_π^p for the first x-bin versus fill (consecutively numbered). A fit with a constant gives $A_\pi^p(< x_{Bj} >= 0.033) = 0.063 \pm 0.236$ with a reduced χ_n^2 of 0.62 .

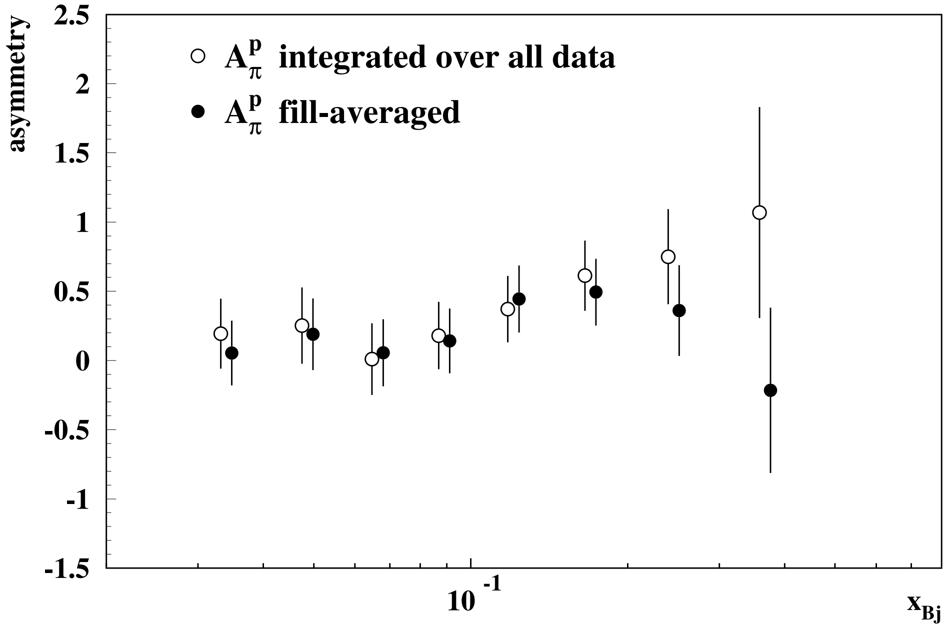

Figure 5.19: The asymmetry A_π^p obtained by integration over all data and by averaging over a fill-wise calculation. The uncertainties are calculated assuming Gaussian statistics. The x_{Bj} values of the second asymmetry are intentionally shifted to allow a clear representation.

5.3.5 Influence of the Particle Identification

The HERMES Monte Carlo simulation (HMC) models the physics processes and most parts of the detector with high accuracy. However, the simulation does not yet reproduce all PID detector responses at a level that would allow to make statements about efficiencies and contaminations achieved using the second level PID (likelihood algorithms). Therefore, this paragraph will give an estimate on particle mis-identification (for the 1995 data set) using a simple model.

The estimate of contaminations and efficiencies for the PID cuts used in the semi-inclusive analysis is done in two steps. First the hadron contamination of the DIS positrons is estimated. Then the lepton contamination of the hadrons is computed. Finally, the hadron contamination of the DIS positrons and the lepton contamination of the hadrons are summed to an overall contamination for semi-inclusive hadrons.

First, positively charged particles that pass all DIS and acceptance cuts and have a hadron (oldPID<-1) in coincidence are considered. Figure 5.20 (top) shows the oldPID-values in this case. The DIS positrons are separated by a cut in the particle spectrum. The model assumption is that the tails in the spectrum can be approximated by an exponential (this is more pessimistic than a Gaussian assumption). A sum of two exponentials is fit to the valley (fig.5.20 bottom/left) to estimate the positron efficiency and the remaining hadron contamination. With the help of this fit the particles are divided into positrons and hadrons. The contamination values obtained for two cut positions (0 and 2) are shown in fig.5.20 (bottom/right). The next step is to plot oldPID for particles that appear in coincidence with 'a well identified DIS positron (PID>2)' (fig.5.21 top). The small peak at oldPID≈5 comes from positrons/electrons that originate in charge symmetric processes. The positron/electron contamination of the h^+/h^- sample can be estimated to be $< 0.1\%$ (for PID<-1).

DIS positron and hadron values are then combined to overall contaminations and efficiencies (fig.5.21 bottom). The contamination of the hadron sample due to PID only is below 0.18% on average and below 0.35% in the worst x-bin. The average overall hadron efficiency is well above 98.5% (>97% in the lowest x-bin). This study was also done for h^+,h^-,π^+ and π^- separately and gave the same results within the statistical uncertainties. Similar studies for the PID used in 1996 were performed. It can be concluded that the influence of the contamination from particle mis-identification on the hadron asymmetries is almost negligible. But because of the model-dependence of the derivations above and the determined contamination values, a maximum systematic uncertainty of 0.5% is assigned to the asymmetry measurement. The definite statement about the overall performance of the PID can only be made by a Monte Carlo simulation that is detailed enough to describe the tails of the PID responses perfectly. Efforts to achieve this precision are under way.

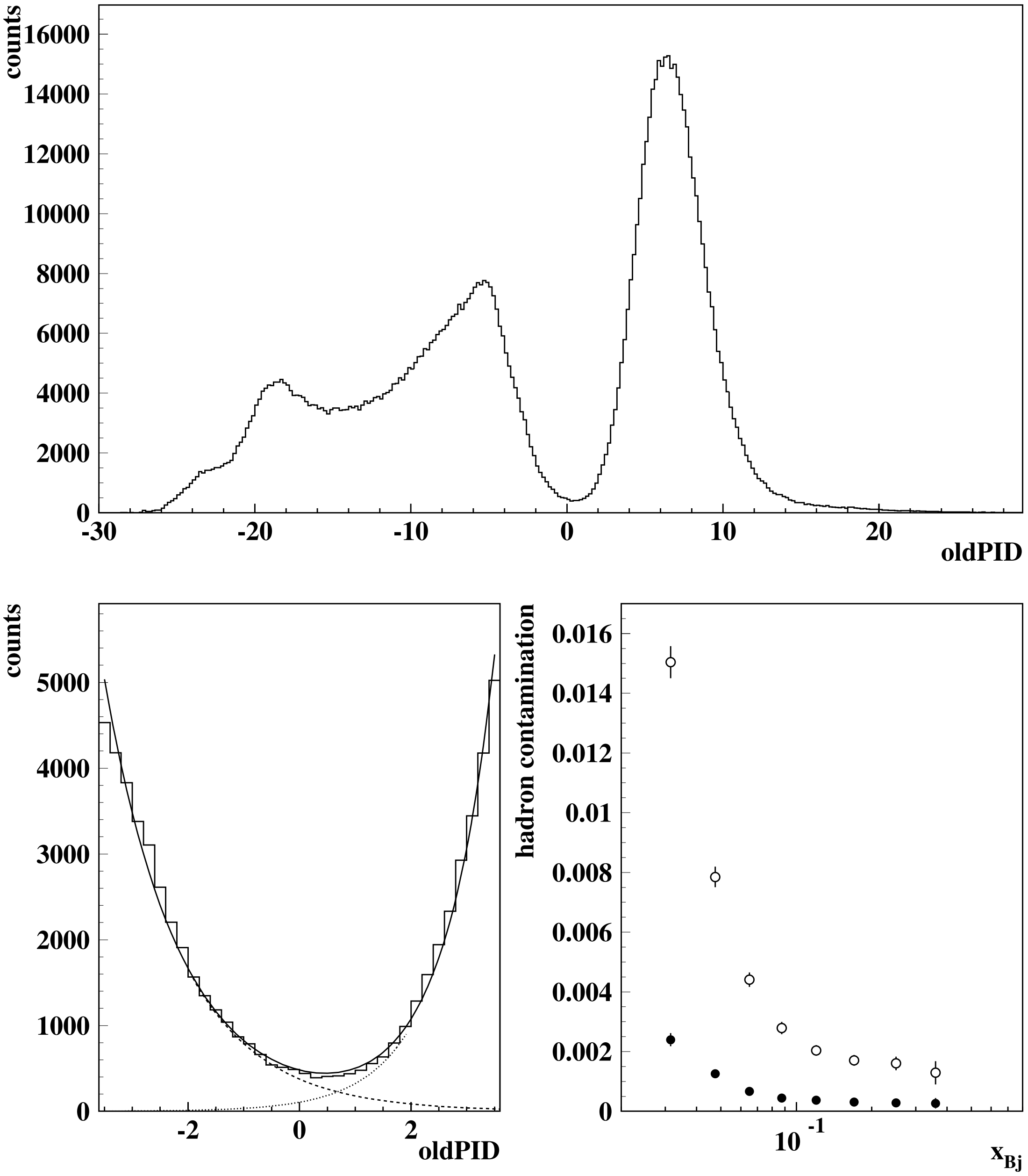

Figure 5.20: Top: oldPID (1995) of positively charged particles that pass all DIS and acceptance cuts and have a hadron (oldPID<-1) in coincidence. Bottom/left: fit of the sum of two exponentials to the 'PID-valley'. Bottom/right: hadron contamination of the DIS positron sample for a cut at oldPID>0 (open circles) and oldPID>2 (solid circles) vs. x_{Bj}.

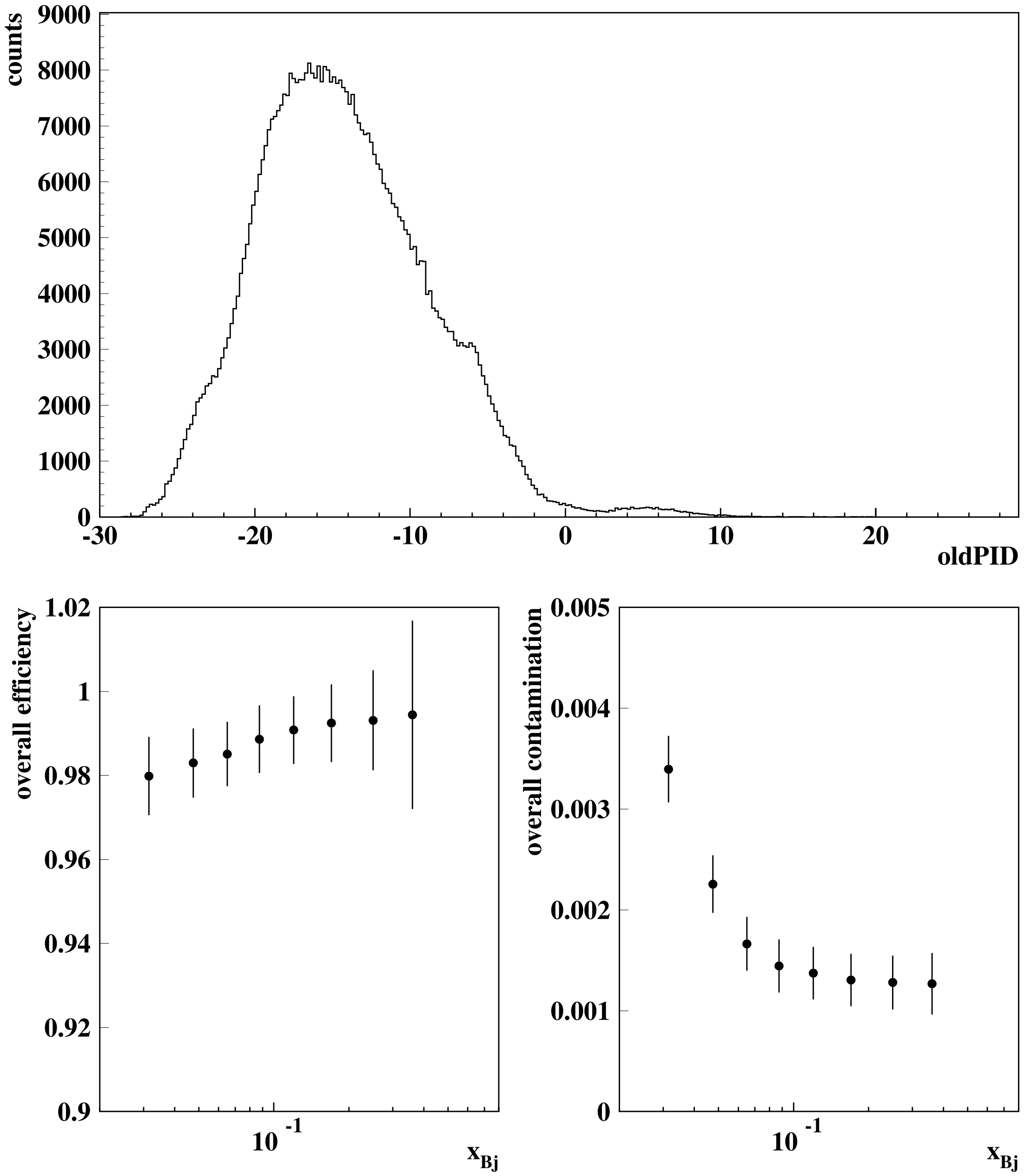

Figure 5.21: Top: oldPID of the particles that come in coincidence with 'a well identified DIS positron (oldPID>2)'. The small peak at oldPID>0 comes from e^+e^- pairs (e.g. produced by γ's from π^0 decays). Bottom: overall hadron efficiency and contamination vs. x_{Bj} for the cuts oldPID>2 (DIS positrons) and oldPID<-1 (hadrons).

5.3.6 Conclusion

A summary of the systematic uncertainties is given in tab.5.5. The uncertainty on the beam polarization measurement in 1996 (4.1%) is calculated for the good data set analyzed [41] . For 1996 the overall systematic uncertainty is expected to become smaller since many studies are not complete yet. The beam and target polarization uncertainties differ from the other systematics because they only change the overall normalization of the spin-asymmetries, not their shape. The uncertainty of the parametrization of the unpolarized quark distribution is of the order of 3%. Despite all the systematic effects, the results on $\delta u_v(x)$ and $\delta d_v(x)$ are still dominated by statistics, especially by the 1995 data set.

Table 5.5: Summary of the systematics uncertainties of the 1995 and 1996 semi-inclusive measurements of A_π.

reason	1995	1996
beam polarization	5.4%	4.1%
target polarization	5.0%	$\approx$ 20%
nuclear corrections	2%	-
$\pi^+ - \pi^-$ acceptance	2%	2%
particle identification	$<$ 0.5%	$<$ 0.5%
overall systematic uncertainty on A_π	7.9%	$\approx$ 20%
$u_v(x)$, $d_v(x)$ parametrization		$\approx$ 3%
systematic uncertainty on $\delta u_v(x)$		$\approx$ 20%
systematic uncertainty on $\delta d_v(x)$		$\approx$ 10%

6 Conclusion and Outlook

The HERMES experiment accumulated 2.2×10^6 good DIS events on a polarized ^{3}He (1995, commissioning year) and 5.7×10^5 good DIS events on a polarized proton target (1996). Efficient particle identification using a threshold Čerenkov counter, a preshower detector, a transition radiation detector, and a calorimeter, enables semi-inclusive measurements with low contaminations due to particle mis-identification. The HERMES TRD with its large active area contributes significantly to the positron/hadron separation. The separation was improved employing a Bayesian probability analysis of the detector response.

Within the simple Quark Parton Model the measured semi-inclusive pion charge difference asymmetries were used to extract the valence quark spin-distributions of the nucleon. The uncertainty of the result is dominated by the statistics of the data set, especially from 1995. The isospin and charge conjugation invariance of the fragmentation functions is still to be proven. Over 2×10^6 good DIS events on the proton have already been collected including the 1997 run. The anticipated number of good DIS events on a deuteron target (1998/99) is estimated to be another 2×10^6 events. Assuming 50% beam and 90% target polarization, the statistical precision on $\delta u_v(x)$ and $\delta d_v(x)$ can be calculated. The anticipated statistical uncertainties using the simple Quark Parton Model (eq.2.36 and eq.2.39) and eq.7.2 (with $n_+ \approx n_-$) are shown in fig.6.1. The semi-inclusive yields were estimated from the 1996 data set using a 2 GeV cut for identified pions corresponding to the proposed effective momentum range of the HERMES Ring Imaging Čerenkov (RICH) detector.

In future, the HERMES RICH detector will provide pion and kaon identification. Therefore, fragmentation functions for each hadron type will be measured as well as kaon spin asymmetries which contain direct information about the strange sea polarization. Additional muon identification will allow the reconstruction of J/Ψ's and hence a measurement of the gluon polarization via photon-gluon fusion. Also reconstructed D's could give a measurement of ΔG.

The valence quark spin-distributions can be measured by approaches other than the one presented which uses the pion asymmetries directly. Iterative fitting of all spin-asymmetries employing a detailed Monte Carlo simulation of the fragmentation process or the unfolding of the hadron asymmetries using fragmentation functions as measured by HERMES are anticipated to give significantly smaller uncertainties than the prediction shown in fig.6.1. Moreover, these methods will give measurements of the polarization of the quark sea. Including the reduction of systematics, HERMES will make a precise measurement of the spin structure of the nucleon.

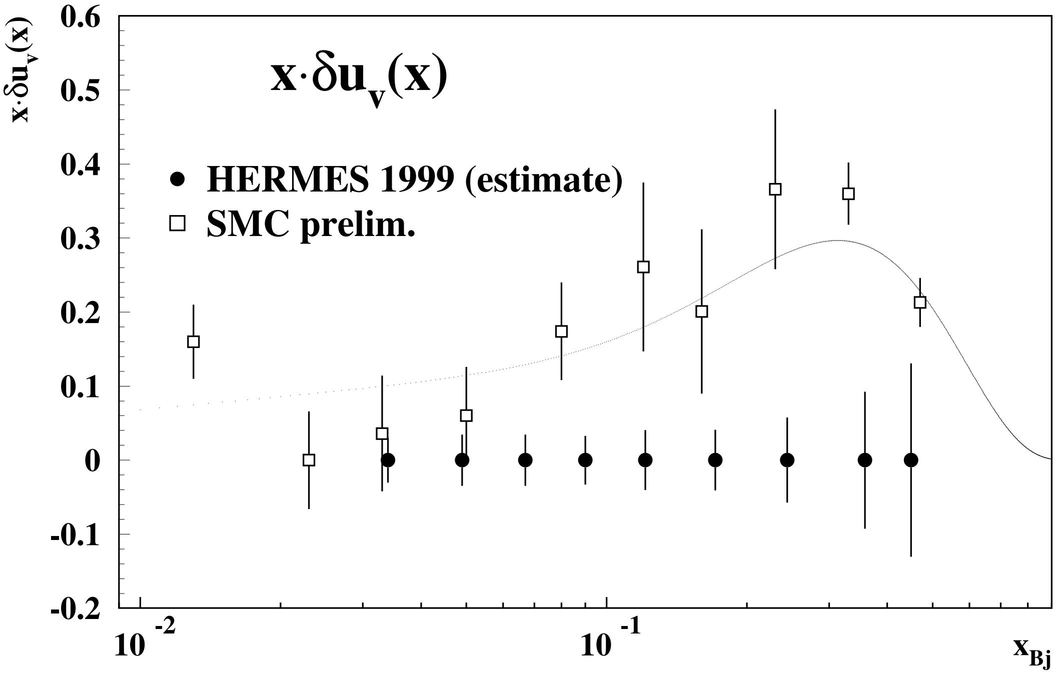

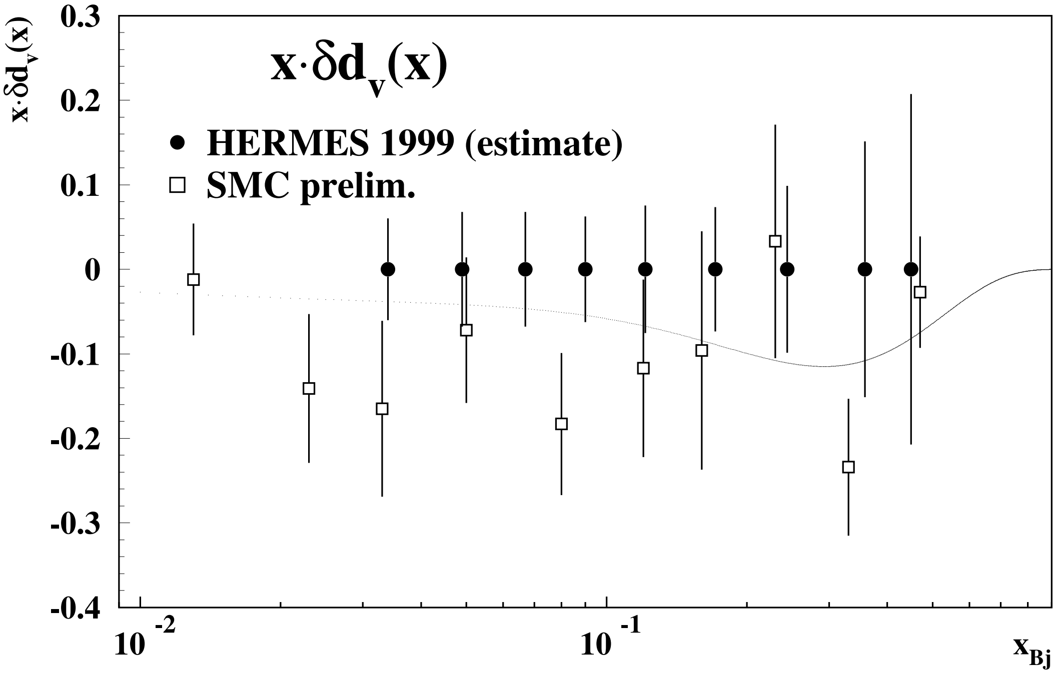

Figure 6.1: Estimated uncertainties for 2×10^6 DIS events on the proton and deuterium each employing pion charge difference asymmetries and the simple Quark Parton Model.

7 Appendix

7.1 Formulas for Uncertainties

7.1.1 Pion Asymmetry: ΔA_π

Assuming enough statistics for a Gaussian calculation, the uncertainty on the measured pion asymmetry A_π is:

$$
\begin{aligned}
\Delta A_\pi = & \frac{1}{<D>}\frac{1}{(n_+^{\pi^+}-n_+^{\pi^-})L_{p-}+(n_-^{\pi^+}-n_-^{\pi^-})L_{p+}} \cdot \\
& \Big[n_+^{\pi^+}(L_- - <D> L_{p-}A_\pi)^2 + n_-^{\pi^+}(L_+ + <D> L_{p+}A_\pi)^2 + \\
& n_+^{\pi^-}(L_- - <D> L_{p-}A_\pi)^2 + n_-^{\pi^-}(L_+ + <D> L_{p+}A_\pi)^2 \Big]^{\frac{1}{2}} \quad ,
\end{aligned}
\tag{7.1}
$$

where $n_\pm^{\pi^\pm}$ are the number of counts for each spin state of the target with the corresponding luminosities $L_\pm$ ($L_{p\pm}$). $<D>$ is the average depolarization factor for each x_{Bj}-bin. In the case of a small asymmetry, equal luminosities, and 100% polarization for both target spin states the uncertainty on the pion asymmetry can be simplified to:

$$
\Delta A_\pi \approx \frac{1}{<D>}\frac{\sqrt{n_+^{\pi^+}+n_+^{\pi^-}+n_-^{\pi^+}+n_-^{\pi^-}}}{n_+^{\pi^+}-n_+^{\pi^-}+n_-^{\pi^+}-n_-^{\pi^-}} \quad . \tag{7.2}
$$

7.1.2 Pion Rejection Factor: $\Delta\eta$

The uncertainty on the pion rejection factor η is:

$$
\begin{aligned}
\frac{\Delta\eta}{\eta} = & \Bigg\{ \left[\left(\frac{\Delta h_m}{h_m}\right)^2+\left(\frac{\Delta h_{m_a}}{h_{m_a}}\right)^2\right]\left(1-\frac{\Phi_m}{\Phi_{m_a}\delta}\right)^2+\left[\left(\frac{\Delta e_m}{e_m}\right)^2+\left(\frac{\Delta e_{m_a}}{e_{m_a}}\right)^2\right]\cdot \\
& \left(1-\frac{\Phi_{m_a}\delta}{\Phi_m}\right)^{-2}+\left[\left(\frac{\Delta c_h}{c_h}\right)^2+\left(\frac{\Delta c_e}{1-c_e}\right)^2\right]\left[\left(1-\frac{\Phi_m}{\Phi_{m_a}\delta}\right)^{-1}-\left(1-\frac{1}{\delta}\right)^{-1}\right]^2\Bigg\}^{\frac{1}{2}} \quad ,
\end{aligned}
\tag{7.3}
$$

with h_m (h_{m_a}) the number of measured hadrons (above the cut) and e_m (e_{m_a}) the number of measured positrons (above the cut). Here c_h is positron contamination of the hadron sample, c_e the hadron contamination of the positron sample, $\Phi_m = h_m/e_m$ the measured total flux ratio, $\Phi_{m_a} = h_{m_a}/e_{m_a}$ the measured flux ratio of the particles above the cut, and $\delta = \frac{(1-c_e)}{c_h}$ the contamination ratio. Δh_m, Δh_{m_a}, Δe_m, Δe_{m_a}, Δc_h and Δc_e are the corresponding (statistical) uncertainties.

7.2 Naming of PID Quantities

The colloquial names of the PID quantities are listed together with their interpretations in tab.7.1. The result of the TRD probability analysis Γ'_{TRD} was wrongly named 'PID5'. This name was reserved for the overall HERMES PID $\Gamma'_{\mathrm{HERMES}}$ that is now named 'PID3+5'. The correct naming would be 'TRDpid' for Γ'_{TRD} and 'PID5' for $\Gamma'_{\mathrm{HERMES}}$.

Table 7.1: The colloquial (but unfortunate) naming of the PID quantities (see text).

in this thesis	coll.name	g1DST/smDST	meaning
$\Gamma'_{Pre} + \Gamma'_{Cal}$	PID2	g1Track_PID2	log.likelihood of preshower and calorimeter
$\Gamma'_{Pre} + \Gamma'_{Cal} + \Gamma'_{Cer}$	PID3	g1Track_PID3	log.likelihood of preshower, calorimeter, and Čerenkov
—	PID4	g1Track_PID4	PID3 + an old prob.analysis of the TRD truncated mean
$\Gamma'_{\mathrm{HERMES}}$	PID3+5	PID3+PID5	log.likelihood of all four HERMES detectors, see sect.4.4.2
Γ_{HERMES}	PID6	g1Track_PID6	includes $\Gamma'_{\mathrm{HERMES}}$ and flux ratios see sect.4.4.2
oldPID	valley cut	see eq.4.19 sect.4.4.2	old PID scheme combining PID3 and TRD truncated mean
$\mathrm{TRD}_{\mathrm{tmean}}$	truncated mean	g1Track_rTRD	TRD truncated mean value see sect.4.1.2
Γ'_{TRD}	PID5	g1Track_PID5	result of the TRD probability analysis, see sect.4.3.1

7.3 Data Quality of the PID Detectors (1996)

The average detector responses for positrons and hadrons are plotted versus time (run number) in figures 7.1 - 7.4. As an example the, the top half of the HERMES spectrometer is shown for polarized data analyzed. No systematic bias on the polarized measurements is expected because the detector responses behave stable over the entire running period.

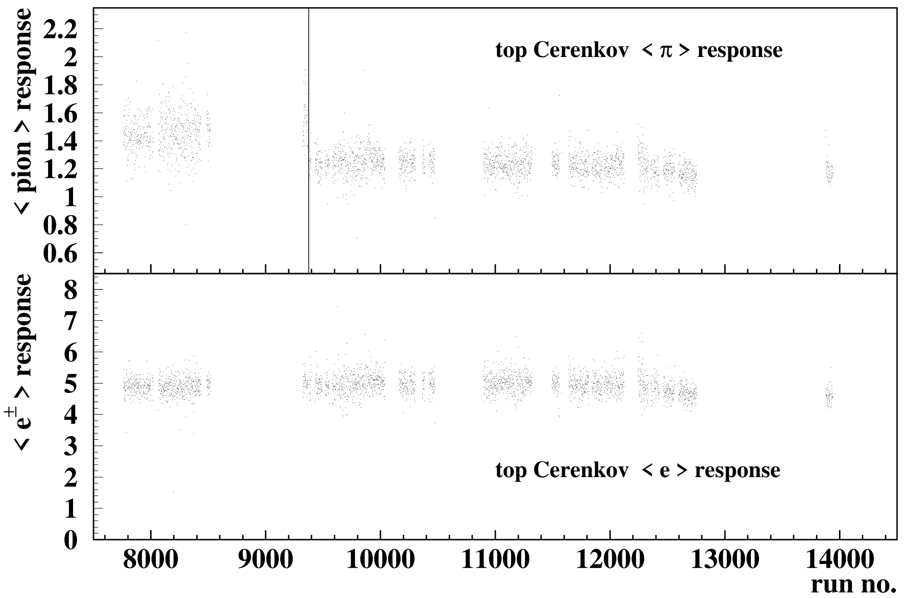

Figure 7.1: The average Čerenkov response for hadrons and $e^{\pm}$ versus run number (1996). The horizontal line marks the point in time the calorimeter threshold was changed from 3.5 to 1.4 GeV.

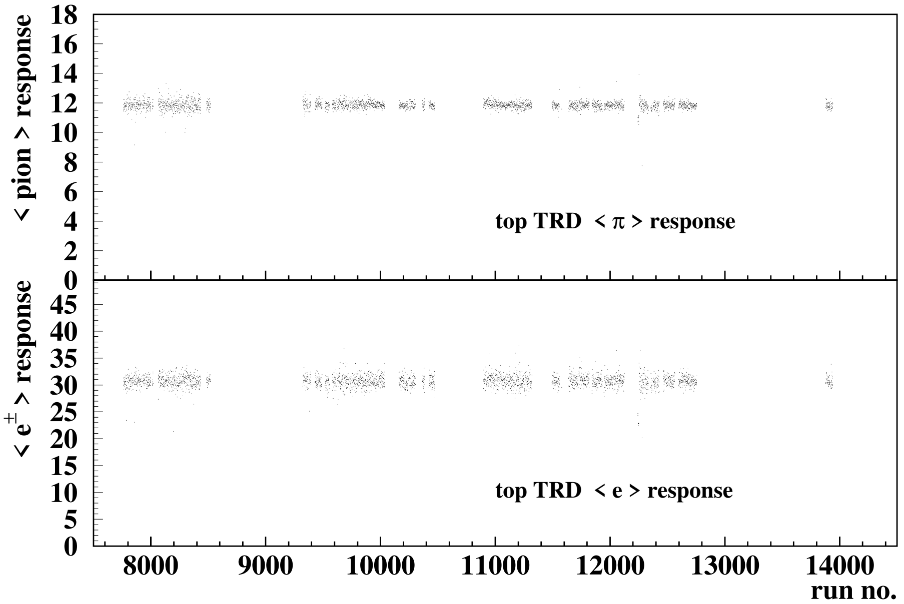

Figure 7.2: The average TRD response for hadrons and $e^{\pm}$ versus run number (1996). The runs around 8000 and 12300 show a high-voltage trip. In these runs, the TRD is not used for particle identification (PID-downshifting).

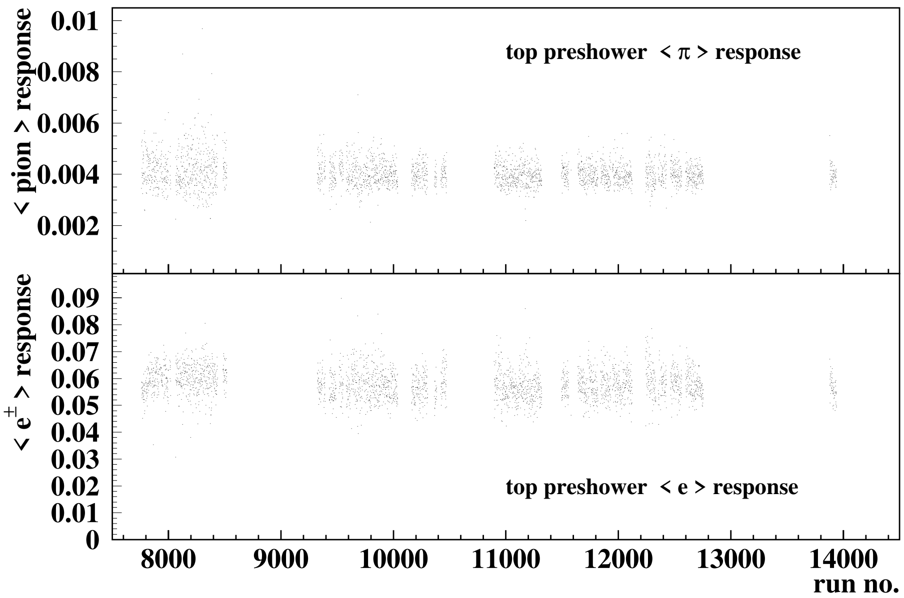

Figure 7.3: The average preshower response for hadrons and $e^{\pm}$ versus run number (1996)

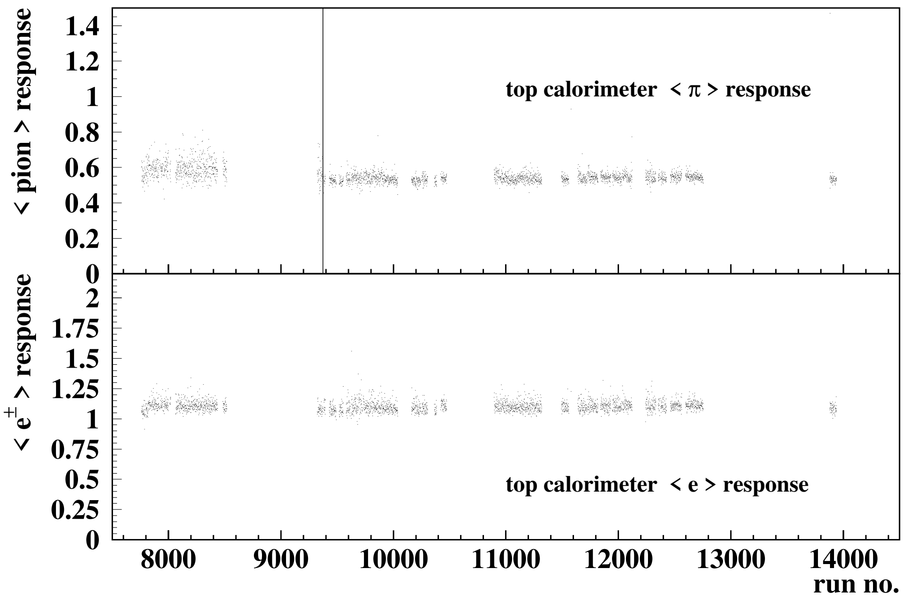

Figure 7.4: The average calorimeter response for hadrons and $e^{\pm}$ versus run number (1996). The horizontal line marks the point in time the calorimeter threshold was changed from 3.5 to 1.4 GeV.

7.4 Tables of the Results

Table 7.2: The measured values of the inclusive asymmetry on the proton (1996).

x_{Bj}-bin	$< x_{Bj} >$	$< D >$	A_{incl}	ΔA_{incl}
1	0.033	0.725	0.105	0.014
2	0.047	0.595	0.105	0.016
3	0.065	0.503	0.100	0.018
4	0.087	0.429	0.187	0.021
5	0.119	0.362	0.231	0.023
6	0.168	0.298	0.263	0.027
7	0.244	0.241	0.405	0.034
8	0.382	0.217	0.471	0.047

Table 7.3: The values of the single charged hadron asymmetries on the proton (1996).

x_{Bj}-bin	$< x_{Bj} >$	$< D >$	$A^s_{h^+}$	$\Delta A^s_{h^+}$	$A^s_{h^-}$	$\Delta A^s_{h^-}$
1	0.033	0.721	0.124	0.035	0.105	0.042
2	0.047	0.590	0.111	0.037	0.092	0.046
3	0.065	0.514	0.096	0.039	0.079	0.049
4	0.087	0.465	0.176	0.045	0.245	0.058
5	0.118	0.441	0.269	0.047	0.255	0.063
6	0.166	0.439	0.343	0.056	0.335	0.079
7	0.239	0.451	0.544	0.073	0.240	0.105
8	0.358	0.464	0.495	0.130	0.487	0.190

Table 7.4: The values of the single charged pion asymmetries on the proton (1996).

x_{Bj}-bin	$< x_{Bj} >$	$< D >$	$A^s_{\pi^+}$	$\Delta A^s_{\pi^+}$	$A^s_{\pi^-}$	$\Delta A^s_{\pi^-}$
1	0.033	0.734	0.124	0.043	0.103	0.049
2	0.047	0.619	0.107	0.049	0.061	0.056
3	0.065	0.558	0.059	0.053	0.077	0.062
4	0.087	0.527	0.211	0.062	0.226	0.075
5	0.117	0.514	0.259	0.067	0.196	0.083
6	0.165	0.516	0.376	0.083	0.207	0.107
7	0.238	0.519	0.478	0.114	0.276	0.150
8	0.354	0.515	0.690	0.221	0.449	0.281

Table 7.5: The values of the pion charge difference asymmetry on ^{3}He (1995).

x_{Bj}-bin	$< x_{Bj} >$	$< D >$	$< Q^2 >$	$A_\pi^{^3\mathrm{He}}$	$\Delta A_\pi^{^3\mathrm{He}}$
1	0.033	0.747	1.24	1.07	0.38
2	0.047	0.624	1.54	-0.29	0.35
3	0.064	0.574	1.93	0.09	0.33
4	0.086	0.553	2.47	-0.47	0.33
5	0.117	0.548	3.26	0.24	0.31
6	0.165	0.545	4.40	-0.31	0.34
7	0.237	0.546	6.10	-0.08	0.43
8	0.361	0.534	8.80	1.00	0.77

Table 7.6: The values of the pion charge difference asymmetry on the proton (1996).

x_{Bj}-bin	$< x_{Bj} >$	$< D >$	$< Q^2 >$	A_π^p	ΔA_π^p
1	0.033	0.734	1.23	0.19	0.25
2	0.047	0.619	1.52	0.25	0.28
3	0.065	0.558	1.88	0.01	0.26
4	0.087	0.527	2.38	0.18	0.24
5	0.117	0.514	3.10	0.37	0.24
6	0.165	0.516	4.22	0.61	0.25
7	0.238	0.519	5.87	0.75	0.34
8	0.354	0.515	8.45	1.07	0.76

Table 7.7: The extracted values of the valence quark spin distributions using the pion charge difference asymmetries on ^{3}He (1995) and the proton (1996).

x_{Bj}-bin	x_{Bj}	$x_{Bj} \cdot \delta u_v$	$x_{Bj} \cdot \Delta\delta u_v$	$x_{Bj} \cdot \delta d_v$	$x_{Bj} \cdot \Delta\delta d_v$
1	0.033	0.25	0.10	0.80	0.28
2	0.047	0.01	0.11	-0.24	0.30
3	0.065	0.03	0.13	0.10	0.33
4	0.087	-0.06	0.14	-0.53	0.39
5	0.118	0.26	0.16	0.36	0.42
6	0.165	0.23	0.19	-0.38	0.51
7	0.238	0.43	0.27	0.00	0.66
8	0.358	0.93	0.50	1.48	1.04

8 Bibliography

References

[1] F.E.Close, *An Introduction to Quarks and Partons*, Academic Press, 1979

[2] F.Halzen and A.D.Martin, *Quarks & Leptons*, J.Wiley & Sons, 1984

[3] P.Schmüser, *Feynman-Graphen und Eichtheorien für Experimentalphysiker*, Springer-Verlag, 1995

[4] M.Vetterli, lecture notes, *Deep Inelastic Lepton Scattering*, HERMES Internal Note 93-016, 1993

[5] A.V.Manohar, *An Introduction to Spin Dependent Deep Inelastic Scattering*, Proc.of the 7th Lake Louise Winter Institute, 1992, editors: B.A.Cambell *et al.*, World Scientific Singapore, 1992

[6] L.W.Whitlow *et al.*, Phys.Lett. **B 250** No.1,2 193-198, 1990 Note: this reference has a typographic mistake. Correct is $b_1 = 0.0635$.

[7] E143 Collaboration (K. Abe *et al.*), Phys.Rev.Lett.**76**:587-591, 1996

[8] H.L. Lai, J. Huston, S. Kuhlmann, F. Olness, J. Owens, D. Soper, W.K. Tung, H. Weerts,*CTEQ Parton Distribution Functions*, Phys. Rev. **D55**, 1280 (1997). The parametrization *CTEQ4D standard DIS scheme* is used throughout the analysis in this thesis.

[9] F.E.Close, *The Nucleon Spin Crisis Bible*, Rutherford Appleton Laboratory, RAL-93-034, 1993

[10] E.L.Berger, *Semi-Inclusive Inelastic Electron Scattering from Nuclei*, published in Proc.of of the Workshop on Electronuclear Physics with Internal Targets, Stanford, CA, Jan.87, ANL-HEP-PR-87-45, 1987

[11] T.Pussieux, R.Windmolders, *A Collection of Formulas for Spin Dependent Deep Inelastic Scattering*, DAPNIA/SPhN 95 10, 03/1995

[12] A.A.Sokolov, I.M.Ternov, Sov.Phys.Dokl.8, (1964) 1203

[13] D.P.Barber *et al.*, *The HERA polarimeter and the first observation of electron spin polarization at HERA*, Nucl.Inst.Meth. A329 (1993) 79-111

[14] The HERMES Collaboration, *Technical Design Report*, DESY-PRC 93-06, MPIH-V20 1993

[15] D.De Schepper, *Spin-dependent deep inelastic positron scattering from a polarized helium-3 internal gas target*, Ph.D.thesis, MIT, June 1997, HERMES internal note 97-022

[16] S. Pate *et al.*, *Cryogenic Polarized* ^{3}He *Gas Target for HERMES*, Proc.of the Int.Workshop on Polarized Beams and Polarized Gas Targets, Cologne, Germany, Jun.1995, editors: H.Paetz gen. Schieck and L. Sydow, World Scientific Singapore, 1996, HERMES internal note 95-017

[17] W.Lorenzon *et al.*, Phys.Rev. **A47**, 468 (1993)

[18] B.Braun, *Polarization of the HERMES Hydrogen Target* HERMES internal note, to be published in the Proc.of Spin96, Amsterdam, September 1996

[19] K. Zapfe *et al.*, *A High Density Polarized Hydrogen Gas Target for Storage Rings*, Rev.Sci.Instrum. 66 (1) (1995) 28-31, 1995, HERMES internal note 95-067

[20] The HERMES Collaboration, *The HERMES internal Target*, HERMES internal note 97-11, (1997), to be published

[21] M.Düren, *The HERMES Experiment: From the Design to the First Results*, Habilitationsarbeit, Universität Erlangen, 1995, HERMES internal note 95-02

[22] The HERMES Collaboration, *The HERMES Spectrometer*, DESY internal note HERMES 97-10, (1997), to be published

[23] W.Wander, *Rekonstruktion hochenergetischer Streuereignisse im HERMES Experiment*, Doktorarbeit, Universität Erlangen, April 1996, HERMES internal note 96-023, English version: 97-031

[24] E.Devitsin *et al.*, *Luminosity Monitor Calibration in 96*, HERMES internal note 97-015

[25] J.D.Jackson, *Classical Electrodynamics*, J. Wiley & Sons, 1975

[26] C.Grupen, *Teilchendetektoren*, BI-Wiss.-Verl., 1993

[27] X.Artru, G.B.Yodh, and G.Mennessier, Phys.Rev. **D12**, 1289 (1975)

[28] J.Cobb *et al.*, *Transition Radiators for Electron Identification at the Cern ISR*, Nucl.Inst.Meth. 140 (1977) 413-427

[29] R.Kaiser for the HERMES PID Group, *Particle Identification at HERMES*, HERMES internal note 97-025

[30] G.D'Agostini, *A Multidimensional Unfolding Method Based on Bayes' Theorem*, DESY 94-099, June 1994

[31] J.E.Emerson, *Modeling of the HERMES Transition Radiation Detector*, M.Sc.Thesis, Simon Fraser University, August 1995

[32] The C-translation of the code was done by P.Green

[33] The HERMES g_1^p Groups (EURO and NAPA), *Status of the g1n(x) Analysis of the 1995 He3 Data*, HERMES internal note 96-042, Sept. 1996

[34] R.B.Kaiser, *Measurement of the Spin Structure of the Neutron using Polarised Deep Inelastic Scattering* Ph.D.thesis, Simon Fraser University, April 1997, HERMES internal note 97-017

[35] The 1996 bad-bit list was taken from the g_1^p-group. B.Tipton, private communication

[36] E.M.Kabuß for the SMC Collaboration, *Asymmetries from Semi-Inclusive Polarized Deep Inelastic Scattering*, Proc.of DIS97, Chicago, April 1997, to be published by the American Institute of Physics, *DEEP INELASTIC SCATTERING AND QCD: 5th International Workshop*, editors: J.Repond, D.Krakauer, October 1997

[37] C.Ciofi degli Atti *et al.*, Phys.Rev. **C48** (1993) R968

[38] The leading-order parametrization *110 Gluon A (LO)* comes from: Gehrmann *et al.*, hep-ph/9512406

[39] P.Renton and W.S.C.Williams, Annual Review of Nuclear and Particle Science **31** (1981) 193.

[40] B.Braun, J.Stewart, and T.Wise, private communication

[41] B.Tipton for the HERMES Polarimeter Group, *Analysis of Positron Beam Polarization Measurements in 1996*, HERMES internal note 97-019, May 1997

9 Acknowledgments

I would like to thank Mike Vetterli for giving me the best possible feedback and freedom a supervisor can give to his student, for support and motivation during the entire work of my thesis, and for the possibility to come to Canada in the first place. I had the greatest time in B.C.. I would also like to thank Prof.A.Wagner who always had ten minutes for me and who made it possible to write my Diplomarbeit at Universität Hamburg and work at TRIUMF at the same time. Mein Dank geht ebenfalls an die Studienstifung des Deutschen Volkes, die mich mit Ihrem Stipendienprogramm während meines gesamten Studiums und des Auslandaufenthaltes unterstüzt hat. I would also like to thank my parents who gave me 'roots and wings' and unlimited support at any time.

I would also like to thank the people I have worked with: Eric Belz who was always up for a Sushi feast, made sure that life in office no.5 never got boring, and spoiled my English so decently that I am quite proud of it. Ralf Kaiser who was an incredible source of information during the first half of my Diplomarbeit and the person who is liable for the fact that I went to Canada. Jinsong Ouyang who showed me how to survive the TRIUMF cafeteria with a chickenburger-diet; he also never hesitated to help me with something: physics, software, or a ride to anywhere. Manuella Vincter who got me started in Hamburg in my first weeks of my Diplomarbeit. Andy Miller who always asked these 'right questions' at the weekly meetings. And Tim Shoppa who helped anytime concerning computer matters either by atomic fireballs, himself, or just by his presence providing a strong enough Tim-field. My thanks go again to the entire HERMES-TRIUMF group for the comfortable working atmosphere, group BBQs/lunches, and more.

I would also like to mention the two cubeville residents Jens Dilling and Trevor Stocki for coffee and nice chats on long working days. It is also time to mention my 'glorious' TRIUMF Volleyball team. It was fun to get injured together. My roommates Mike and Rob with their generosity, humor, and friendship made my stay in Vancouver unforgettable; it was hard to go and leave 4274 W 11th Ave behind. Maybe I am back someday. I would also like to thank the Kits Volleyball team for having a lot of decent games and beers (Bimini). Also Marco and Sonia were always there for beer, tea, and some 'culture' during endlessly rainy days and nights (By the way: life is NOT exponential!).

I would also like to thank all Hermesians I have worked with: Arthur Mateos for his feedback, Kevin McIlhany for all the (PID) discussions, Brendan Fox who was very patient with me (or I with him?), Holger Ihssen, Michael Ruh, and Antje Brüll as valuable sources of the EURO side, Mark Sutter, Bryan Tipton, and Jeff Martin for working at night, helping me drinking three kegs of beer, and supporting some stupid ideas from time to time.

Weiterer Dank gilt allen, die die Heimatbasis gehalten haben: Meine Geschwister: Linus, Nina und Sophie; außerdem Götz, Ansgar, Uschi, Christine, Hannes, Britta, Mati und alle in Sachen 'Operation DOKO'. Ferner auch mein Dank an alle (ex-)Natural Science Singers und DESY-Kommilitonen, die mir aus der Ferne mit den 'kleinen' Dingen ausgeholfen haben.